UNIVERSITÀ DEGLI STUDI DI PADOVA

DIPARTIMENTO DI SCIENZE CHIMICHE

CORSO DI LAUREA MAGISTRALE IN CHIMICA

TESI DI LAUREA MAGISTRALE

Synthesis in Confined Space of Undoped and Eu(III)-doped Yttrium Vanadate Phosphors

Relatore: Prof. Silvia Gross

Correlatore: Prof. Dr. Klaus Müller-Buschbaum

Controrelatore: Prof. Valerio Di Marco

Laureando: Andrea Guerrer

ANNO ACCADEMICO 2023/2024

Table of contents

1 INTRODUCTION AND AIM OF THE THESIS

The concept of confined space is very attractive in the field of inorganic synthesis, as it represents a promising approach to develop synthetic methods that allow a precise control over the reaction outcome, ensuring to obtain inorganic materials with well-defined functional properties. The confined space is defined as an enclosed nanoscale volume with limited accessibility,[1] which ensures a thoroughly controlled reaction environment that may involve some different reaction pathways as compared to the same reaction carried out in a typical non-confined space. This because the confined space on one hand entails phenomena such as the alteration of the physical-chemical properties of the matter, e.g. the density, dielectric constant, or conductivity of the solvent, that can allow non-conventional crystallisation pathways. On the other hand, the fact that both reactants and products remain in a specific volume range with a specific shape results in a better control over the size distribution and shape of the resulting product by confining its formation.[2]

Among the nanoscale hosts in which a reaction can occur, miniemulsions can be referred to as "nanoreactors" since the reaction is carried out within the small droplets of the emulsion system (see Chapter 2). Miniemulsions are a particular class of emulsions obtained by high shear treatment, usually exploiting high power ultrasounds, of a mixture of two immiscible liquids, a surfactant and an osmotic agent, leading to the formation of small droplets (30 nm to 500 nm) of the dispersed phase in the continuous phase, either water-in-oil or oil-in-water.[3] The surfactant and the osmotic agent guarantee the droplets' stability against the degradation processes of coalescence and Ostwald's ripening respectively,[4] allowing the droplets to be considered as separate and individual nanoreactors, since there is no inter-droplet exchange of matter until an external force (e.g. ultrasounds) favour the fusion of the droplets. This latter feature is what differentiate miniemulsions from microemulsions, where the droplets exchange matter spontaneously upon simple mixing.

Another attractive nanoscale host is represented by mesoporous materials, which are defined as materials possessing pores with sizes ranging from 2 nm to 50 nm.[5] The pore size distribution and pore structure can easily be tuned by means of the synthetic procedure, allowing an easy optimisation of the material for specific synthetic purposes. Usually, mesoporous materials are exploited as supports for noble metals nanoparticles as catalysts.[6] However, they can be used as a model of solid confined space, by restricting the reaction inside the pores. Exploiting this kind of materials as solid confined space can have several advantages, such as the better control over the morphology and size distribution of the product due to the defined pores' shape and size. Moreover, the restricted environment can inhibit phenomena such as sintering or coalescence of the particles and can also favour the interaction among

the reagents thanks to their proximity, leading to a faster reaction or lower reaction temperature compared to a classical solid-state synthesis.

The objective of this thesis is to assess and evaluate the effects of the space confinement, given either by the miniemulsion's droplets or by the pores of a mesoporous material, on the nucleation and crystallisation of a target inorganic crystalline matrix, i.e. non-substituted and Eu(III)-substituted yttrium vanadate. To do that, the properties of the material (i.e. structure, morphology, and photoluminescence) obtained within the confined space framework are compared to the properties of the same material synthesised through classical, non-confined processes. The batch syntheses are considered as opposed to miniemulsion syntheses, as regards the wet chemistry synthesis, while the syntheses within mesoporous materials are exploited as syntheses in confined space regarding the solid-state approach. The possible noted differences are likely related to the spatial confinement of the reactions.

Yttrium vanadate, both non-substituted and Eu(III)-substituted, is chosen as model inorganic matrix as it possesses good luminescent properties and a very efficient energy transfer to the lanthanide ions, properties that make it a worldwide used matrix to obtain red phosphors.[7] Moreover, studies have proved that the crystallisation of this matrix proceeds through an amorphous intermediate (Ostwald's step rule)[8], making it possible to follow the crystallisation process via photoluminescence measurements, which may allow to deepen the knowledge of its crystallisation pathway.[9] Further information on this inorganic matrix is found in **Chapter 3**. Within the work of this thesis, non-substituted and Eu(III)-substituted yttrium vanadate were synthesised both via inverse miniemulsion approach and through the synthesis in mesoporous materials. Since the photoluminescence properties depend on the structure and morphology of the product, the size, size distribution, shape, crystallites size and crystalline phase of the obtained nanoparticles were analysed and related to the photoluminescence properties measured for each product, and the possible differences compared to classical synthesis highlighted.

This master thesis is organised into seven chapters. More in detail, the current **Chapter 1** represents the introduction of the thesis project, with a brief overview regarding the space confinement. **Chapter 2** outlines the concept of synthesis in confined space and focuses on the exploited nano spaced systems, i.e. miniemulsions and mesoporous metal oxides, highlighting first their basic concepts and general definitions, and then presenting the main approaches for their preparation and the main synthetic processes that involve these systems as model confined space. In **Chapter 3**, the studied inorganic matrix – yttrium vanadate – is introduced, presenting its structural, physical-chemical and photoluminescence properties and the state of the art of its synthetic procedures. In **Chapter 4**, the results of the experimental work are presented and discussed, and the outcomes are related to the effect of the confined space on the synthesis of this specific inorganic matrix. In **Chapter 5**, the characterisation techniques employed within the work of this thesis are described, with particular emphasis on the less

common techniques. In Chapter 6, the experimental details for the synthesis and optimisation of the different systems are presented. Finally, in Chapter 7 the conclusions that can be drawn from this experimental work are presented, along with the perspectives for future studies on this system.

2 SYNTHESIS IN CONFINED SPACE

Inorganic nanoparticles have drawn much interest among scientists thanks to their applications in several fields, ranging from biomedicine[10] to catalysis[11] or energy storage.[12] Many synthetic approaches for the production of inorganic nanoparticles have been developed, and they include reactions from the gaseous phase, e.g. chemical vapour deposition (CVD),[13] wet-chemistry reactions, e.g. sol-gel synthesis[14] or co-precipitation method,[15] and finally solid-state reactions, e.g. mechanochemistry[16] or ceramic method.[17] Among all the possible synthetic routes, the synthesis of inorganic nanoparticles in a confined space is gaining increasing relevance thanks to peculiar properties that a confined environment can imply. Indeed, downsizing the available volume for the reaction to occur can alter the physical-chemical properties of the species, such as the density, viscosity and dielectric constant of the solvent,[18] as well as allowing non-conventional crystallisation pathways even at low temperatures. Moreover, the restricted space in which the reaction is happening may lead to a more favourable interaction among the reactants, and the shape and size of the environment affect the final morphology of the product, leading to more homogeneous nanoparticles.[2]

Amongst the possible confined space systems, the two exploited within the work of this thesis were miniemulsions and mesoporous materials. In the following paragraphs, an introduction on those two systems is given.

2.1 Miniemulsions

In the following section, the theoretical aspects at the basis of emulsions and miniemulsions in particular are presented. Historically, miniemulsions have been used primarily for the synthesis of polymeric colloids,[19,20] but in these last years they have also proved to be efficient for the confined space synthesis of inorganic materials, such as ZnS, $CaMoO_4$, and ZnO.[21–26]

2.1.1 General definitions and basic principles

Emulsions are defined by IUPAC as a dispersion of liquid droplets (dispersed phase) in another non-miscible liquid (continuous phase).[5] A first classification of different types of emulsions can be made based on the nature of the continuous and dispersed phases: when an apolar phase is dispersed in a polar continuous phase, these kinds of emulsions are referred to as *direct emulsions*, and are usually called “oil-in-water” emulsions (o/w). *Inverse emulsions* are represented by the opposite scenario, i.e. a polar phase dispersed in an apolar continuous phase, and are referred to as “water-in-oil” emulsions (w/o). A further classification can be made based on the droplets size: *macroemulsions*, which present droplets with a diameter larger than 1 µm, *miniemulsions*, which possess droplets with a diameter between 500 nm and 30 nm, and *microemulsions*, with droplets of diameter less than 100 nm.[27] In order to provide a more complete definition of the different types of emulsion, the thermodynamics of the formation of these systems has to be addressed. The process of formation of an emulsion is associated with a variation of the Gibbs’ free energy (Equation 2.1):

$$\Delta G_{form} = \gamma_{12}\Delta A - T\Delta S_{conf} \qquad \textbf{2.1}$$

where the first term represents the energy required for the formation of a new interface, more in detail γ_{12} is the interfacial tension between the two phases 1 and 2, and ΔA is the newly formed interfacial area due to the emulsification process. The second term represents the gain in energy during the formation of the emulsion, more in detail T is the temperature and ΔS_{conf} is the change in configurational entropy, which is positive thanks to the formation of a large number of droplets. For macro- and miniemulsions, the ΔG_{form} for the emulsification process results positive, due to the fact that the droplets' surface is not completely covered by the surfactant (Figure 2.1.1), thus resulting in a high value of the first term of the Equation2.1 and therefore an external force has to be applied for these systems to form; however, for miniemulsions, the second term is closer in value to the first one, since a higher amount of smaller droplets is formed, which results is a higher ΔS_{conf}. A further difference between macro- and miniemulsions is the fact that the former can be obtained by simple mechanical stirring, while the latter can be obtained only through a high-shear treatment (see Chapter 2.1.2). On the other hand, for microemulsions, the variation in Gibb's free energy associated with the formation of the emulsion is negative ($\Delta G_{form} < 0$), due to the low interfacial tension of the system and the high change in configurational entropy due to the formation of a large number of small droplets; therefore, microemulsions are thermodynamically stable and do not require external work to form, apart for an initial mechanical stirring to favour the mixing of the two phases. The low interfacial tension in microemulsions is obtained through the addition of a high amount of surfactant (complete coverage of the droplets' surface, Figure 2.1.1), which can lower the interfacial tension value up to the point where the emulsification process results thermodynamically favoured.

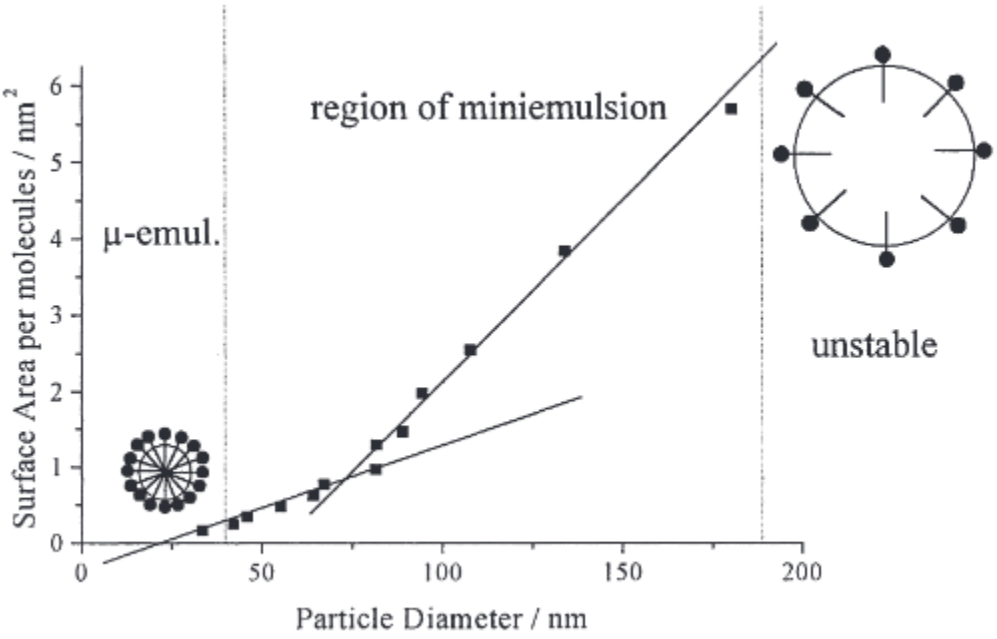

Figure 2.1.1: Different surfactant amounts for different types of emulsion.[28]

2.1.2 Preparation and stability of miniemulsions

To prepare an emulsion, an aqueous phase, an organic phase, a surfactant, and an osmotic agent are needed: the relative amounts of these factors rule the average size of the emulsion droplets, therefore determining the type of emulsion that will be obtained (Figure 2.1.2).

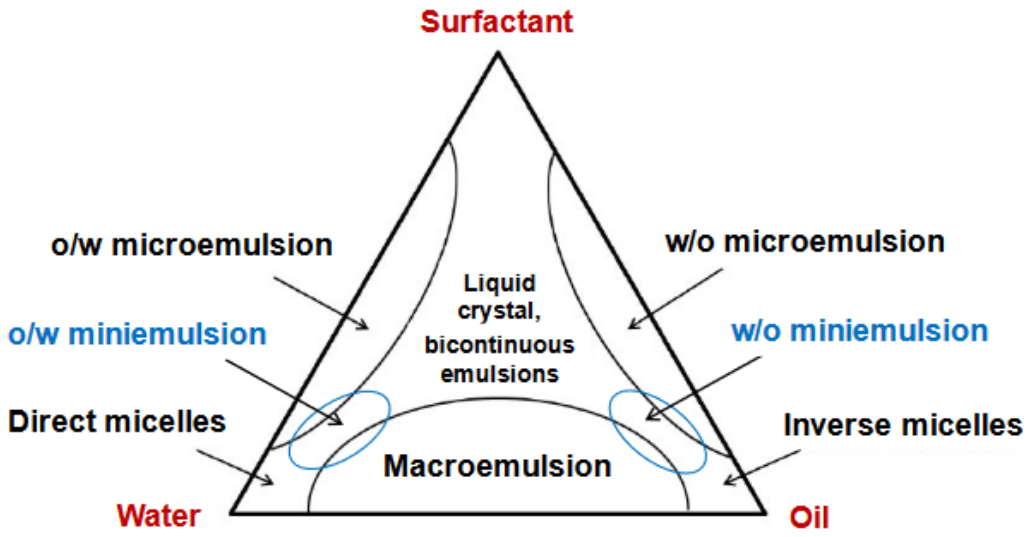

Figure 2.1.2: Ternary phase diagram for the water/oil/surfactant system.[29]

Miniemulsions are represented by stable emulsions with very small droplet sizes.[30] However, as stated in paragraph 2.1.1, miniemulsions are not thermodynamically stable because of the positive ΔG_{form} associated with the emulsification process: the miniemulsions are rather defined as kinetically stabilised,[31] since they reach a steady state in the process of their formation. To better explain this concept, the mechanism of the formation of a miniemulsion must be introduced. Since the emulsification process for this type of emulsion is not spontaneous, an external energy, higher in magnitude than the positive $\gamma_{12}\Delta A$ term, has to be applied to the mixture: the mechanical stirring is not energetic enough to overcome this factor, therefore a high-shear treatment is required. Usually, the external energy is provided by high energy ultrasounds for small quantity of liquid, and by high pressure devices for larger amounts.[32] As regards the application of ultrasounds, there are several possible mechanisms proposed for the formation and disruption of droplets, but the most crucial is the cavitation process.[30] Sound waves propagate through matter via a series of compression and rarefaction waves. When the power is high enough, the rarefaction waves may exceed the attractive forces of the molecules of the medium, causing the bubbles to form. The succeeding compression wave will make these bubbles collapse, generating the energy required in form of shock waves for the physical or chemical process to occur.[33] For the formation of miniemulsions, at first the two different phases, aqueous and organic, are stirred together to obtain macro-droplets: the simple mechanical agitation does not provide sufficient energy to overcome the first term of Equation 2.1, and therefore the miniemulsion does not form. Subsequently, high-energy ultrasounds are applied to obtain the miniemulsions (Figure 2.1.3). During the sonication, the droplets' size changes rapidly and the polydispersity of the system decreases (Figure 2.1.3) until it reaches a steady

state, where the droplets' size is a function of the relative amounts of oil, water, surfactant, and osmotic agent, and not anymore of the mechanical energy supplied (Figure 2.1.4). To follow the evolution of the system, turbidity or surface tension measurements are required.[30] However, surface tension measurements depend on the total interfacial area, which increases during the sonication time, but it cannot distinguish between monodisperse and polydisperse systems, whereas turbidity measurements are also sensitive to the size distribution of the system.

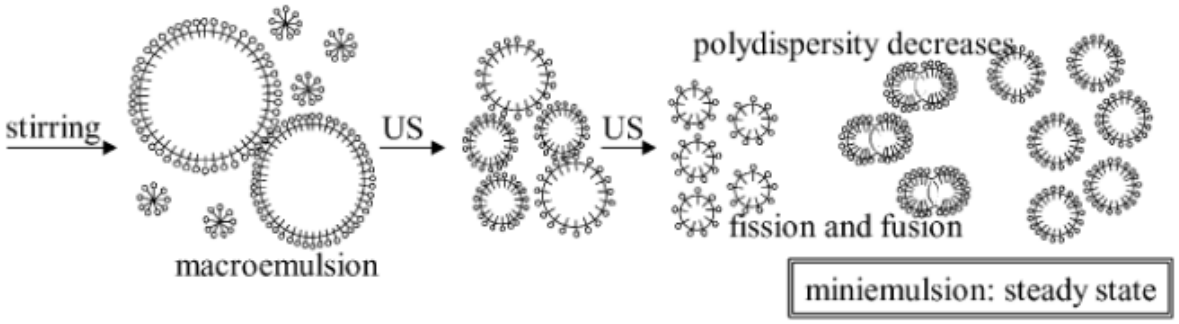

Figure 2.1.3: Schematical representation of the formation of a miniemulsion.[30]

The emulsification process involves two different mechanisms: first, the disruption of droplets, which causes an increase in the interfacial area, and second, the adsorption of surfactant molecules at the interface. This because the adsorption of surfactant molecules occurs in a time scale much longer than the disruption process, and this is why special mechanical designs have been developed to guarantee either a high turbulent flow after disruption or sufficient residual time in elongation flow to allow surfactant molecules to adsorb at the interface.[34] Experimental studies have demonstrated that, during sonication, droplets undergo a dynamic equilibrium of the Fokker-Plank type:[34] droplets after fission are much smaller but colloidally unstable, whereas the bigger droplets have a higher probability of undergoing the fission phenomenon. This means that the resulting miniemulsion possesses the smallest possible droplet size for the given system and that these droplets are at the borderline between stability and instability: the miniemulsion is said to be critically stabilised.[30]

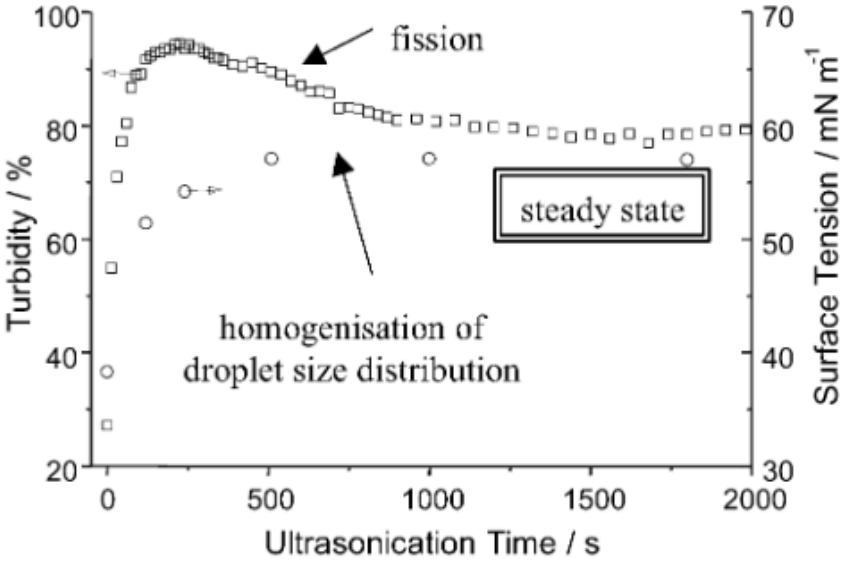

Figure 2.1.4: homogenization process followed by turbidity and surface tension measurements.[30]

As stated above, miniemulsions are not thermodynamically stable, and the system can evolve following two different mechanisms of destabilisation: molecular diffusion, also known as Ostwald's ripening (Figure 2.1.5B), which is a monomolecular process (τ_1) or coalescence by collision (a bimolecular process, τ_2, Figure 2.1.5C).[28]

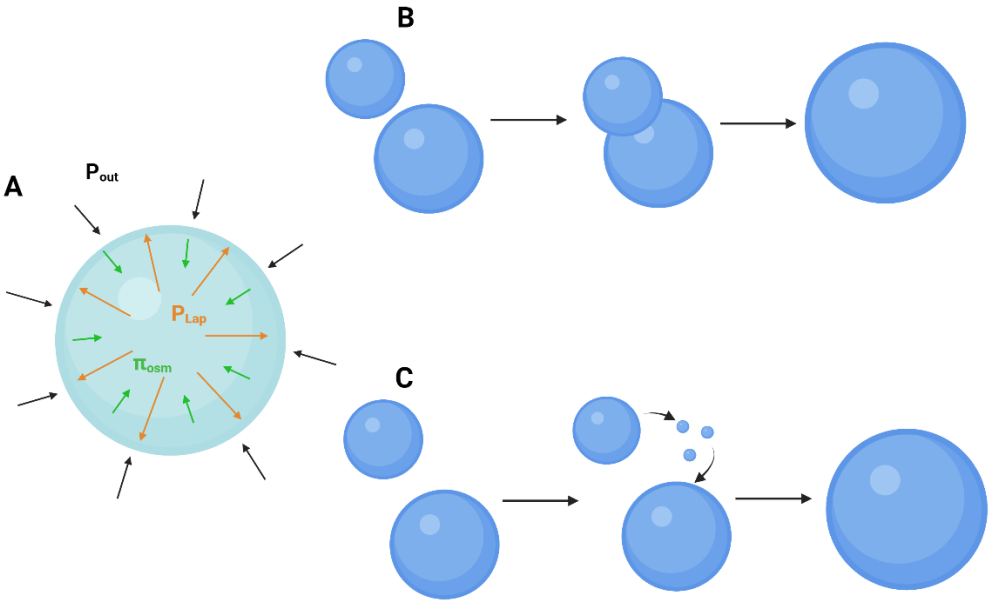

Figure 2.1.5: Pressures acting on a droplet (A), coalescence mechanism (B), Ostwald's ripening (C).

In order to stabilise the system with respect to these two degradation mechanisms, an osmotic agent and a surfactant are added, respectively. The Ostwald's ripening phenomenon arises from the different dimensions of droplets, thus a different vapour pressure and a different chemical potential, which involves a different Laplace pressure (Equation 2.2) for droplets of different sizes, resulting in a net flux

by molecular diffusion through the continuous phase from the smaller droplets, possessing a higher Laplace pressure, to the larger ones in order to reduce the total chemical potential of the system. This flux continues until the Laplace pressure is equalised in all the droplets, which means until the smaller droplets disappear. To avoid this phenomenon, an osmotic agent, that is a species highly insoluble in the continuous phase, is added to the system: this species will cause an inward osmotic pressure to rise, opposed to the outward Laplace pressure of the droplets, according to the **Equation 2.3**:

$$\Delta p_{Laplace} = \frac{2\gamma_{12}}{r} \qquad \textbf{2.2}$$

$$\pi_{osm} = \frac{3nRT}{4\pi r^3} \qquad \textbf{2.3}$$

where γ_{12} is the interfacial tension, r is the droplet's radius, n is the amount of osmotic agent in moles, T is the absolute temperature and R is the universal constant for gases. Besides, for direct miniemulsions, there is evidence that after the ultrasonication step, the droplets' dimensions do not differ by varying quantities of osmotic agent, that is, the droplets' size does not depend on the concentration of the osmotic agent. This is a hint at the fact that there is no pressure balance between the osmotic and Laplace pressures for each droplet, but rather there is an equal pressure in all the droplets as they are osmotically stabilised (**Figure 2.1.5A**). The pressure balance can be reached only through collisions of the droplets, which occurs in a time scale of hundreds of hours.[28] For direct miniemulsions, the osmotic agent is represented by an ultrahydrophobe.

However, even if an emulsion is stabilised against the Ostwald's ripening, it still can undergo the coalescence by collision process. In order to inhibit this phenomenon, a surfactant is added to the system, which provides either electrostatic or steric stabilisation of the droplets.[34] The IUPAC definition of surfactant states that "a surface active agent (= surfactant) is a substance which lowers the surface tension of the medium in which it is dissolved, and/or the interfacial tension with other phases, and, accordingly, it is positively adsorbed at the liquid/vapour and/or at other interfaces".[5] There are several types of surfactants, and the use of one surfactant or another depends on the considered system, since they can drive the formation of direct or inverse emulsions depending on their nature. Thus, the most important classification for surfactants is based on the hydrophilic-lipophilic balance (HLB, **Equation 2.4**),[35] which is an empirical parameter based on the hydrophilic or lipophilic groups present in the molecule.

$$HLB = [(n_H \cdot H) - (n_L \cdot L)] + 7 \qquad \textbf{2.4}$$

Where H and L are constants attributed to the hydrophilic and lipophilic groups respectively, and n_H and n_L are the number of hydrophilic and lipophilic groups respectively. A large HLB value (HLB > 10) means that the surfactant is soluble in polar solvents, and therefore it will lead to direct emulsions. On the other hand, low HLB values (HLB < 10) means that the surfactant is soluble in apolar solvents and will lead to inverse emulsions. Another important classification is made upon the charge of the surfactant: they can be either ionic or non-ionic. Usually, ionic surfactant are exploited to obtain direct miniemulsions.[27,35] Surfactant, contrary to osmotic agents, have an effect on the droplets' size, as shown in **Figure 2.1.2**. As

regards miniemulsions, surfactants are present in such a concentration that the surface of the droplets is not completely covered, and well below the critical micelle concentration (cmc), assuring the absence of free micelles. It can be said that in miniemulsions the surfactant is exploited in the most efficient way possible.[30,34,35]

2.1.3 Inverse miniemulsion

As stated in paragraph 2.1.1, direct miniemulsions are primarily exploited for the synthesis of polymeric colloids. For this type of emulsion, the properties described in the last paragraphs apply. On the other hand, inverse miniemulsions, i.e. water-in-oil emulsions, have been exploited for the synthesis of inorganic compounds being the aqueous environment in the droplets suitable for inorganic reactions. Some differences between o/w and w/o miniemulsions rely on the type of osmotic agent exploited, which is water soluble and lipophobe. Usually, a salt, sugar or ionic compound can be used as osmotic agent, and normally the precursors of the inorganic species themselves can act as osmotic agents, thus eliminating the need to add a further chemical species to the reaction mixture.[34] Then, surfactants with low HLB values, thus soluble in the apolar phase, are required. Several surfactants have been tested, ionic and non-ionic, but the most effective are the block copolymers, especially the poly(ethylene-*co*-butylene)-*b*-poly(ethyleneoxide) [P(E/B)-*b*-PEO].[36] In inverse miniemulsion, the most important stabilisation mechanism is provided by steric stabilisation,[34] and that could explain the higher stability offered by copolymers, and especially [P(E/B)-*b*-PEO]. Another widely used surfactant, which offers less steric stability, is sorbitan monooleate (Span80, Figure 2.1.6). Span80 possesses a HLB value of 4.3, and this is the surfactant exploited within the context of this thesis.

A few examples on the high droplets' stability of inverse miniemulsions can be found considering reactions for which a colour change occurs, such as the formation of Prussian blue[3] or nickel murexide.[20] In both cases, the miniemulsions of the reagents do not react with each other when the simple mixing is occurring, and ultrasounds need to be applied in order to favour the mixing of the droplets, as the colour of the mixture change only upon sonication. Another difference as compared to direct miniemulsions relies on the effect of the osmotic agent on the droplets' size: in inverse miniemulsions, the higher the content of osmotic agent (generally the precursor's salt), the smaller the resulting droplets of the miniemulsion. A further difference is found regarding the pressure balance, when, shortly after sonication, the droplets of an inverse miniemulsion experience a real zero-effective pressure, meaning that the osmotic pressure and the Laplace pressure counterbalance each other. This could be due to the different stabilisation mechanism of inverse miniemulsions, i.e. more relied on the steric stabilisation, and this is what makes them fully stable systems and not only critically stabilised.[20,30,34]

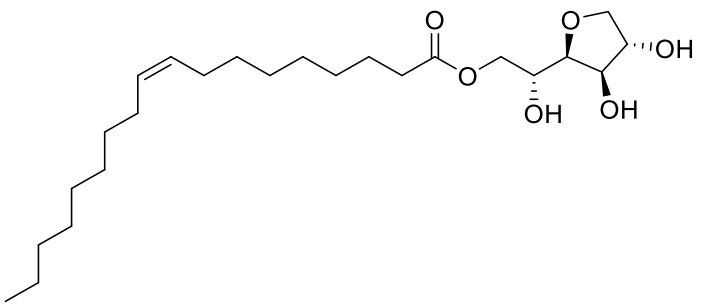

Figure 2.1.6: Structure of Span80.

2.1.4 Miniemulsions as confined space nanoreactors in inorganic chemistry

Many different synthetic routes for inorganic materials have been developed during the last decades, from sol-gel processes to co-precipitation method, but these routes are based on kinetic control of the reactions, that can lead to disadvantages regarding the low homogeneity of the products or the few polymorphs accessible. Therefore, exploiting nanoreactors to reach a thermodynamic control of the reaction outcome is of great interest, since it could pave the way for the synthesis of highly controlled nanoparticles.[37] Within this framework, droplets of a miniemulsions, thanks to their high stability against both coalescence and Ostwald's ripening, are considered as separated and independent nanoreactors in which the reaction is carried out in a high parallel fashion, i.e. the reaction occurs in 10^{18}-10^{20} independent nanoreactors separated by the continuous phase. The formulation of the miniemulsion dictates the reaction conditions in which the product will be formed, allowing to explore non-conventional crystallisation paths by altering the nucleation and growth of the nanoparticles in the confined space.[38]

As regards inverse miniemulsions, two main synthetic approaches are generally exploited: the co-homogenisation and the diffusion approaches (Figure 2.1.7A and Figure 2.1.7B respectively).

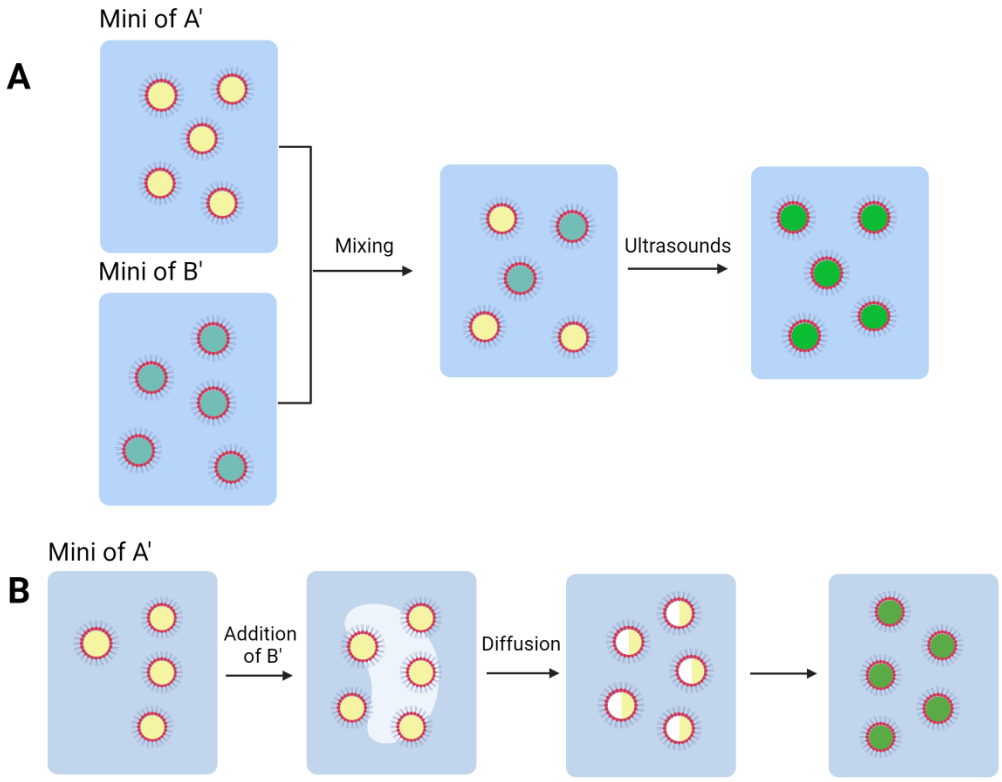

Figure 2.1.7: co-homogenisation approach (A) and diffusion approach (B).

As regards the co-homogenisation approach, the miniemulsions of the inorganic precursors are mixed together, and they will maintain their identity thanks to their high stability. Then, ultrasounds are applied, starting the droplets' fission and fusion processes that lead to the mixing of the reagents inside the droplets, thus allowing the reaction to start and the formation of nanoparticles within the confined space. On the other hand, the diffusion approach involves the formation of the miniemulsion of one of the reagents, while the precipitating agent is added to this miniemulsion as a water solution. This solution will eventually diffuse inside the water droplets through the surfactant layer, causing the reaction to start.[21] Within the work of this thesis, variations and combinations of these two synthetic approaches were applied to synthesise the yttrium vanadate, as the synthesis of this matrix proceeds through an amorphous intermediate that complicates the synthetic route. This because the fast precipitation of the amorphous intermediate and the importance of the order of addition of the reagents (vanadium and yttrium precursors and sodium hydroxide) complicates the exploiting of just one synthetic procedure, requiring the setting of an ad hoc procedure. The synthetic approaches designed and exploited are further discussed in paragraph 6.3.

2.2 Mesoporous materials

2.2.1 General definitions

Porous materials comprise a wide range of materials, from zeolites to porous metal oxides and porous metal-organic frameworks (MOFs).[39] Ordered porous materials have drawn a lot of interest in the last years thanks to their role as promising model materials in several fields, such as heterogeneous catalysis,[40] photocatalysis,[41] adsorption of pollutants from wastewater, and electronic devices.[42] The most important feature of this type of materials is their large and easily accessible surface area. For actual applications, it is important to control and optimize several properties of these materials, the most important being structure, morphology, and porosity.[43] A porous material is defined by IUPAC as "a solid matrix composed of an interconnected network of pores filled with a fluid (gas or liquid)",[5] and based on its pore size it can be classified in three different categories: macroporous materials, ($d > 50$ nm), mesoporous materials, ($2 < d < 50$ nm), and microporous materials ($d < 2$ nm). Going from the former to the latter type of porosity, an increase in pore accessibility is found, but at the cost of a decrease in surface area. Bigger interconnected pores allow an easier and more facile diffusion of the species in the pore network, while smaller pores provide a higher specific surface area.

The first materials studied in the field of porous materials belong to the class of zeolites, which were exploited in several fields, from catalysis to drying agents,[44] and their typical microporosity is given by the formation mechanism itself.[45] However, despite the fundamental importance of these materials, their application is restricted to specific areas because of the small dimensions of the pores (ca. 3-15 Å), which make these materials unsuitable when the reactants' or other involved species' molecules or nanoparticles exceed the pores' diameter. In the last years, many new zeolite-like materials obtained by comprising other elements in the structure other than aluminum and silicon have been developed, with pores of diameter up to 200 Å, still too narrow to be exploited in new applications.[45] For this reason, the synthesis of the so-called M41S materials (mesoporous silica) possessing a pore diameter of about 4 nm by the Mobil Oil company was a breakthrough.[46] After this discovery, the synthesis of mesoporous materials has been a field of intensive research.

2.2.2 Preparation of mesoporous materials

Sol-gel synthesis is one of the simplest and most spread techniques to prepare nanoporous, i.e. microporous or mesoporous, materials thanks to its several advantages, among which are its low cost, ease of implementation, the better control over texture, size, and surface properties of the material,[14,47] and the possibility to start from homogeneous precursor, thus allowing to operate with lower temperatures and shorter reaction times with respect to solid state synthesis.[48] The formation of the sol occurs through the hydrolysis and partial condensation of the metal precursor as shown in Equation 2.1 and Equation 2.2 (which apply in the case of metals and semimetals in oxidation state 4).

$$MX_4 + nH_2O \longrightarrow MX_{4-n}(OH)_n + nHX\,, \qquad X = OR, Hal, etc. \tag{2.5}$$

$$2MX_3OH \longrightarrow X_3M - O - MX_3 \tag{2.6}$$

The following polycondensation step leads to the formation of the gel via the formation of metal-oxo-metal or metal-hydroxy-metal bonds.[48] In this step, the relative rates of hydrolysis and condensation determine the resulting gel structure. These two processes depend on the nature of the X group, the ratio of water to precursor, and the presence and nature of a catalyst. Both processes can be carried out in acidic or basic conditions, thus altering the outcome: in acidic conditions, the hydrolysis step becomes slower as the reaction proceeds, while in basic conditions the opposite happens for a matter of stability of the intermediate ($MX_{4-n}(OH)_n$). Therefore, in basic conditions the degree of hydrolysis of the precursor is higher than in acidic conditions, leading to a higher number of hydroxide groups that can undergo the condensation process. This leads to the formation of a crosslinked gel in the basic scenario, while in the acidic one, the formed gel is more chain-like. In the case of silicon, the use of a catalyst to accelerate the reaction is needed as the reaction at autogenic pH is very slow. On the other hand, another important issue arises when the sol-gel synthesis is applied to transition metals, the most used ones being titanium and zirconium: these elements have lower electronegativity than silicon, and therefore they possess a higher partial charge. Since hydrolysis proceeds through a nucleophilic attack, the higher positive partial charge makes these elements more reactive to this process, up to the point that it is necessary to slow down this reaction in order to carry out the sol-gel synthesis, by adding multidentate ligands or reducing the content of water.[48]

Within the sol-gel approach to obtain nanoporous materials, two main approaches have been developed in the last decades, namely the *endotemplating* (or soft templating) and the *exotemplating* (or hard templating). Endotemplating is frequently used to prepare nanoporous – micro- or mesoporous – materials, which exploits flexible nanostructures as soft templates, such as surfactants, flexible organic molecules, and block copolymers.[49] In endotemplating, the dissolution of the directing agent in the solvent is of fundamental importance to form ordered mesoporous materials. This because the interactions between the inorganic precursor and the templating species, which usually consist of weak intermolecular bonds, have to be favorable, otherwise, a phase separation occurs and no templating can be reached. Two main strategies are possible for obtaining the porous materials with this method: the cooperative self-assembly and the "true" liquid-crystal, depicted in Figure 2.2.1A and Figure 2.2.1B respectively.[50] The former involves an assembly of precursor and template molecules in small groups, like the building blocks of the hybrid structure, which then aggregate into bulkier structures. On the other hand, in the liquid-crystal strategy, the surfactant molecules form semi-liquid or true crystal mesophase out of micelles, around which the growth and condensation of the inorganic precursor can occur. Usually, this latter method requires a higher concentration of surfactants. Most likely, a combination of the two processes governs the synthesis of these hybrid materials. In both cases, the system undergoes a process of self-assembly, generally defined as the spontaneous organization of materials via non-covalent

bonding and without external intervention.[51] After condensation, the organic template is removed either by calcination or by dissolution, and the inorganic mesoporous structure is obtained, essentially like a fossil of the liquid-crystalline assembly.[50]

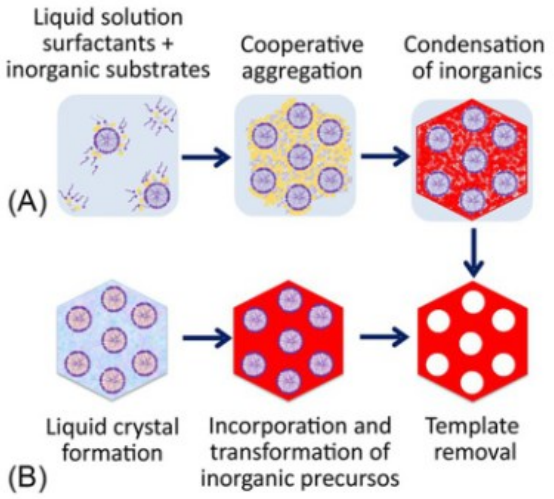

Figure 2.2.1: Scheme of the two possible strategies for the soft templating method: cooperative self-assembly (A) and "true" liquid-crystal (B).[49]

A particular case of soft templating which has been exploited for the synthesis of the mesoporous metal oxides used within this thesis is represented by the *Evaporation-Induced Self-Assembly* (EISA). This method is mainly used for the synthesis of thin films, usually coupled with different coating techniques like dip-coating or spin-coating,[52] but it can also be exploited to obtain mesoporous powders. The main reaction that takes place in the EISA process is again the sol-gel synthesis. Indeed, the initial solution must fulfill the requirements of a controlled sol-gel system, that is the hydrolysis and condensation step must be set as in a usual sol-gel synthesis by adjusting the precursors' concentrations and the quantity of the catalyst. Usually, the preferred solvent is ethanol, thanks to its high volatility and high wettability with hydrophilic substrates.[52] Then, the driving force of this entire process is the evaporation. During solvent evaporation, the concentration of the non-volatile substances, such as the metal precursor and the surfactant, increases, leading to the self-assembly of the hybrid material into a liquid crystal phase.[53] As soon as the concentration of the surfactant reaches the *critical micelle concentration* (CMC), micelles start forming and the inorganic framework starts condensing around them, in a phase called *tunable steady state* (TSS). In this stage, volatile molecules are in equilibrium between the system and the environment, and therefore the composition of the system can be controlled by changing the relative humidity (RH). Finally, a post-synthesis treatment step is required: the template is removed (calcination, dissolution or soxhlet) in order to provide the porosity to the inorganic framework and to stabilize it by further condensation.[52,53] Pore size and pore wall thickness depend on the template used and on the relative concentrations between inorganic precursor and surfactant. A schematic representation of an EISA process is illustrated in Errore. L'origine riferimento non è stata trovata..2.

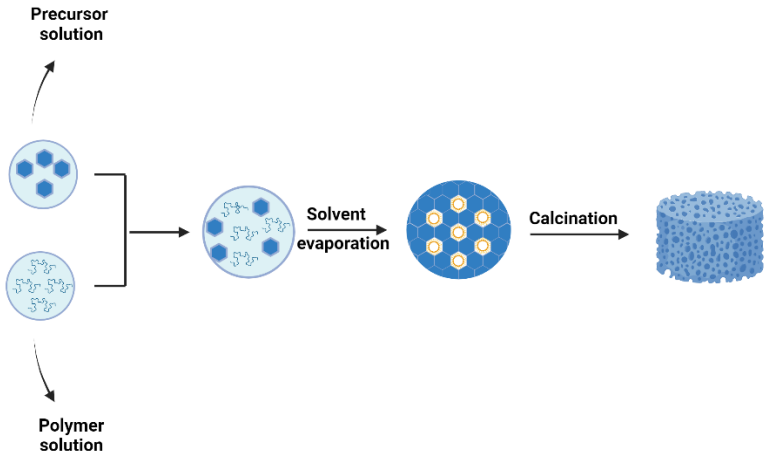

Figure 2.2.2: Schematic representation of the EISA process.

On the other hand, the exotemplating (or hard templating) synthetic route is another well-known procedure to obtain mesoporous and macroporous materials, which exploits rigid, pre-formed templates made of aggregates of nanoparticles or porous materials themselves as scaffolds, in which the product can grow. Since the template is not flexible, this synthetic route overcomes the problems associated with the control of the hydrolysis and condensation of the inorganic precursor and its interaction with the surfactant.[50] Indeed, the morphology of the product is defined by the morphology of the hard template, since its pores are filled with the precursor molecules to form the product. Eventually, the scaffold is eliminated (for instance by etching) to obtain the bare product.[49] The advantage of this synthetic route is that highly crystalline or even single-crystal materials can be obtained, thanks to the resistance of the hard scaffold to high temperature treatments. Nevertheless, this method has some disadvantages, such as the presence of only a few possible hard templates which makes the choice of the right scaffold more difficult with respect to soft templating, and also the higher cost and smaller yield.[49,50] A summary representation of the hard templating technique is provided in Errore. L'origine riferimento non è stata trovata..

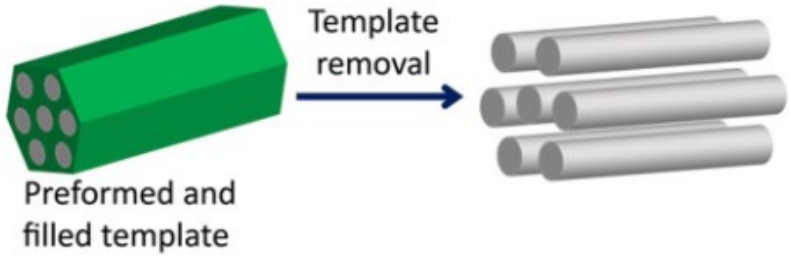

Figure 2.2.3: Schematic representation of the hard templating technique.[49]

2.2.3 Mesoporous materials as confined space nanoreactors

Among all the possible applications of mesoporous materials, there is also the possibility of exploiting the confined environment represented by their pores as nanospaced confinement for a reaction. For example, mesoporous materials can be exploited for the synthesis of supported noble metals nanoparticles for catalysis,[54] but they can also be used for the synthesis of other inorganic species. The properties of the product, such as crystalline phase, size, and shape of the particles, depends not only on the exploited support but also on the efficient dispersion of the precursors into the pore network. Thus, particular care must be taken when the loading of precursors into the porous matrix is considered. There are several preparation methods of the loaded matrix to then carry out a reaction in mesoporous materials, such as reductive deposition, colloidal synthesis or deposition by precipitation,[54] but the most diffuse is the impregnation method. This last method involves three different phases: i) *impregnation step*, in which the pores of the mesoporous material are filled with the precursor's solution; ii) *drying step*, where the solvent is evaporated from the mesoporous material, and iii) *activation step*, which involves a calcination and/or reduction step if necessary. Among these three steps, the first two are those which mainly affect the impregnation profile and therefore the distribution of the impregnated species inside the pores.[54] As regards the impregnation step, two different mechanisms can be followed: the incipient wetness impregnation (IWI) or the wet impregnation (WI). In the first case, the dry support is impregnated with a volume of solution that is exactly the same as the pore volume of the material (determined with techniques such as the N_2 physisorption), so that no exceeding solution is present. In the second scenario, the dry support is immersed in an excess volume of solution and stirred for hours or days. The major drawback of the second method is the preferred adsorption of precursor onto the external surface of the support and not into the pore system.[54] The solution enters the pore system due to the capillary pressure, and once it has entered the pore system, adsorption and diffusion of the precursor on the support's surface begins.[54] However, trapped air may hinder this process, as the pressure of the trapped air can oppose to the capillary pressure: pores with a small diameter possess a higher capillary pressure, thus resulting in a more efficient impregnation step. Several models, depending on the type of gas and on the mesoporous material exploited, that describe the dependence of capillary pressure on different parameters can be found in literature.[55] The optimal conditions for the adsorption of the precursor depend on the surface polarity of the support, the polarity of the solvent and the solubility of the precursor in the solvent.[56] For example, for a support with a high density of polar functions on the surface (e.g. silica), a polar solvent involves a higher degree of wettability and therefore a convenient diffusion of the precursor. To optimise the impregnation step, the interactions between the precursor and the support should be maximised, usually through electrostatic interactions. In the last years, the methods named *Strong Electrostatic Adsorption* (SEA), and *Charge-Enhanced Dry Impregnation* (CEDI)[6] have been developed. In these two methods, the pH of the system (impregnating solution and support) is varied out of the point of zero charge (PZC) of the support in order to maximise the electrostatic attraction between the support itself and the precursor. The difference between the two methods relies in the quantity of impregnating solution: SEA exploits an excess of solution, while CEDI has no exceeding solution, as in IWI.[54] Figure 2.2.4 summarises the four possible cases. In general, if multiple components have to be adsorbed, the process can be either simultaneous, where an impregnating solution containing every species is exploited, or sequential, where each species is adsorbed individually.

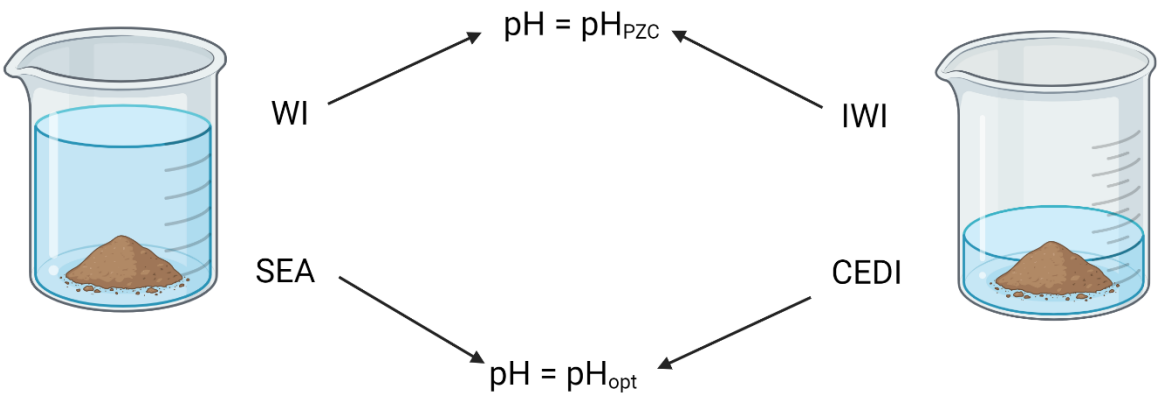

Figure 2.2.4: schematic representation of the possible impregnation mechanisms. WI: wetness impregnation; IWI: incipient wetness impregnation; SEA: strong electrostatic adsorption; CEDI: charge-enhanced dry impregnation: pH_{PZC}: pH of point of zero charge; pH_{opt}: pH optimal

The subsequent step is represented by the drying step. In this scenario, before the drying process, the pores of the support are filled with the impregnating solution, and the precursor is present both as adsorbed phase on the pores' wall and in the liquid phase in the pores' volume.[54] During the drying step, the solvent is transported outside the pore system by capillary flow and diffusion,[55] and in the process, the target precursor species is redistributed depending on its adsorptivity. For this reason, a controlled drying process is usually preferred.[54,57] Within the work of this thesis, mesoporous silica, zirconia and titania were exploited as mesoporous metal oxides for model confined space. The inorganic precursors were adsorbed in the pore system through the IWI technique.

3 YTTRIUM VANADATE

3.1 Structural and physical-chemical properties

In the last decades, yttrium vanadate – YVO_4 – has been extensively studied thanks to its several applications, since it is both a good luminescent material, especially when doped with trivalent lanthanides ions, and a semiconductor. Yttrium vanadate can be exploited in fields such as polarisers, laser host materials, phosphors and optoelectronics.[58–60] Besides, it possesses excellent thermal and chemical stability.[61]

Yttrium vanadate occurs in nature as wakefieldite mineral, and it belongs to the family of zircon-type materials, with general formula $M^{+m}N^{+(8-m)}O_4$, where *M* and *N* are metal ions with coordination numbers of eight and four, respectively.[62] The crystalline structure of yttrium vanadate (**Figure 3.1.1**) is a tetragonal zircon-type structure, with $I4_1/amd$ space group and D_{4h}^{19} point-group symmetry.[62] More in detail, YO_8 dodecahedra share edges to form chains along the <100> direction, and the same occurs for VO_4 tetrahedra. (**Figure 3.1.2A**) Moreover, YO_8 and VO_4 form alternated edge-connected chains parallel to the <001> direction (**Figure 3.1.2B**).[63]

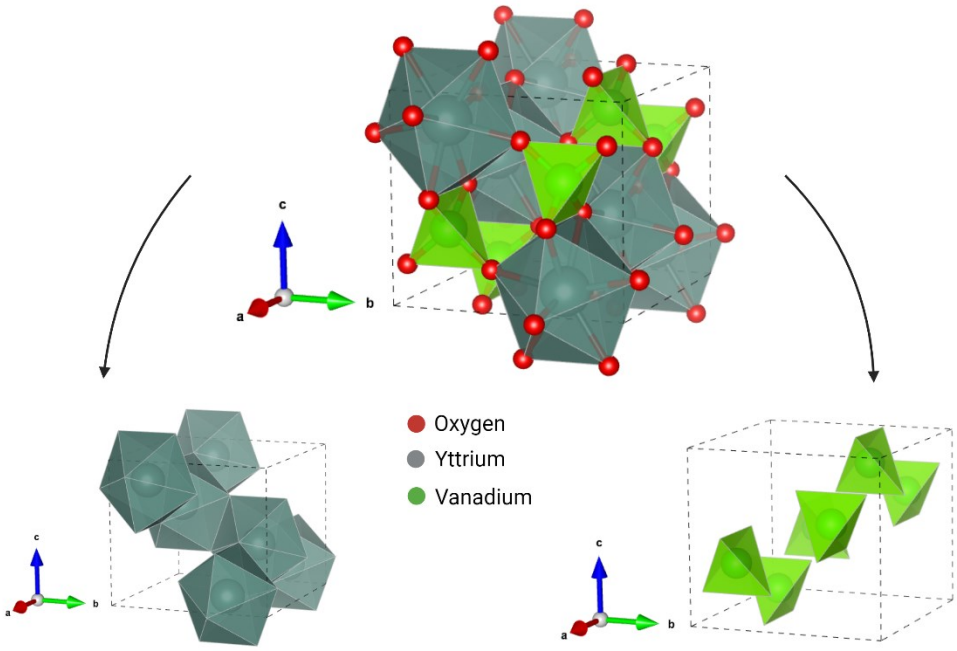

Figure 3.1.1: Crystal structure of YVO_4. Separated polyhedra of oxygen around yttrium and vanadium atoms are also depicted.

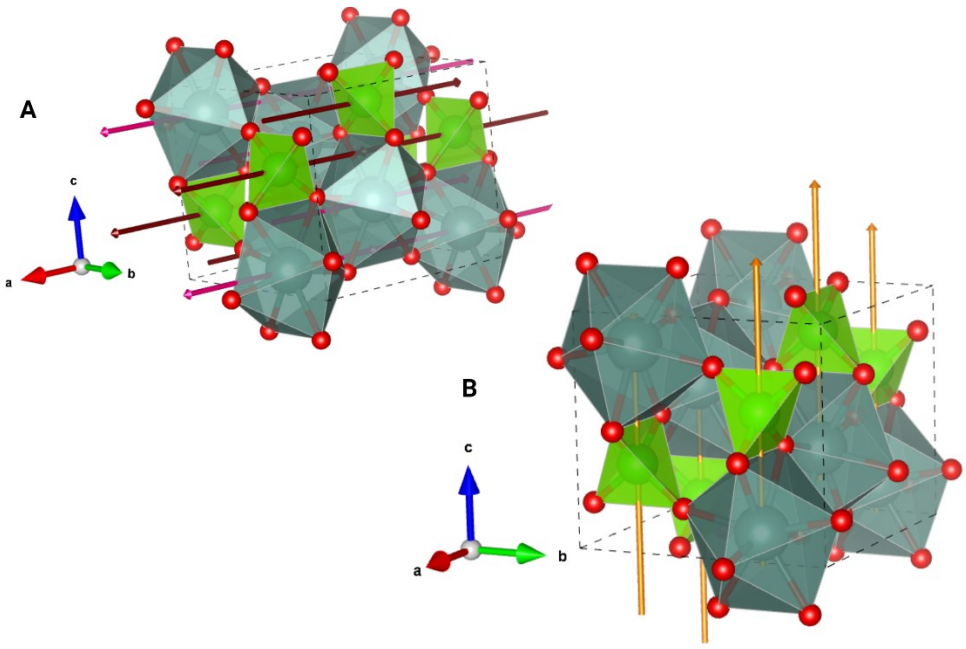

Figure 3.1.2: Crystallographic vectors <100> (A) and <001> (B).

The VO_4 tetrahedra are based on the orthovanadate ion VO_4^{3-}. In free space its group symmetry is T_d, but when considered in a crystal, the crystal field reduces the symmetry to the D_{2d} group.[64] The YVO_4 structure can be considered as composed of ionic interactions between the Y^{3+} ion and the orthovanadate molecular ions, thus allowing the division of vibrational modes in internal, i.e. due to vibration modes of the orthovanadate ion, and external modes, which involve translations and rotations of the VO_4 tetrahedra as a whole with respect to the yttrium ion.[65] Group theory predicts twelve parity even phonons for the zircon-type structure, which are all Raman active.

The formation of YVO_4 in solution occurs through a precipitation reaction between the Y^{3+} and VO_4^{3-} ions, proceeding via an intermediate amorphous step as described more in detail in Paragraph 3.2. Moreover, when the synthesis of yttrium vanadate is carried out in an aqueous solution, the pH plays a fundamental role, as the behaviour of both ions in solution depends on the pH of the solution itself. As regards the Y^{3+} ion, present in water solution as $Y(H_2O)_8^{3+}$, pH values higher than 6 cause the hydrolysation to occur with the precipitation of $Y(OH)_3$, an amorphous white solid.[66] As regards the behaviour of vanadium in aqueous solution, the most common oxidation numbers for vanadium in solution are III, IV, and V, and each of these oxidation states possesses its own different chemistry. The difference is readily visible in Figure 3.1.3, where it can be noted that vanadium (V) is the only oxidation state forming anionic species, such as $VO_2(OH)_2^-$. As regards the vanadium (V) behaviour in aqueous solutions, it exists primarily in monomeric forms, especially in dilute solutions, which can be expressed by the general formula $H_\alpha VO_4^{(3-\alpha)-}$, with α being an integer value between 0 and 3. However, in more concentrated solutions, monomeric vanadate readily undergoes condensation reactions with nucleophiles, including other vanadate species. Indeed, in a solution with millimolar or higher concentrations of vanadium, the major species present in the solution are vanadium oligomers. The predominant oligomer present at pH between 3 and 6 is $V_{10}O_{28}^{6-}$, but at different pH values other oxoanions or vanadium oligomers (polyoxoanions) can be

present.[67] However, these species can easily convert back to the monomeric species upon dilution or other processes.

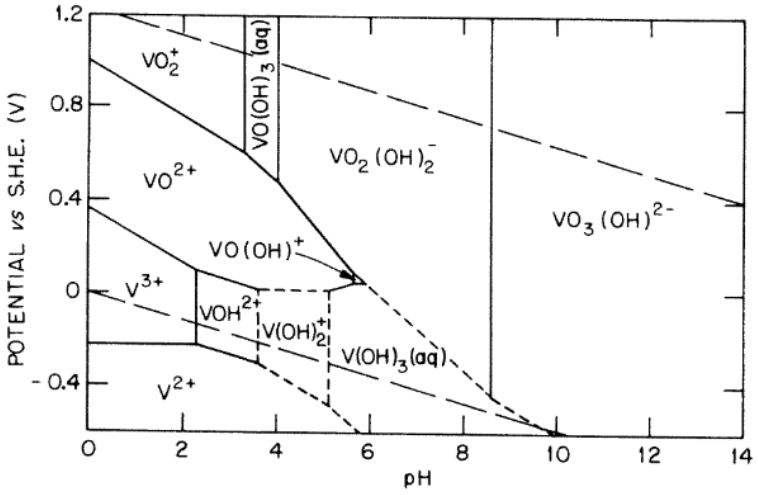

Figure 3.1.3: Diagram for potential vs. pH for dilute vanadium solution at 25 °C.[66]

3.2 Crystallisation through an amorphous intermediate: the Ostwald's step rule

For many years the so-called "classical nucleation theory" (CNT) has been the only theory present to describe the crystallisation of inorganic compounds in solution. Briefly, the crystallisation of a compound is composed of two phenomena: nucleation and growth. As stated by *Karthika et al.* nucleation is the process in which a new thermodynamic phase forms, from an old phase with high free energy to an organised structure with low free energy.[68] The thermodynamic description of this process is provided by Equation 3.1:[68,69]

$$\Delta G = -\frac{4\pi r^3}{3v} KTlnS + 4\pi r^2 \sigma \qquad \textbf{3.1}$$

where *K* is the Boltzmann's constant, *T* is the absolute temperature, *v* is the volume of a single molecule, *σ* is the specific surface energy [N·m^{-1}] of an interface between the two different faces and *S* is the vapour supersaturation ratio (adimensional). The first term lowers the free energy by considering the energy yield obtained when atoms aggregate together in a regular shape, and the second term increases the free energy by considering the higher energy introduced by the new interface. As can be noted by Equation 3.1, the sign of the ΔG of nucleation depends on the ratio surface over volume. A critical radius can therefore be defined, at which the probability of the formation of a nucleus is minimal because of the highest value of ΔG (Figure 3.2.1).

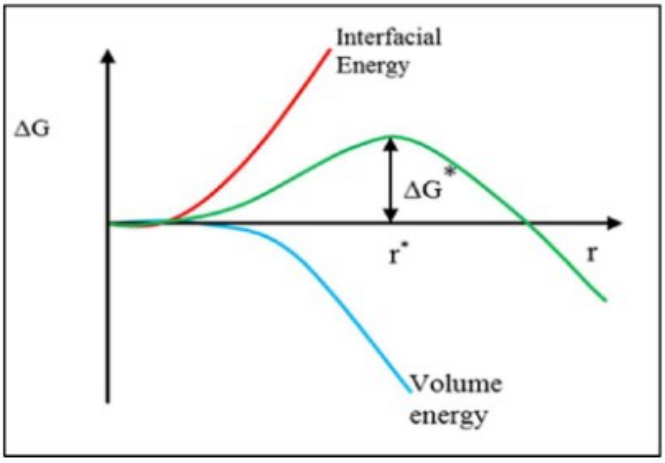

Figure 3.2.1:Thermodynamic behaviour of the nucleation with dependence on the radius.[68]

The value of the critical radius is not fixed but depends on the concentration of the solution: the higher the concentration, the smaller the critical radius and therefore the easier to obtain stable nuclei. One of the most famous and exploited classical nucleation and growth models is the LaMer burst model[70], which considers the formation of the nuclei as a swift, homogeneous, and simultaneous process. A valid implementation of this model is given by Sugimoto[71], who hypothesised that nucleation and growth are two separate events, and that the nucleation rate only depends on the concentration of the solute and not on the kinetics of this process.[72]

However, the CNT fails to provide a good picture of the formation of inorganic crystals, especially when intermediate phases are involved, like in the case of yttrium vanadate. Thus, new nucleation theories (such as the Non-Classical Nucleation Theories (NCNT)) have been developed to better describe these systems. One further relevant theory is the Ostwald's step rule, which states that during the transformation of an unstable or metastable system into a thermodynamically stable one, the system does not go directly to the most stable configuration, but proceeds through intermediate stages having closer free energy to the initial stage, and therefore are kinetically favoured (Figure 3.2.2).[73]

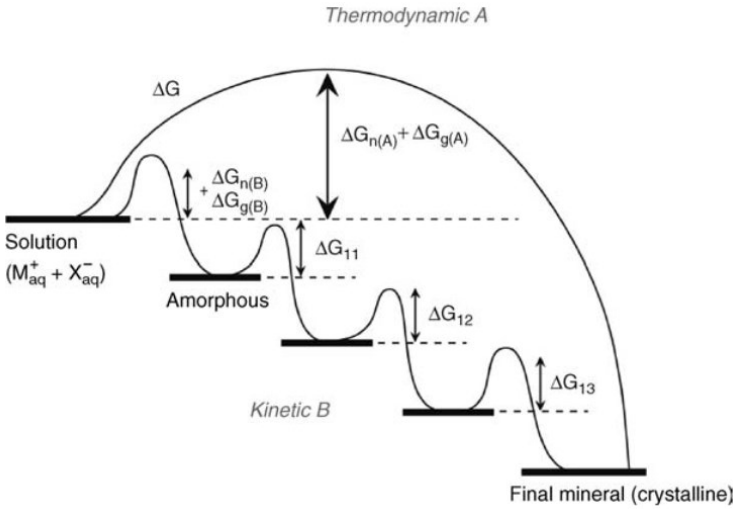

Figure 3.2.2: Visual interpretation of the Ostwald's step rule.[74]

This theory allows to describe more complex crystallisation pathways, considering not only the thermodynamic aspect of the crystallisation but also the kinetic one. Kinetically driven crystallisation often involves an initial amorphous phase that may also be nonstoichiometric or hydrated, which eventually undergoes a phase transformation.[74] Moreover, the kinetic control of the crystallisation of inorganic compounds can lead to the selection of particular polymorphs of the compound by varying the crystallisation conditions. This applies also for the yttrium vanadate system, for which the crystallisation pathway starts with the precipitation of the amorphous yttrium hydroxide. Eventually, yttrium hydroxide reacts with the orthovanadate species present in solution to form the yttrium vanadate crystal structure. The interesting aspect is the possibility to combine this crystallisation pathway through an amorphous intermediate with the emission of lanthanide ions, which emit only when they are embedded in a crystalline matrix. Indeed, lanthanides ions embedded in a crystalline matrix can lead to the antenna effect, that is receiving the energy transfer from the host matrix and eventually relax to the ground state by radiative processes. Thus, when the amorphous yttrium hydroxide precipitates, no luminescence of the lanthanides' ions can be detected because the antenna effect cannot happen. On the other hand, when the crystallisation of this amorphous intermediate proceeds towards the formation of crystalline yttrium vanadate, a luminescence signal can be measured, therefore allowing the study of the crystallisation mechanism and kinetic of yttrium vanadate by means of lanthanide luminescence.[75]

3.3 Synthesis of yttrium vanadate: state of the art

As stated in Paragraph 3.1, yttrium vanadate has been largely investigated thanks to its thermal and chemical stability, and thanks to its photoluminescence properties. Moreover, it is well known that these latter depend not only on the type of lanthanide ion, which determines the wavelength of emission, and its distribution in the matrix, but also on the size and morphology of the particles.[76] Indeed, in recent years research efforts have been made to better understand the effects of quantum confinement on the physical-chemical properties of crystalline nanophosphors, such as their band gap or their photoluminescence properties.[77] For this reason, in past years several ways to synthesise yttrium

vanadate nanoparticles have been developed, such as hydrothermal synthesis,[78] sol-gel method,[79] sonochemical process,[80] microemulsions,[81] microwave assisted synthesis,[82] Pechini method,[83] or through solid state approaches, e.g. thermal annealing.[84] These different methods led to different morphologies and particle sizes of yttrium vanadate, highlighting the possibility to efficiently control the outcome of the reaction and the photoluminescence properties of the nanoparticles. The synthesis of doped yttrium vanadate incorporated in mesoporous thin films has also been reported.[85] To date, the synthesis of undoped and Eu(III)-doped yttrium vanadate via inverse miniemulsion approach or by exploiting the reaction of educts impregnated in mesoporous matrix have not been reported in the literature.

3.4 Optical properties of non-substituted and Eu(III)-substituted YVO_4

Yttrium vanadate possesses intrinsic luminescence properties, and its optical spectrum is due to optical transitions within the VO_4^{3-} ion.[86] The orthovanadate ions possess a T_d symmetry, but when inserted into the YVO_4 crystal, its symmetry is reduced to D_{2d} by the crystal field. This causes a splitting of the energy levels of the excited state, $^1A_1$, ^1E, and $^1T_2$ that would otherwise be degenerated, bringing to five excitation bands centred at 330, 320, 305, 262.5 and 252 nm respectively. These bands are generated from the transition between the $^1A_2$ component of the ground state and one of the states of the excited state (Figure 3.4.1). Transitions to the $^1B_2$ levels are forbidden. The excited levels then relax to the less energetic level of the excited state and eventually decay back to the ground state, generating the broad fluorescence band.[86]

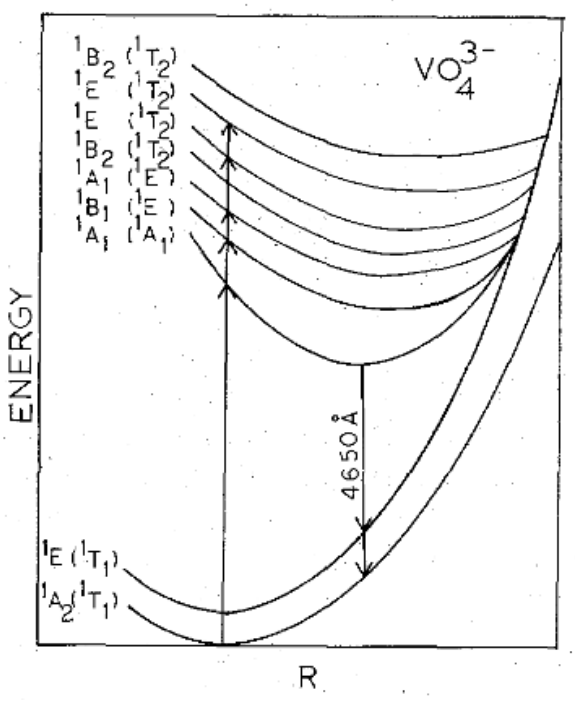

Figure 3.4.1: Energy levels for the VO_4^{3-} ion in the YVO_4 crystal.[86]

As regards the temperature dependence, non-substituted YVO_4 presents a blue emission centred at 420 nm at temperatures below 200 K.[87] At temperatures higher than 100 K, energy migration to traps starts occurring, decreasing the intensity of the emission. A similar temperature dependence is found regarding the decay time, but, as stated by *Blesse et al.*, this behaviour is attributed to an increase in the relevance of non-radiative processes from the lowest excited state of the vanadate ion. More in detail, they suggest that at high temperatures, vibrational modes of the vanadate ion may distort the symmetry, thus allowing symmetry selection rules to relax.[88] The luminescence properties of the vanadate ion are due to a ligand-to-metal charge-transfer (LMCT) transition,[89] involving the HOMO (highest occupied molecular orbital), composed of nonbonding O 2p orbitals with a t_1 symmetry, and the LUMO (lowest unoccupied molecular orbital) and SLUMO (second lowest unoccupied molecular orbital), composed of the linear combination of the antibonding V 3d and O 2p orbitals, with e and t_2 symmetry respectively.[90] When considering a crystal, these molecular orbitals build up the valence and conduction bands respectively. Besides, when varying the cation associated with the vanadate anion, the different electronic configurations of the cations may interact differently with the vanadate orbitals, leading to differences in the band gap energies and therefore in the luminescence properties of the crystal.[91] For example, Y^{3+} possesses a noble gas like electronic configuration and therefore does not electronically interact with the vanadate ion, and the YVO_4 crystal presents a band gap of about 3.5 eV.[92] Moreover, the vanadate anion has been reported to possess a more efficient energy transfer to doping ions as compared to similar anions (e.g. PO_4^{3-}) since for vanadate the transition from the lowest excited state $^1A_1$ to the ground state is symmetry forbidden, making the excited state metastable and therefore able to transfer efficiently the energy to a dopant ion.[93]

Yttrium vanadate has been extensively reported to be an excellent host matrix for the development of lanthanide-based phosphors.[78] This arises not only from the presence of the vanadate ion possessing good luminescence properties and energy transfer features as described above, but also from the presence of the Y^{3+} ion. Indeed, this ion possesses structural properties that are very similar to those of many trivalent lanthanides ions: *i*) the same charge, that allows the substitution with Ln(III) ions, the most abundant oxidation state for lanthanides, without the need for charge compensation mechanism; *ii*) a similar ionic radius, e.g. Eu(III) with ionic radius of 1.066 Å and Y(III) of 1.019 Å (in eightfold coordination).[94] These similarities allow the substitution of Y(III) ions with Ln(III) ions without major changes in the structure of the crystal.[62] For these reasons, YVO_4 has been exploited as host matrix for the statistical substitution of several lanthanide ions, such as Tb^{3+}, Sm^{3+}, Dy^{3+}, Nd^{3+} and Eu^{3+}.[95] The high efficiency of this host matrix with respect to the energy transfer can be explained by quantum mechanical considerations. First, as stated above, the exited $^1A_1$ electronic state is metastable, thus favouring the energy transfer process. Second, the primary excitation of the vanadate ion does not involve an increase in electron density on the vanadium atom, instead the excited electron has its charge distribution shifted towards the outside of the VO_4^{3-} ion in the A_1 state, as confirmed by molecular orbitals calculations.[93] This can further guarantee a good overlap between the excited electron orbitals and the orbitals of the surrounding ions, favouring the energy transfer. As regards the mechanism of energy transfer from the host to the lanthanide ion, two mechanisms are proposed: a single-step, long-range resonance mechanism at low temperatures, and a migration mechanism at high temperatures.[86] Historically, the doping of YVO_4 with Eu(III) ions has been the most exploited to obtain red phosphors, and it is also the

doped system studied within the work of this thesis. The optical properties of Eu(III)-doped YVO_4 present some peculiarities. First, the characteristic intense emission of Eu(III) at 614 nm can be generated either by directly exciting the f-f transitions of the europium ions, or by exciting the matrix at around 280 nm and exploiting the energy transfer to the lanthanide ions. Besides, luminescence spectra of Eu(III) ions can give structural information of the host matrix. In general, f-f transitions of lanthanide ions are not sensitive to the environment of the ion itself, since these f orbitals are shielded by the 5s and 6p outer orbitals. However, some differences can be noted in the luminescence spectra of lanthanides ions due to the different symmetry of their environment, which can cause a different splitting in the energetic levels according to the different symmetry.[96] In the case of Eu(III)-doped YVO_4, the most intense europium emission coincide with the $^5D_0 \rightarrow {}^7F_2$ hypersensitive transition, i.e. a transition which is more influenced by the local symmetry of the Eu(III) ion compared to the others.[95] Besides luminescence spectra profile, excited state lifetime can also highlight structural differences in the local symmetry of Eu(III) ions, for example, the presence of sites of Eu(III) ions with different symmetry or the presence of aggregates of Eu(III) ions. In particular, decay profiles can shed light on the possible decay mechanisms: it has been demonstrated that usually, for concentrations up to 1% at. of dopant ions, the decay profile follows an exponential character, while for higher concentrations the profile is nonexponential, with a shorter lifetime. The latter could be explained by the fact that a higher amount of Ln(III) ions in the lattice may involve a higher probability of ion-ion cross relaxation leading to non-radiative processes.[61]

4 RESULTS AND DISCUSSIONS

In this chapter, the optimisation of the formulation for obtaining stable miniemulsions, as well as the characterisation of the non-substituted and Eu(III)-substituted yttrium vanadate obtained by inverse miniemulsion synthesis and by exploiting the mesoporous matrices are described and discussed. Then, a comparison of the properties of the so-obtained yttrium vanadate with those of yttrium vanadate obtained in non-confined space, i.e. by classical co-precipitation synthesis, is performed, comparing properties such as the crystallinity, crystallites size and morphology of the different products. Finally, the photoluminescence properties of the different products are analysed and compared, highlighting the differences amongst the various synthetic approaches.

4.1 Optimisation of the formulation of miniemulsions

As stated in paragraph 2.1.2 and reported in Figure 2.1.2, miniemulsions are obtained by the combination of an aqueous phase, an organic phase, a surfactant, and an osmotic agent. As regards inverse miniemulsions, the inorganic precursor itself acts as the osmotic agent. In the case of our system, the organic phase was constituted by cyclohexane, and the chosen surfactant was the Span80 (sorbitan monooleate, Figure 2.1.6). The osmotic agent, and therefore the inorganic educt, chosen to test the stability of miniemulsions was the $Y(NO_3)_3 \cdot 6H_2O$. Besides the chemical species, the stability of the miniemulsion also depends on the shear history, that is the intensity and duration of the high shear treatment to which the system is subjected. Thus, the optimisation of the formulation of the miniemulsions involved the variation of both compositional and instrumental variables. Typically, the DLS is a useful technique to study the stability of miniemulsions, since it can provide information on the droplets' hydrodynamic radius. Thus, studying the variation of the droplets' hydrodynamic radius over time, the stability of the miniemulsions can be investigated. However, in our case the DLS instrument could not analyse the original miniemulsions since they resulted too concentrated. Therefore, the miniemulsions were diluted in cyclohexane approximately by a factor 1:100 in order to reduce the background signal. However, by performing the measurements on diluted miniemulsions, i.e. by measuring the droplets' hydrodynamic radius over time (1 hour, 1 day and 2 days after the sonication, as reported in Figure 4.1.1) for all the different formulations, an increment in the droplets' hydrodynamic radius was found, but no significant differences related to the different formulations could be highlighted. Moreover, by diluting the miniemulsion in cyclohexane, only a small portion of the entire miniemulsion was analysed, not accounting for possible differences in various parts of the original miniemulsion, e.g. an incipient phase separation which could cause different droplets' hydrodynamic radii in different parts of the miniemulsion. Therefore, DLS measurements were not suitable for precisely determining the stability of miniemulsions as a function of the different formulations. Since the laboratory was not equipped with instruments such as the viscometer or the turbidimeter to quantitatively determine the stability of miniemulsions, the absence of phase separation observed visually was chosen as empirical method to assess the stability of miniemulsions. An example of a stable miniemulsion and an unstable one is reported in Figure 4.1.2. The reaction time needed for the formation of YVO_4 was chosen as time scale in which no phase separation should occur in order for a miniemulsion

to be defined stable. Thus, several formulation parameters were changed, and the miniemulsions were checked for twenty-four hours after the sonication: if no phase separation was detectable after the 24 h, the formulation could be defined as stable. In the following, a description of the various parameters changed during the optimisation and how they affected the stability of the miniemulsion system is provided.

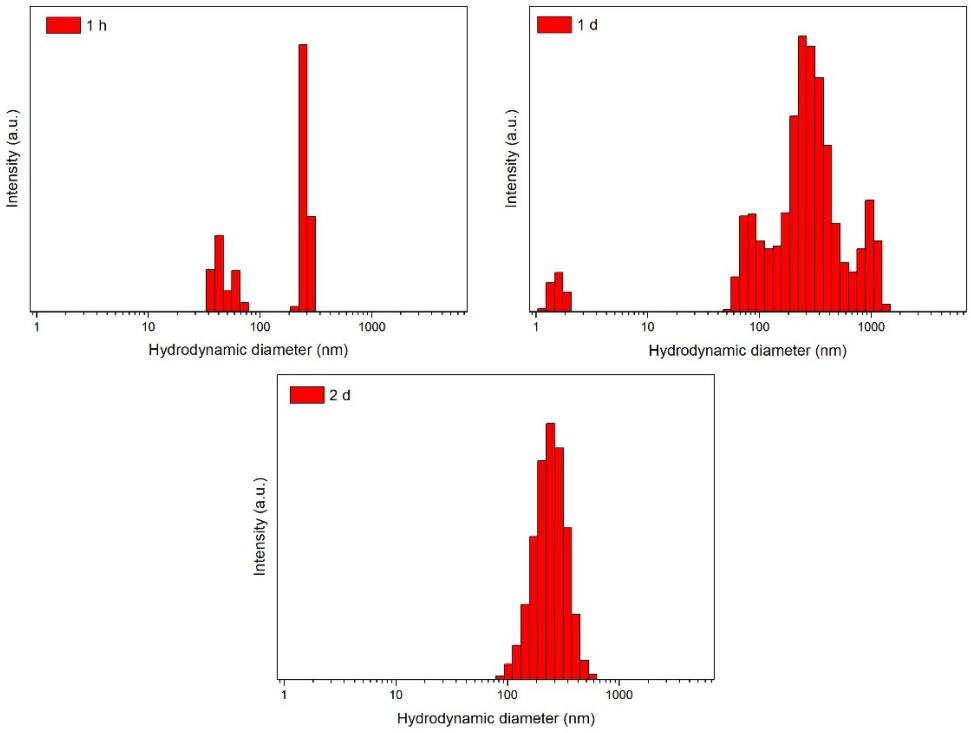

Figure 4.1.1: DLS measurements of the miniemulsion obtained with 3% wt Span80, water:oil weight ratio of 1:3 and 2 minutes of sonication time. The measurements were taken after 1 h, 1 day and 2 days after sonication.

- *Water to oil weight ratio*: keeping fixed all the other parameters, two different water-to-oil weight ratios were tested, that is 1:3 and 1:4. As regards the stability, no appreciable differences could be noted with different water-to-oil weight ratios, thus the 1:3 value was kept for the up following tests. The 1:3 weight ratio was chosen as a lower amount of oil phase and therefore a lower amount of surfactant compared to the aqueous phase should be exploited, thus leading to a reduction in the usage of harmful chemicals (cyclohexane).

- *Surfactant concentration*: the surfactant concentration is defined as its weight percentage with respect to the continuous phase. Three different concentration values were tested, that is 1.5, 2.3 and 3% wt. With concentration of 1.5% wt, the miniemulsion was stable for 5 to 6 hours after sonication, then phase separation occurred. With 2.3 and 3% wt. the miniemulsion resulted stable for the 24 hours of the reaction. Finally, the 2.3% wt value was chosen as reference value for the synthesis, for the reason presented afterwards in paragraph 4.1.1.

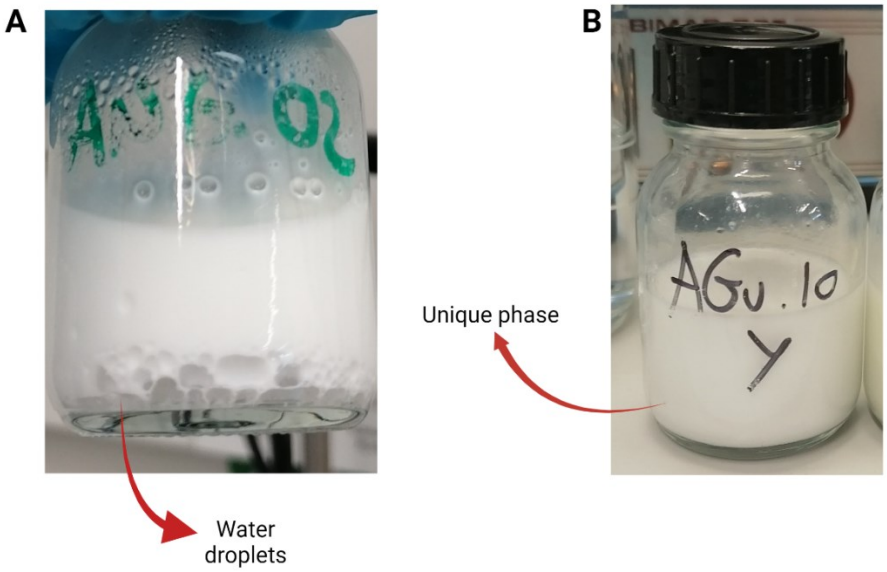

Figure 4.1.2: Comparison between an unstable miniemulsion (A) and a stable one (B).

- *Ultrasonication power applied*: the ultrasounds were applied at three different power values, that is 50, 60 and 70% of the maximum amplitude of the instrument (550 W) and using the 3 mm titanium tip. By applying the two higher values of power, the obtained miniemulsions were not stable for more than 1 h, probably due to a too high energy supplied to the system or a too high reached temperature, both of which could probably lead to a disruption of the surfactant (due to the high energy involved in the sonochemical approach[97]). With high sonication powers, high temperatures were reached also if an ice-bath was exploited, probably because the energy supplied with high sonication powers was more than the energy dissipated thanks to the ice-bath. Whit 50% of applied power, the resulting miniemulsions were instead stable for over 24 h, hinting at a successful formation and stability of the miniemulsion.

- *Total sonication time*: the total time of sonication was changed amongst 2, 5 and 15 minutes. Of these, miniemulsions obtained with 2 minutes of sonication time were the only ones stable for more than 24 h. Again, this is probably due to a too high total energy transferred to the miniemulsion syste upon prolonged sonication, which may cause the disruption of the surfactant molecules with consecutive instability of the formed droplets.

4.1.1 *Stability of the miniemulsions*

As anticipated in paragraph 2.1.3, inverse miniemulsions should be extremely stable with respect to the diffusion of reagents amongst the droplets. Thus, when two miniemulsions are mixed, the resulting miniemulsion should be a simple mixture of the two independent starting miniemulsions until ultrasounds are applied again to favour fusion of the droplets and therefore the mixing of the matter inside the different droplets. As it was previously noticed by carrying out the batch reaction between $Y(NO_3)_3 \cdot 6H_2O$ and NH_4VO_3 solutions, the reaction mixture turns yellow immediately as the two reactants are added, and a yellow precipitate is formed. Thus, in the corresponding miniemulsion system, the miniemulsion obtained by mixing the two miniemulsions of the educts should be of a white colour until

ultrasounds are applied, turning the miniemulsion to a yellow colour. However, it was found that the colour changed immediately to yellow when the two miniemulsions of the reagents were mixed even if no ultrasounds were applied, hinting at a spontaneous exchange of matter amongst the droplets. Figure 4.1.3 summarises the theoretical and experimental process of the reaction.

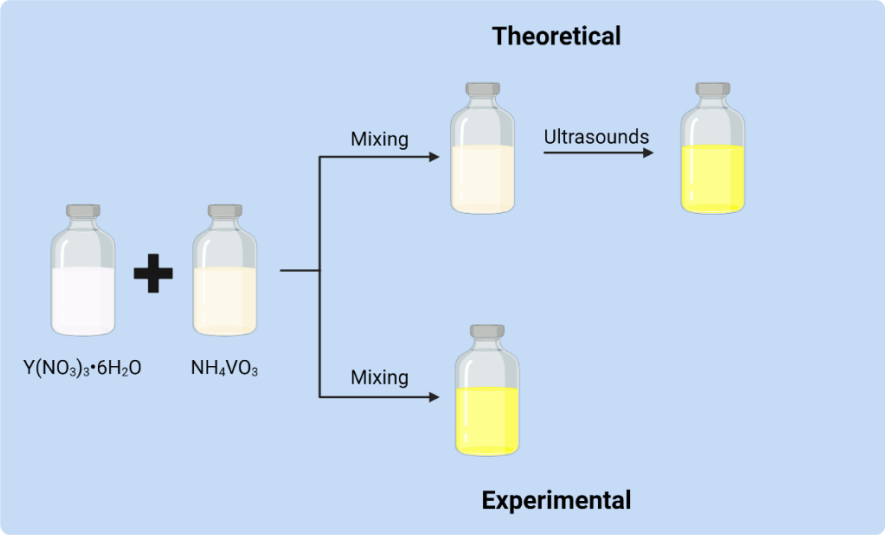

Figure 4.1.3: Schematic representation of the theoretical and experimental process of the synthesis with the specific educts and a comparison between the theoretical and experimental outcomes. In the figure, only miniemulsions are reported.

This behaviour of the system was found with all the different formulations tested for the stability of miniemulsions, that is different surfactant concentrations and different sonication times. In order to assess whether this inter-droplets matter exchange was a particular scenario of the studied system (synthesis of YVO_4) or if it was a problem related to the specific optimised miniemulsion formulation, and therefore it is observed also with an already established reaction, the synthesis of Prussian blue in miniemulsion, following the process described by *Antonietti et al.*,[3] was carried out. In this synthesis, the two reagents, that is $FeCl_3$ and $K_4[Fe(CN)_6]$, are mixed and the dark blue product $Fe_4[Fe(CN)_6]_3$ precipitates, following the reaction described in Equation 4.1:

$$FeCl_3 + K_4[Fe(CN)_6] \rightarrow Fe_4[Fe(CN)_6]_3 \qquad \textbf{4.1}$$

In the miniemulsion system, the two starting miniemulsions should be mixed and retain a pale-yellow colour until ultrasounds are applied, allowing the precipitation of the Prussian blue and therefore causing the miniemulsion to turn dark green (due to the blue colour diluted in the miniemulsion system). However, also in this case, the mixed miniemulsion turned dark green by simple mixing and stirring and without the application of ultrasounds, as depicted in Figure 4.1.4, with the difference that the colour change happened in a period of 4-5 h and not immediately as in the case of the synthesis of YVO_4.

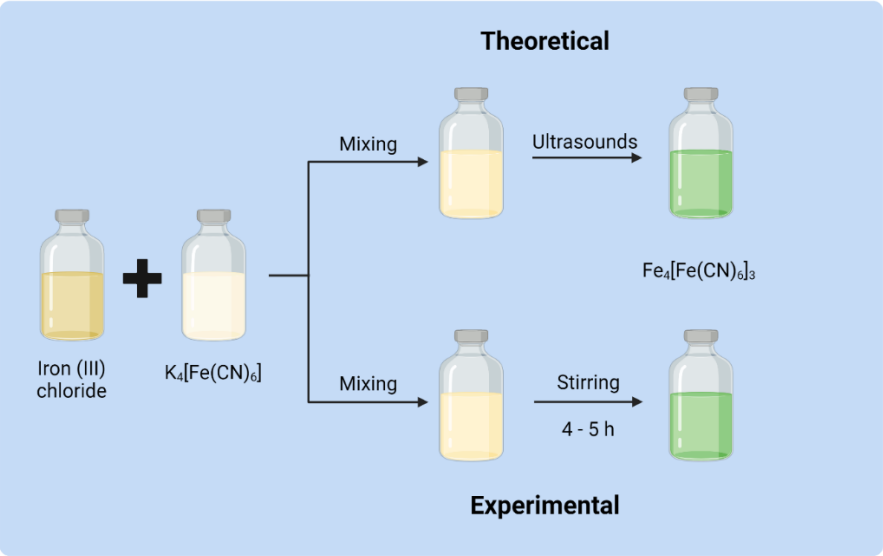

Figure 4.1.4: Schematic representation of the synthesis of Prussian blue within the miniemulsion system and a comparison between the theoretical and experimental outcomes.

In order to test if this was a particular scenario of a specific formulation of the miniemulsion, several trials with different miniemulsion formulations were carried out, varying both the surfactant concentration and the sonication time. Five different concentrations of surfactant were tested, that is 1.5, 2.3, 3.0, 5.0 and 10% wt of the continuous phase. As regards the 1.5% wt, the miniemulsion was not stable for more than three hours, therefore no conclusions could be drawn, since the stability period of 24 h chosen as stability time scale was not fulfilled. Regarding the miniemulsions with 2.3 and 3.0% wt of Span80, the colour change from cream-yellow to green occurred in roughly 4 to 5 h. For the 5.0% wt miniemulsion, the colour change occurred in roughly 1 h, and finally for the 10% wt miniemulsion, the colour change occurred in about 10 minutes. Thus, a shorter time required for the colour change, and therefore a faster material exchange amongst the droplets, could be found with increasing concentration of the surfactant. This could be due to the fact that with increasing surfactant concentration, the formation of free micelles of surfactant begins to occur once its concentration overcome the critical micelle concentration (cmc), favouring the material exchange, since the free micelles can exchange matter. These free micelles can freely exchange matter,[98] and this could explain why with a higher concentration of surfactant, an easier matter exchange, and thus a more rapid colour change, occurred. An accurate determination of the cmc of the specific system was not possible, due to the absence of a surface tensiometer which could provide an accurate estimation of the cmc. However, this experiment could suggest that the matter exchange for the formation of Prussian blue occurs more slowly as compared to the yttrium/metavanadate system, probably due to a difference in diffusion constant of the different ions, also through the surfactant layer. In this case, the only difference with respect to the literature's example was the exploited surfactant, which was Span80 for the experimental trials in this work and [P(E/B)–*b*–PEO] (that is poly(ethylene-butylene)–*b*–poly(ethyleneoxide) copolymer) for the literature's example. The two surfactants' structures are quite different, with the copolymer presenting an apolar part with a higher steric hindrance, which could entail a higher inertia with respect to the matter exchange and thus explain the better stability regarding the inter-droplets matter exchange of

the miniemulsions obtained using the copolymer as surfactant. As regards the different sonication times, four values were tested, that is 1, 2, 5, and 15 minutes. In this case, the only difference amongst these trials was that only the miniemulsion sonicated for 2 minutes was stable for the 24 h chosen as stability period.

However, as discussed in the following chapters, the effect of the confined space on the final size and morphology of the product is still persistent, even with the initial exchange of matter amongst the droplets. This could probably be due to the exchange of ions among the droplets after mixing and before sonicating, but not of solid product, which forms within the confined space of the droplet and cannot penetrate the surfactant layer, thus resulting in an effective space confinement.

4.2 Synthesis via inverse miniemulsions

For the synthesis via inverse miniemulsions of the non-substituted YVO_4, three different synthetic methods were tested, which are a combination of the co-homogenization and the diffusion approaches, and which are described in more detail in section 6.3. Here, the properties of the non-substituted YVO_4 obtained with $Y(NO_3)_3 \cdot 6H_2O$ and NH_4VO_3 as yttrium and vanadium precursors respectively, adjusting the pH of the reaction mixture to 11 and by exploiting the co-homogenization followed by diffusion approach (method A, paragraph 6.3), here labelled as YV-A3, are discussed more in detail and considered as reference for the following paragraph on the variation of the reaction conditions. The reaction process is described in detail in section 6.3.

4.2.1 *Reference sample*

The crystal structure of the reference compound was determined by XRD analysis. For the analysis of the diffractograms, it must be reminded that the position of the reflections in the diffraction pattern depends only on the crystalline phase and crystallinity of the sample, whereas the broadening of the reflections depends on two different factors: the instrumental and the specimen's ones. The former are due to the geometry of the diffractometer and to the optical components, while the latter are due to the crystallites size, the strain of the crystallites or the local distortion of the reticular plane. For example, the diffraction peak broadening is inversely proportional to the crystallites size and directly proportional to the crystallites strain.[99] In this work, the crystallites size is estimated by using the Scherrer's equation (**Equation 6.2**, Paragraph 6.1), but it is important to underline that this is just an approximation, since this equation correlates the diffraction peak broadening only to the crystallites size and not to the other factors. For a more accurate estimation of the crystallites size and unit cell parameters, in order to also consider the other instrumental and specimen's factors influencing the diffraction peaks broadening, Rietveld refinement calculations should be carried out.[100] In the case of YV-A3 sample, since the reflections on the diffractograms were too large to assess the presence of phases other than that of YVO_4, a calcination step (500 °C, 2 h) was carried out. **Figure 4.2.1** reports the diffractograms of the reference sample both before and after calcination. As it can be noted, no phases other than the zircon-

type of the YVO_4 were detectable, thus indicating a high purity of the obtained sample. The analysis of the diffractogram of the as prepared sample confirmed a zircon-type YVO_4 structure, named wakefieldite, (COD 9009764) with space group $\mathbf{I}4_1/amd$ and a D_{4h}^{19} point group symmetry, as described in paragraph 3.1. The crystallites dimension estimated by using the Scherrer's equation were of roughly 5 nm; the crystallinity was estimated by the *diffractEVA* software and is of roughly 60%, and the unit cell parameters were extrapolated with the Vesta software for the Card COD 9009764, and they were equal to $a = b = 7.11830$ Å and $c = 6.28930$ Å and $\alpha = \beta = \gamma = 90°$. In the diffraction pattern, the most intense reflection was that at 25° 2θ, i.e. the (200) Bragg peak, in agreement with the reported examples in literature.[101] The quite low crystallinity of the sample hinted at the absence of a long range order in the structure, also supported by the small crystallite dimensions.

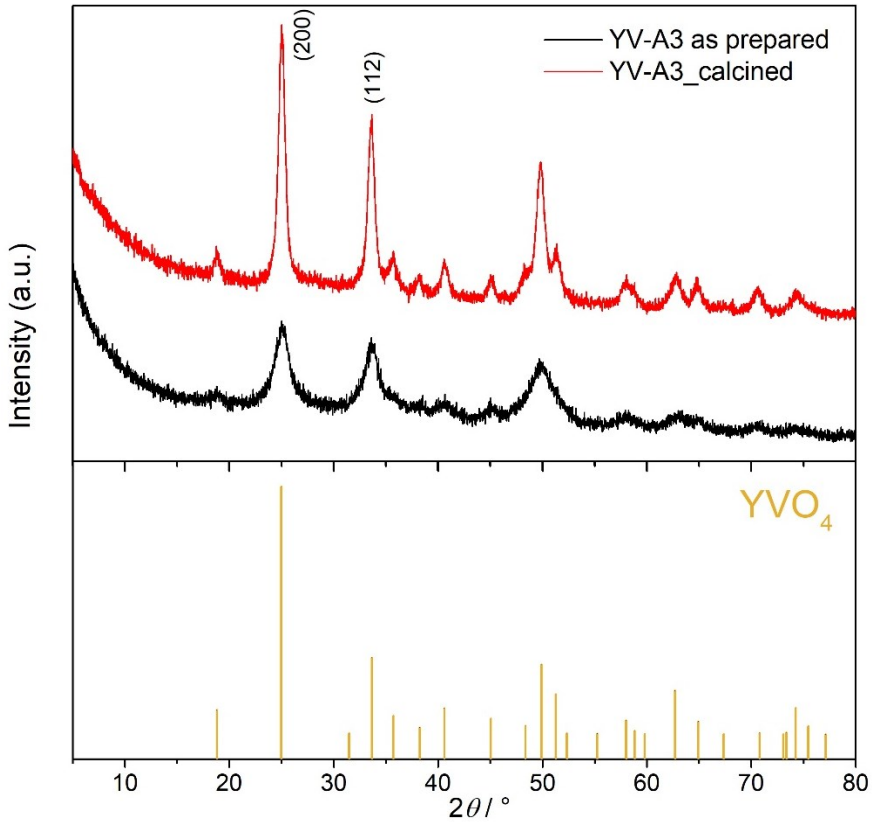

Figure 4.2.1: Diffractograms of the as prepared (black) and calcined (red) reference sample. The diffraction pattern of zircon-type YVO_4 is also reported as a refence, with the (200) and (112) reflections highlighted.

To further confirm the crystalline structure of the YVO_4, Raman spectra were measured in order to investigate the vibrational modes of the crystal. As already discussed in paragraph 3.1, zircon-type yttrium vanadate presents YO_8 dodecahedra and VO_4 tetrahedra which shares edges with each other, and it should present twelve phonons which are Raman-active. The Raman-active vibrations can be classified into internal and external modes. The first arise from the VO_4^{3-} orthovanadate ion vibrations, thus with the mass centre being fixed in the initial position, whereas the second arise from translations and rotations of the VO_4 tetrahedra considered as a whole with respect to the yttrium ion. Typically, the

internal modes involve vibrations of the strong V-O covalent bond, while external modes rely on the weak coupling between the VO_4^{3-} molecular ion and the Y^{3+} ion. Thus, the internal modes are generally associated with more energetic transitions, generating Raman signals at higher wavenumber compared to the signals arising from the external modes. The Raman spectrum of YVO_4 could therefore be divided into two regions, one presenting the internal modes of the orthovanadate molecular ion (ranging from 891 to 264 cm^{-1}), and a second one presenting the external modes (ranging from 264 to 160 cm^{-1}). Figure 4.2.2 reports the Raman spectrum measured for the reference sample, and Table 4.2.1 summarises the assignation of the peaks to the corresponding vibrational modes. From group theory calculations, the YVO_4 molecule possesses thirty-six vibrational modes: $\Gamma_{36} = 2A_{1g} + 2B_{1u} + B_{1g} + A_{1u} + A_{2g} + B_{2u} + 4B_{2g} + 4A_{2u} + 5E_g + 5E_u$, but only twelve even parity phonons are Raman active. In the measured Raman spectrum of the reference sample, only nine of the twelve active vibrational modes were detectable, in good agreement with the results of *Miller et al.*[64]

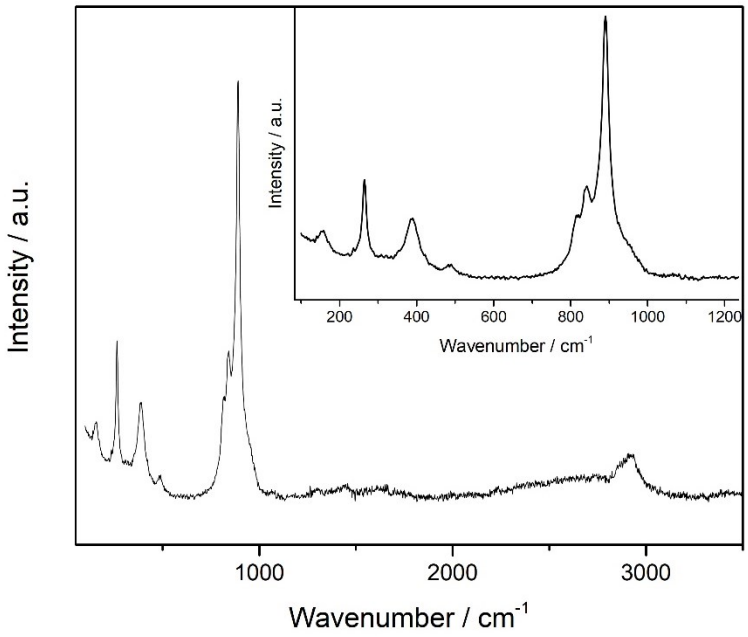

Figure 4.2.2: Raman spectrum of the reference sample.

Table 4.2.1: Assignation of the Raman signals of the reference sample.

Wavenumber (cm^{-1})	Mode	Reference[64] (wavenumber, cm^{-1})
160*	B_{2g}	157
160*	E_g	162
264**	B_{1g}, E_g	260
384	A_{1g}	379
487	B_{2g}	489
814	B_{2g}	817

841	E_g	840
891	A_{1g}	891

*: in the measured spectrum, they result superimposed

**: degenerate

All the vibrational modes associated with the peaks from 384 to 891 cm^{-1} wavenumber and the B_{1g} mode at 264 cm^{-1} involve internal vibrations of the orthovanadate ion, while the E_g mode at 264 cm^{-1} is associated with an external rotational mode, and finally the two signal at 160 cm^{-1} are associated with external translational modes. Finally, at roughly 2900 cm^{-1}, the signal arising from adsorbed water and residual surfactant can be detected, due to the stretching of O-H and C-H bonds.[102]

Finally, in order to evaluate the particles' size and morphology, SEM measurements were carried out on the sample. From SEM images it was not possible to accurately determine the size of the particles, because of their small dimensions. However, it was possible to roughly estimate their size, and since they presented a spherical shape, the estimation of the dimensions was independent of the chosen direction of measure. As can be noted from **Figure 4.2.3**, the particles possessed a diameter of roughly 30 to 40 nm, and they tended to aggregate into bigger particles, of a non-defined shape. These aggregates could reach dimensions up to 1 µm. TEM measurements were carried out in order to better assess the particle size and size distribution. **Figure 4.2.4** highlights how the particles seemed to possess sharp edges of an undefined shape rather than a clear spherical shape. Using the ImageJ software, a particle size of (27 ± 6) nm was estimated. The non defined shape and quite large standard deviation from the mean particle size may hint to a not complete reaction and therefore the not complete formation of a well-defined product. Trials with a longer reaction time would be required in order to assess if this hypothesis could be well-founded. A possible alternative explanation could be that, when performing the reaction in the miniemulsion system, the confined space may alter the Ostwald's step rule mechanism, for example by stabilising a possible intermediate state previous to the thermodynamically stable one, which is obtained by batch synthesis.

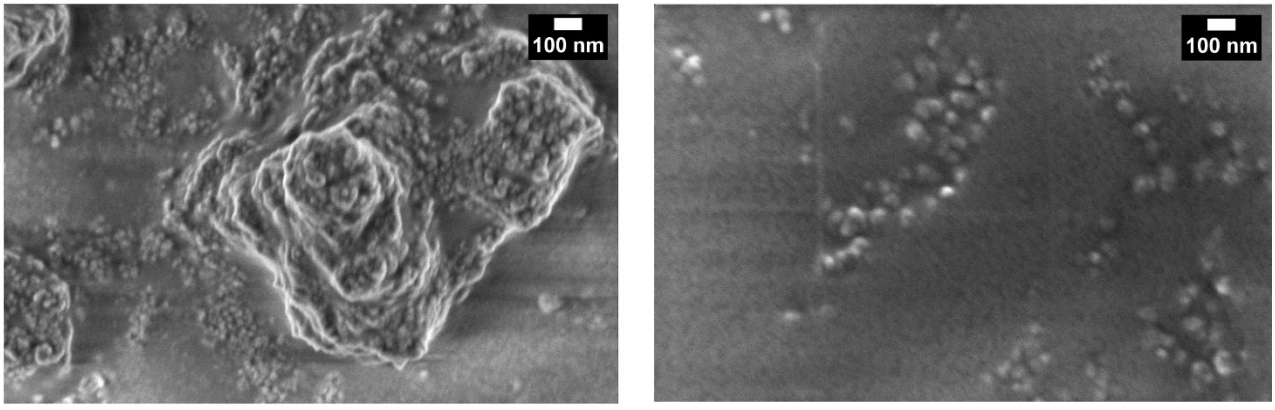

Figure 4.2.3: SEM images of the reference sample.

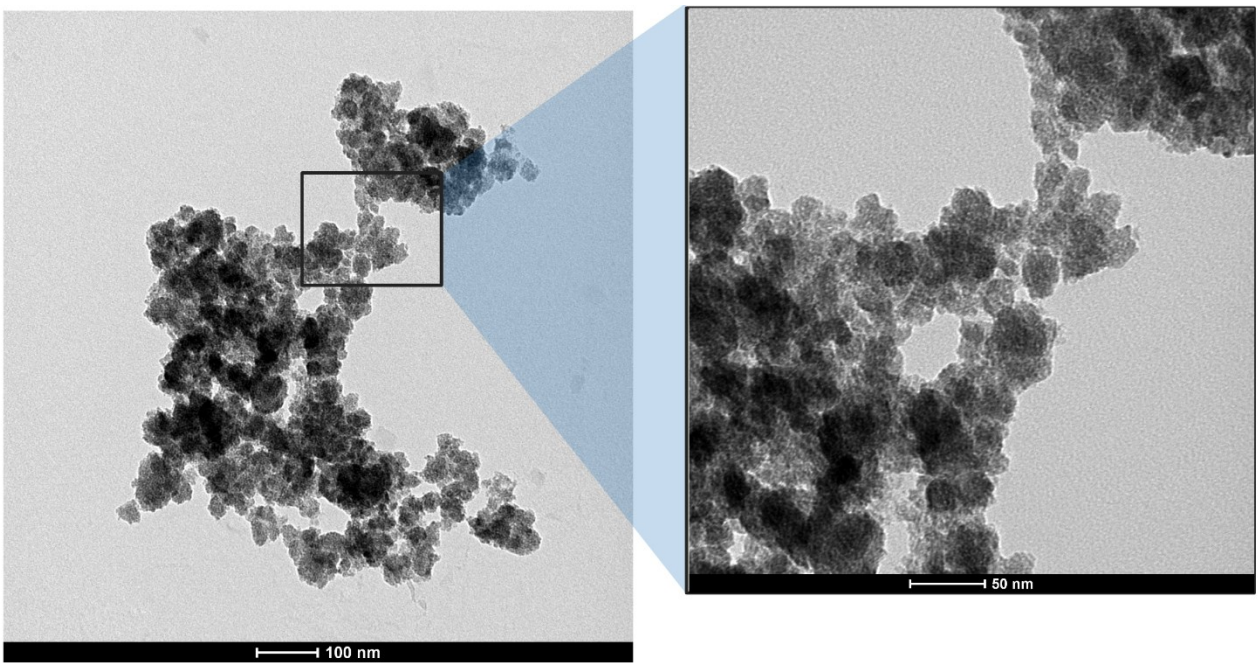

Figure 4.2.4: TEM image of the reference sample.

On the suspension of the product particles, DLS measurements were carried out in order to assess the hydrodynamic radius of the particles. The measurements were performed after sonication of the product powder suspended in water with the tip sonicator (3 mm of diameter), and at 10% of the maximum amplitude (550 W) for 5 minutes. As can be noted in Figure 4.2.5, the particles appeared to possess a hydrodynamic radius of (330 ± 10) nm. However, this value overestimated the size of the spherical particles obtained through the SEM images, and this is probably due to the fact that the aggregates did not separate into the single particles after sonication, therefore DLS measurements revealed the hydrodynamic radius of the aggregates themselves. Besides, the aggregates hydrodynamic radius was also larger than the hydrodynamic radius of the droplets in the miniemulsion (Figure 4.1.1), thus further confirming the fact that the signal arises from the aggregates and not from the single particles. The fact that the aggregates result larger than the miniemulsion's droplets could be explained by an aggregation of the product particles outside of the droplets themselves, thus during the purification step (paragraph 6.3), or during the preparation of the sample for the DLS measurement.

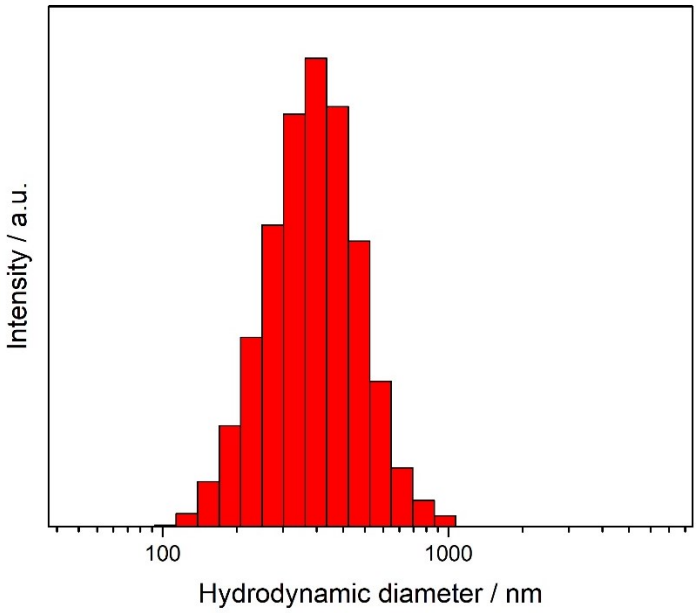

Figure 4.2.5: DLS measurement of the reference sample product particles.

In order to assess the presence of residual surfactant on the product, TGA-DTA analysis, coupled with MS analysis, was performed as reported in Figure 4.2.6. The TGA analysis up to 1000 °C was conducted in a synthetic air atmosphere, in order to reveal the residual surfactant present in the sample, since it releases CO_2 in an oxidative atmosphere.

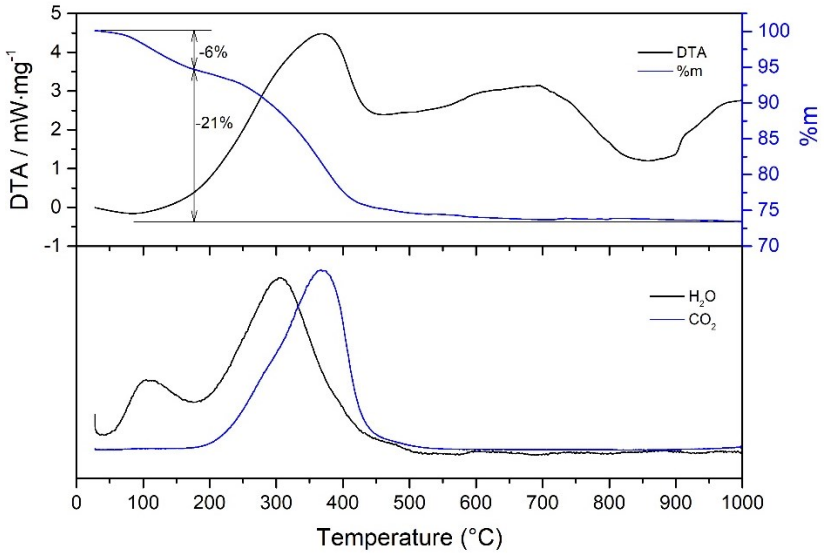

Figure 4.2.6: TGA-DTA coupled with MS analysis of the reference sample.

As can be noted, an initial weight loss of 6% with respect to the starting weight due to water evaporation could be detected at 100 °C. Then a weight loss of 21% of the initial weight was detected in the range

from 200 to 400 °C. This loss was related to a second evaporation of water, as it can be observed from the H_2O signal in the MS graph, probably due either to water molecules adsorbed not on the surface of the aggregates but on the defects of the structure or to water molecules bonded through H-bonds to the surface of yttrium vanadate particles, thus requiring a higher temperature to evaporate. This weight loss could be also due to the degradation of possible residual $Y(OH)_3$ to Y_2O_3 with evaporation of water. However, as can be noted in **Figure 4.2.8**, no signal of Y_2O_3 could be detected after the thermal treatment, thus excluding the degradation of the possible residual hydroxide. The weight loss related to the CO_2 formation arose from the degradation of the residual surfactant. Another interesting phenomenon that can be noted from the TGA-DTA measurement is an exothermic process occurring at 900 °C with no weight loss associated, as can be noted in **Figure 4.2.6**. Therefore, this could arise from a phase change in the crystalline structure. To confirm this hypothesis, *in-situ* XRD measurements of the powder at different temperatures were carried out (**Figure 4.2.7**), as well as an XRD measurement on the reference sample after TGA treatment (**Figure 4.2.8**).

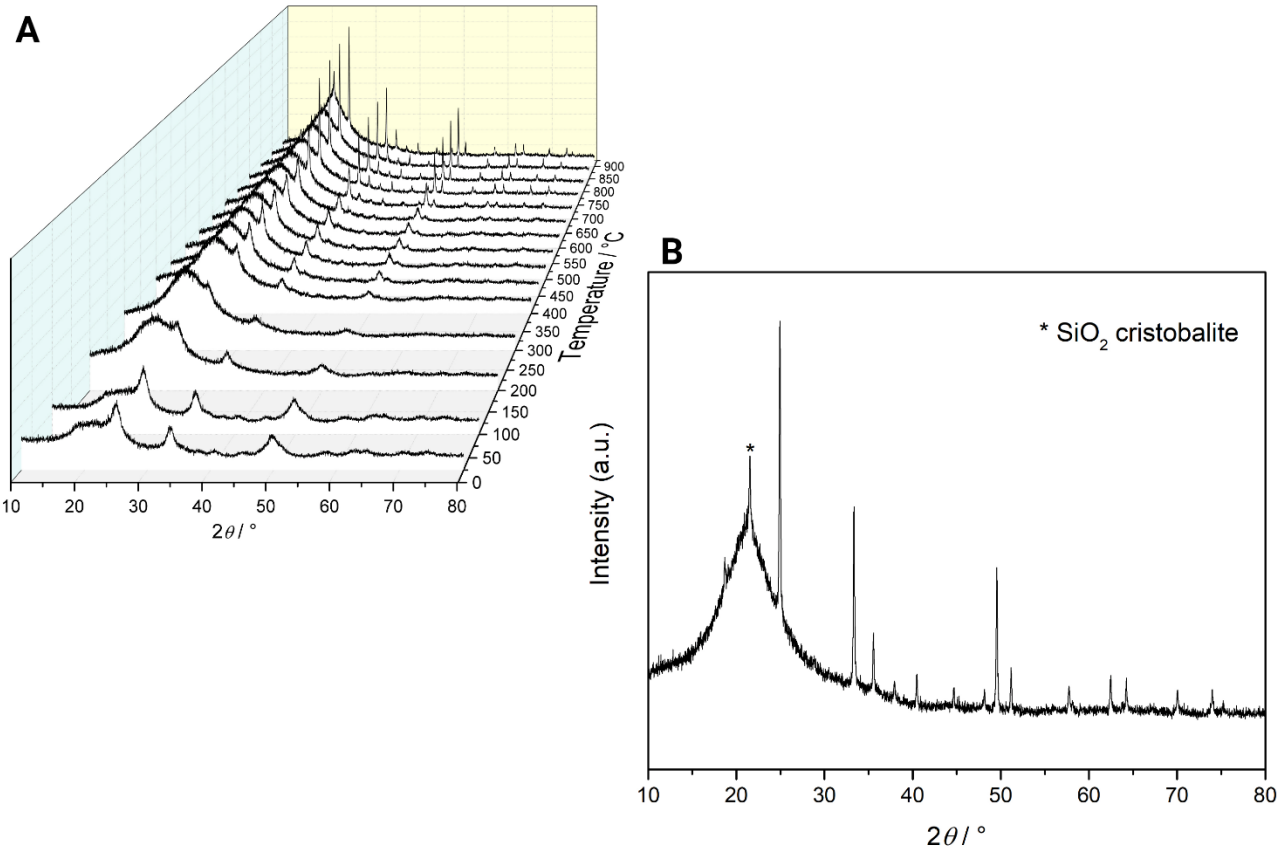

Figure 4.2.7: XRD measurements at different temperatures (A) and the XRD measurement after thermal treatment at 900 °C (B) of the reference sample.

In the *in-situ* measurements, the initial broad reflection, centred at 20.3° 2θ, was caused by the quartz capillary used for the measurement. From **Figure 4.2.7A**, it is possible to distinguish an initial decrease of the intensity of the reflections at temperatures up to 300 °C. Probably, this was due to the fact that the sample was placed in a capillary, and the evaporation of both water and carbon dioxide may have led to a displacement of the sample (noted by the presence of blank spaces in the capillary at the end of

the measurement), which caused an apparent lowering of the intensity of the reflections, when actually it was simply an effect caused by the evaporation of gases that altered the distribution of the powder in the capillary. At 900 °C no additional reflections could be noted, other than a reflection at 22° 2θ that may be attributed to an initial formation of SiO_2 cristobalite structure from the quartz of the capillary (Figure 4.2.7B). The cristobalite starts forming at roughly 1000 °C, and this could explain the signal. However, from the diffractogram reported in Figure 4.2.8, measured on the sample after the TGA measurement, it was possible to distinguish a signal at 29° 2θ, assigned to the yttrium and vanadium mixed oxide $Y_8V_2O_{17}$ (PDF 44-0390), which was probably the phase started forming at around 900 °C. However, this phase was not detectable by *in-situ* measurements due to the overlapping of the broad reflection of the quartz capillary and also because, due to technical limitations, the maximum temperature reached with the *in-situ* XRD measurement was 900 °C and not 1000 °C as for the TGA measurement.

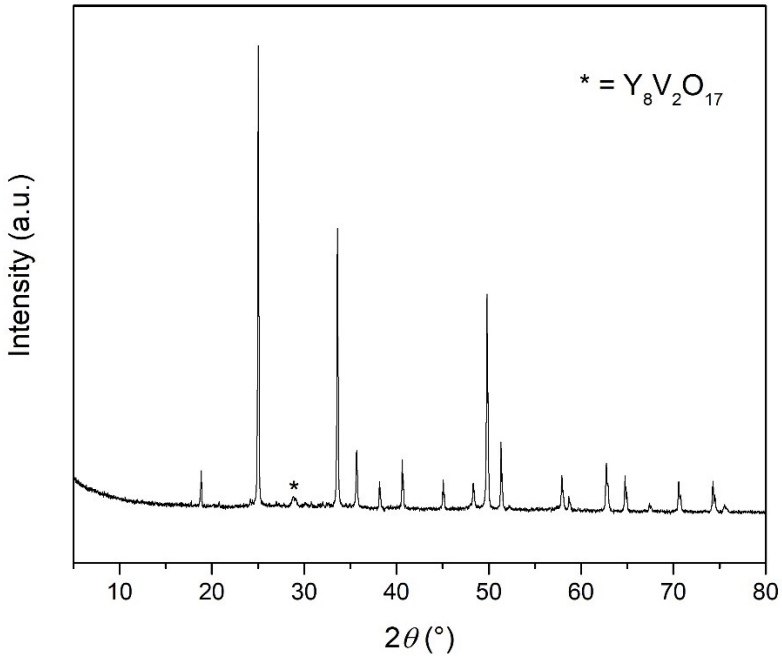

Figure 4.2.8: XRD measurement of the reference sample after the TGA treatment.

4.2.2 Variation of the reaction conditions

In this section, the variation of the reaction conditions and the resulting effect on the particles size and morphology, as well as possible variation on the optical band gap and Raman spectrum are discussed. From an experimental point of view, the reaction conditions were varied one at a time (the *one variable at a time* (OVAT) approach) in order to assess the specific effect on the product features. The varied conditions are: *i*) the exploited method for the reaction steps (a thorough description of the different methods is reported in paragraph 6.3), *ii*) the starting vanadium precursor, changed between Na_3VO_4 and NH_4VO_3, *iii*) the pH of the aqueous phase of the reaction mixture, that is after the mixing of all the

reagents, varied amongst 4 (autogenic pH), 7, 9 and 11 by addition of sodium hydroxide. It must be specified that the reason for the variation of the sole vanadium precursor species, and not also of the yttrium one, arises from previous observations for the batch reaction, in which it was found that the nature of the yttrium precursor does not significantly affect the product properties. Moreover, since the evaluation of the pH value of the aqueous phase is hindered by the presence of the organic phase, the previous batch synthesis were taken as reference also in this case: the molar ratios amongst yttrium, vanadium and sodium hydroxide were kept constant and equal to those exploited in the batch synthesis, thus assuming that the resulting pH would also be comparable. In general, by varying these reaction parameters, it can be observed that the morphology of the nanoparticles is maintained as spherical, with almost constant size ranging from 30 to 50 nm, accounting for an effective space confinement in the miniemulsion droplets.

Variation of the vanadium precursor. The reactions for the synthesis of yttrium vanadate in miniemulsion were mainly carried out exploiting the ammonium metavanadate (NH_4VO_3) as vanadium precursor, since it was found to be the most sensitive to the variation of the reaction conditions, when considering as a reference the batch synthesis carried out in a previous work. However, in order to check if this difference between the two vanadium educts is found also in the miniemulsion system, some reactions were completed using the sodium orthovanadate (Na_3VO_4) as vanadium precursor. As regards the morphology, both precursors led to spherical nanoparticles of roughly 40 nm of diameter estimated by SEM images, using the ImageJ software for the dimensional analysis (Figure 4.2.9), aggregated into bigger particles of a non-defined shape. The fact that both precursors led to spherical nanoparticles with a comparable size, implies that the synthetic method, that is synthesis in miniemulsion, significantly affects the morphology and particles size of the product, even more significantly than the reaction parameters exploited.

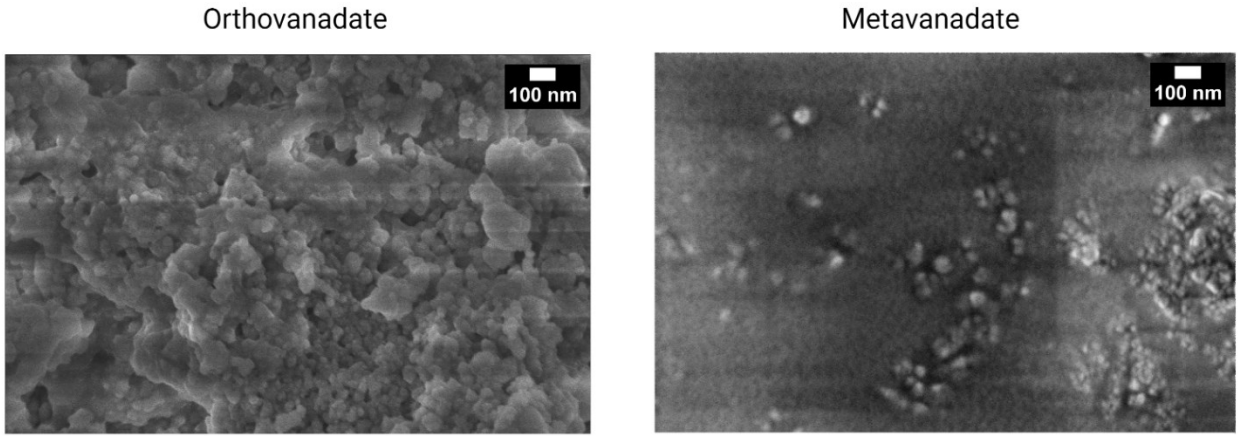

Figure 4.2.9: SEM images YVO_4 particles obtained exploiting either Na_3VO_4 as educt (left) or NH_4VO_3 (right), pH = 11. The yttrium vanadate particles on the right were synthesised exploiting the synthetic method A.

The main difference between the two different educts is found when the reaction is carried out at autogenic pH (pH 4): by exploiting the orthovanadate as educt, the diffraction pattern of the zircon-type yttrium vanadate is detectable, while using the metavanadate as vanadium reagent, additional reflections resulting from the presence of polyoxovanadate species, most probably decavanadate ($V_{10}O_{28}^{6-}$) since it is the most stable at pH 4 (cfr. Figure 3.1.3), are detectable (Figure 4.2.10). This may be explained by the different reaction mechanisms occurring with the two vanadate precursors. With the orthovanadate as precursor, the initial amorphous $Y(OH)_3$ reacts directly with the orthovanadate ions to yield the final crystalline yttrium vanadate. On the other hand, when using the metavanadate as precursor, the metavanadate ion must react with a hydroxide ion to convert to the orthovanadate molecular ion before reacting with the yttrium hydroxide to yield the final product.[80] Thus, at low pH value, the lack of hydroxide groups in the reaction solution may explain the presence of polyoxovanadate species and the partial formation of the yttrium vanadate product. The presence of vanadium species other than yttrium vanadate is further confirmed by the calcination of the sample (Appendix A.1, Figure 9.1.1): after calcination at 500 °C for 2 h, the presence of vanadium pentoxide (V_2O_5, PDF 09-0387), derived from the degradation of vanadium species, can be detected from XRD measurements.

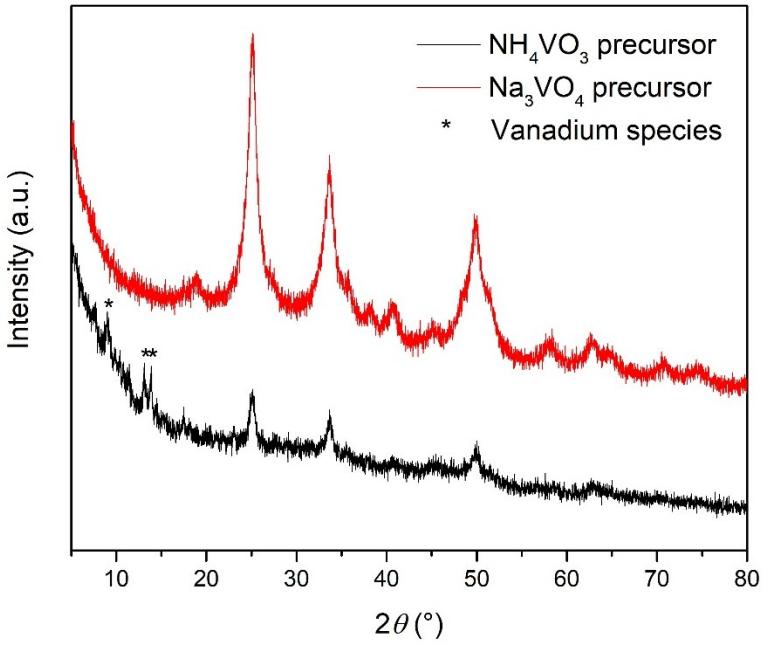

Figure 4.2.10: XRD measurements for yttrium vanadate obtained at pH 4 with either ammonium metavanadate or sodium orthovanadate as vanadium educts.

Variation of the pH of the aqueous solution. The pH was varied by adding the sodium hydroxide, whether to the yttrium miniemulsion or to the reaction mixture by diffusion, depending on the exploited synthetic method (paragraph 6.3). The four pH values were 4, 7, 9 and 11. As can be noted by Figure 4.2.11, apart from the diffractogram of the product obtained at pH 4 exploiting the metavanadate as vanadium precursor already discussed, it can be noted that different concentrations of sodium hydroxide do not result in a significant variation of the product's crystallinity and crystallites size, being roughly 60% and 6 nm respectively. However, an estimation with the Rietveld refinement would be needed to precisely calculate the crystallinity and crystallites size of the different products, in order to assess if the small

variations found with the Scherrer's equation must be attributed to the method or to actual differences in the products properties.

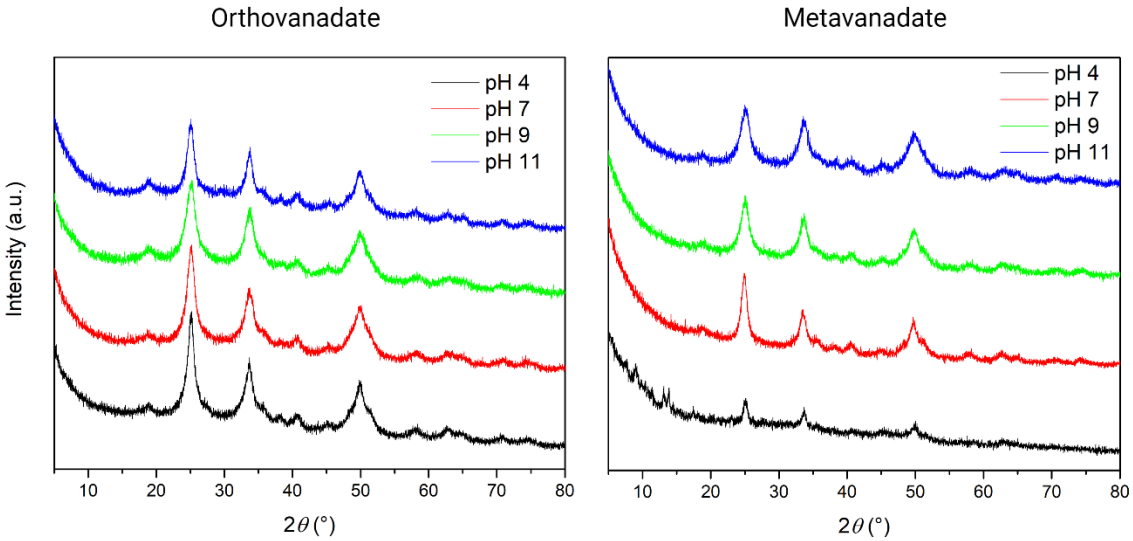

Figure 4.2.11: XRD diffractograms of the yttrium vanadate products obtained at different pH values of the aqueous phase. The exploited vanadium precursor is Na_3VO_4 (left) and NH_4VO_3 (right).

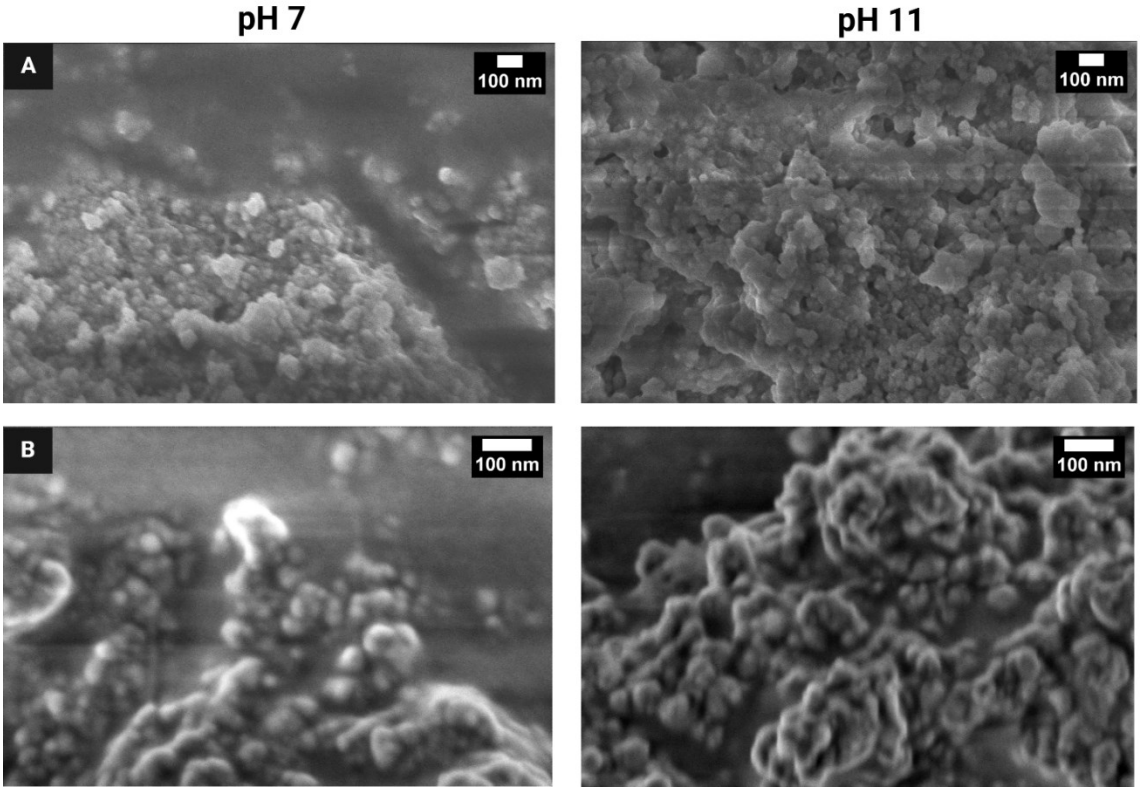

Figure 4.2.12: SEM images of the yttrium vanadate particles obtained at two different pH values exploiting Na_3VO_4 (A) or NH_4VO_3 (B) as vanadium educts. The particles in (B) were synthesised exploiting the synthetic method B.

Also, Figure 4.2.12 highlights that no significant differences are found in the product morphology and particles size with different concentrations of NaOH added in the reaction mixture. The particles retain

their spherical shape with a diameter of roughly 40 nm. In order to better assess the particle morphology and dimensions, TEM measurements were acquired on selected samples. To check the dependence on the pH, two samples obtained exploiting the synthetic method A at two different pH values were measured with the TEM. As can be noted by Figure 4.2.13, the sample obtained at pH 7 seems to be highly irregular both in shape and size of the particles and highly aggregated, to the point that it was not possible to assess a mean diameter of the particles. On the other hand, as regards the yttrium vanadate obtained at pH 11, the particles are still not of a well-defined form: indeed, they seem to present sharp edges instead of a spherical shape as predicted by SEM images. However, it is possible to distinguish the particles borders and therefore estimate the particles size. By using the ImageJ software, a particles size of (27 ± 6) nm was found, slightly underestimating the value outlined by the SEM images. This visible dependence of the particles shape and size on the pH of the reaction environment is a further confirmation of the reaction mechanism, which involves the hydroxide ions as reactive species. However, the irregular shape and the quite large standard deviation compared to the mean particle size could be a hint of an uncompleted reaction, suggesting that a longer reaction time may be needed when carrying out the reaction in the miniemulsion system.

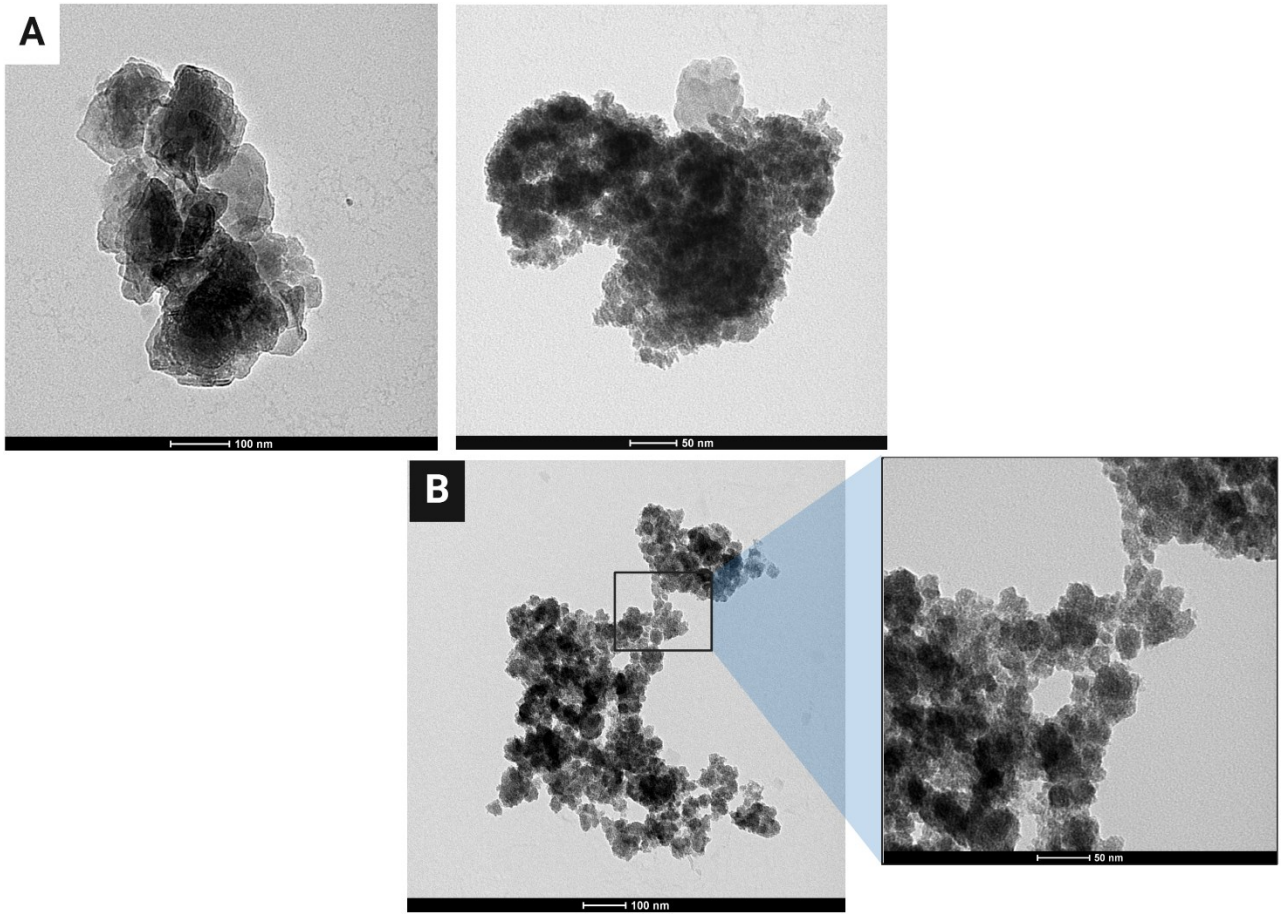

Figure 4.2.13: TEM images of two different yttrium vanadate samples obtained exploiting the synthetic method A. The experimental pH values are 7 (A) and 11 (B).

As regards the optical band gap and absorption spectra, Figure 4.2.14 illustrates how the product obtained at pH 4 presents quite different properties as compared to the others, which instead are similar.

The product obtained at pH 4 is also visibly different as compared to the others, presenting a dark-brown colour instead of a light yellow one. This is confirmed by the different absorption spectrum, where a weak absorption up to 500 nm is detectable, causing the yellow colour of the powder. As regards the optical band gap, the lower value obtained for this product may be explained by the presence of polyoxovanadates species, which possess lower band gap energies compared to the yttrium orthovanadate compound.[103] This further confirms the hypothesis of the reaction mechanism. However, the higher magnitude of the band gap compared with the value reported in the literature (roughly 3.3 eV for particles and 2.8 eV for the bulk material)[104–106] may be either due to the larger amount of defects of the synthesised products or to the quantum confinement effect, which is responsible for a larger band gap in nanosized semiconductors of dimensions up to a few tens of nanometers, as compared to the bulk ones.[107,108]

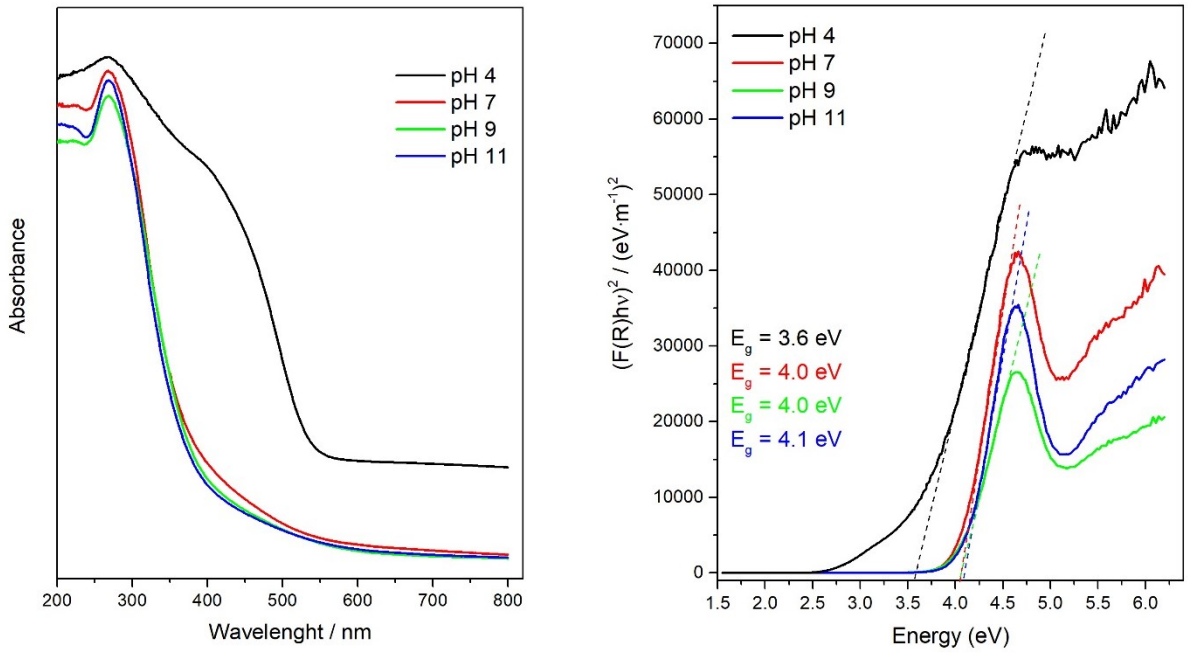

Figure 4.2.14: Absorption spectra (right) and Tauc plot (left) of the yttrium vanadate samples obtained at different pH values. The synthetic method B was exploited for these samples.

A further confirmation of the difference of the yttrium vanadate product obtained at pH 4 compared to the others can be noted in the Raman spectra (the spectrum of the sample obtained at pH 11 was not measured because of the low amount of sample). Figure 4.2.15 highlights the presence of the yttrium vanadate compound in the two samples obtained at pH 7 and 9, while only a partial presence of the typical vibrational bands for the compound obtained at pH 4 (cfr. Paragraph 4.2.1). For this last sample, several further signals can be detectable, and may be attributed to the presence of polyoxovanadate species, but an exact literature comparison was not found. To correctly determine which vanadium species are present in the sample, ^{51}V-NMR measurements should be carried out.

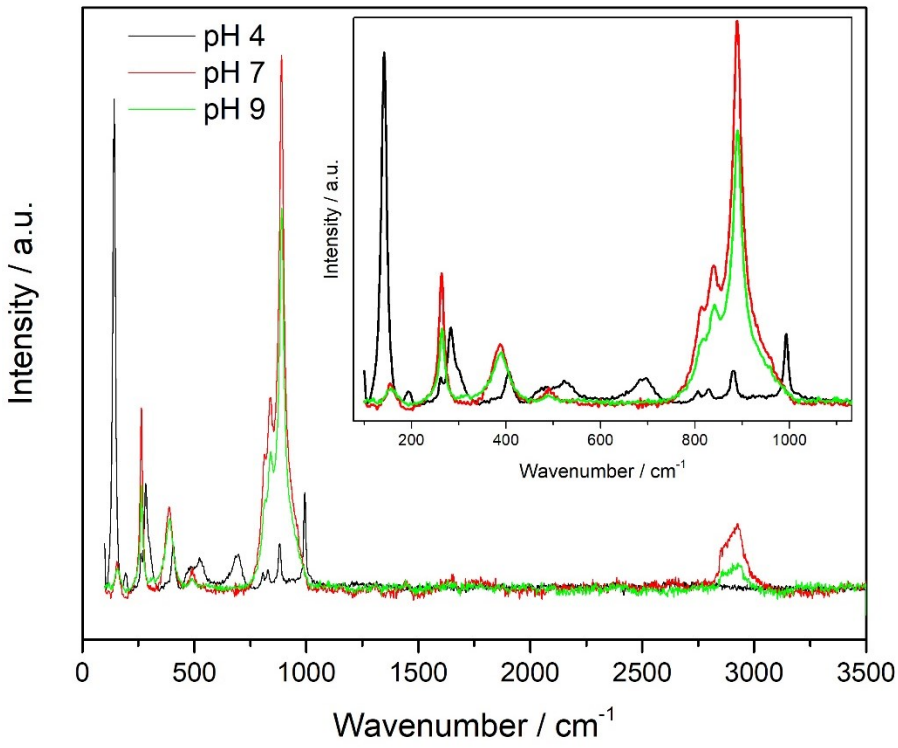

Figure 4.2.15: Raman spectra of the yttrium vanadate samples obtained with the synthetic method B at different pH values. The sample obtained at pH 11 was not enough to register a significant signal.

Variation of the synthetic method. The three different exploited synthetic methods are described in detail in paragraph 6.3. The difference amongst them is the order and method of mixing of the reagents. In method A (co-homogenisation + diffusion), the mixing of the two reagents occurs before the addition by diffusion of sodium hydroxide. In method B (incorporation + co-homogenisation), the sodium hydroxide is added to the yttrium nitrate miniemulsion by sonication, thus causing the precipitation of the $Y(OH)_3$ inside the droplets, which then is mixed and sonicated with the miniemulsion of the vanadium precursor. Finally, in method C the two miniemulsions of the precursors and the sodium hydroxide solution are sonicated together at the same time. Every method was tested at the different pH values, apart from the test at pH 4 which was the same for all the methods. As it can be noted in Figure 4.2.16, also in the case of different synthetic methods and at different pH values, the crystallinity and crystallite size of the product do not vary significantly, being roughly 60% and 6 nm respectively, comparable to the values previously found.

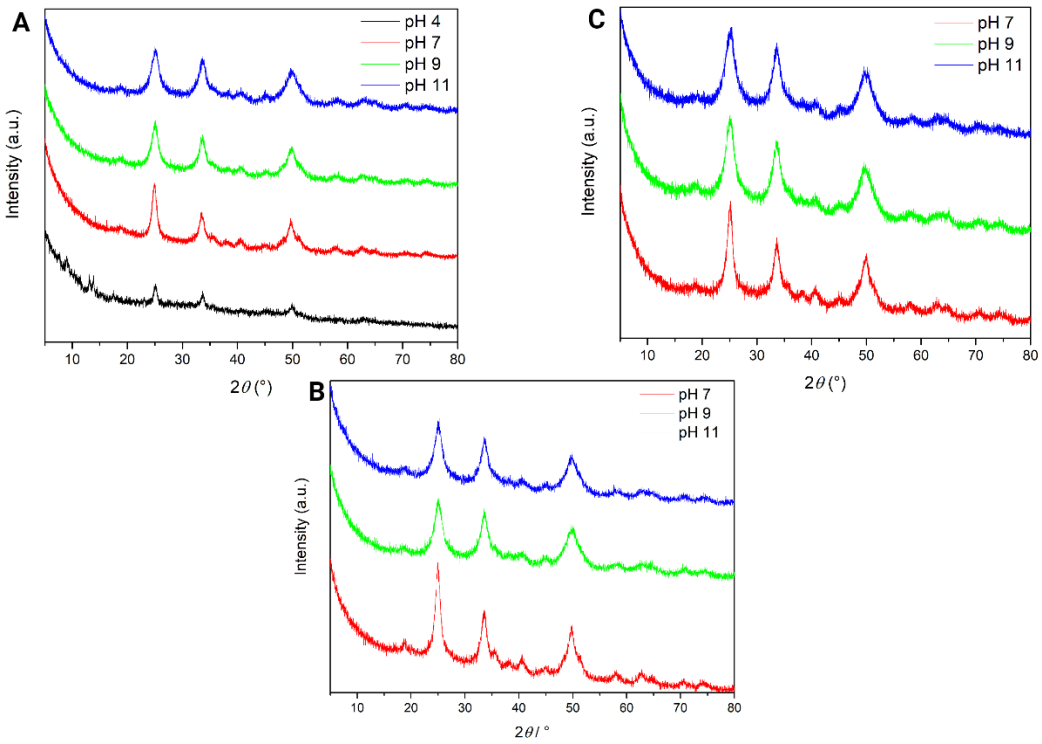

Figure 4.2.16: XRD diffractograms of the yttrium vanadate particles obtained with the synthetic methods A, B and C and at different pH values. The diffractogram of the product obtained at pH 4 is reported only once.

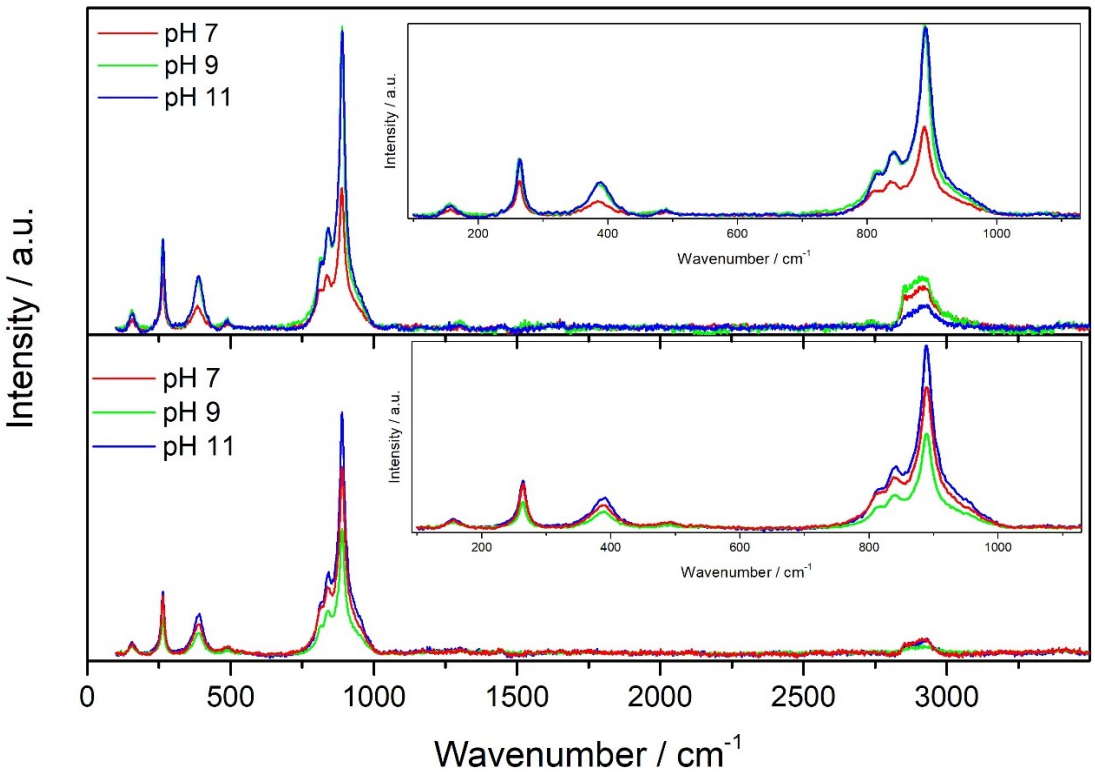

Figure 4.2.17: Raman spectra of the yttrium vanadate samples obtained at different pH values, exploiting the synthetic method A (top) and C (bottom).

As a further confirmation that a different pH value does not involve significant differences from a structural point of view, the Raman spectra of the yttrium vanadate samples obtained at different pH values and with different synthetic methods are reported in Figure 4.2.17, highlighting the absence of significant differences amongst the samples. The Raman spectra of the yttrium vanadate samples obtained with the synthetic method B have already been reported in Figure 4.2.15.

Also in this case, referring to Figure 4.2.3 and Figure 4.2.12, it can be noted that the shape and size of the obtained particles do not vary with different exploited synthetic methods: in all cases, the particles resulted of a spherical shape, and with size of around 40 nm. Moreover, TEM images of two different samples synthesised with two different synthetic methods at pH 7 are reported in Figure 4.2.18. As can be noted, the morphology of the two samples is very different, with the sample obtained through method B presenting a morphology and size distribution more similar to that of the reference sample (Figure 4.2.4). Using the ImageJ software, a particles size of (24 ± 4) nm was estimated. Also in this case, the quite irregular shape and high degree of aggregation of the particles hindered the process of measuring the particles size.

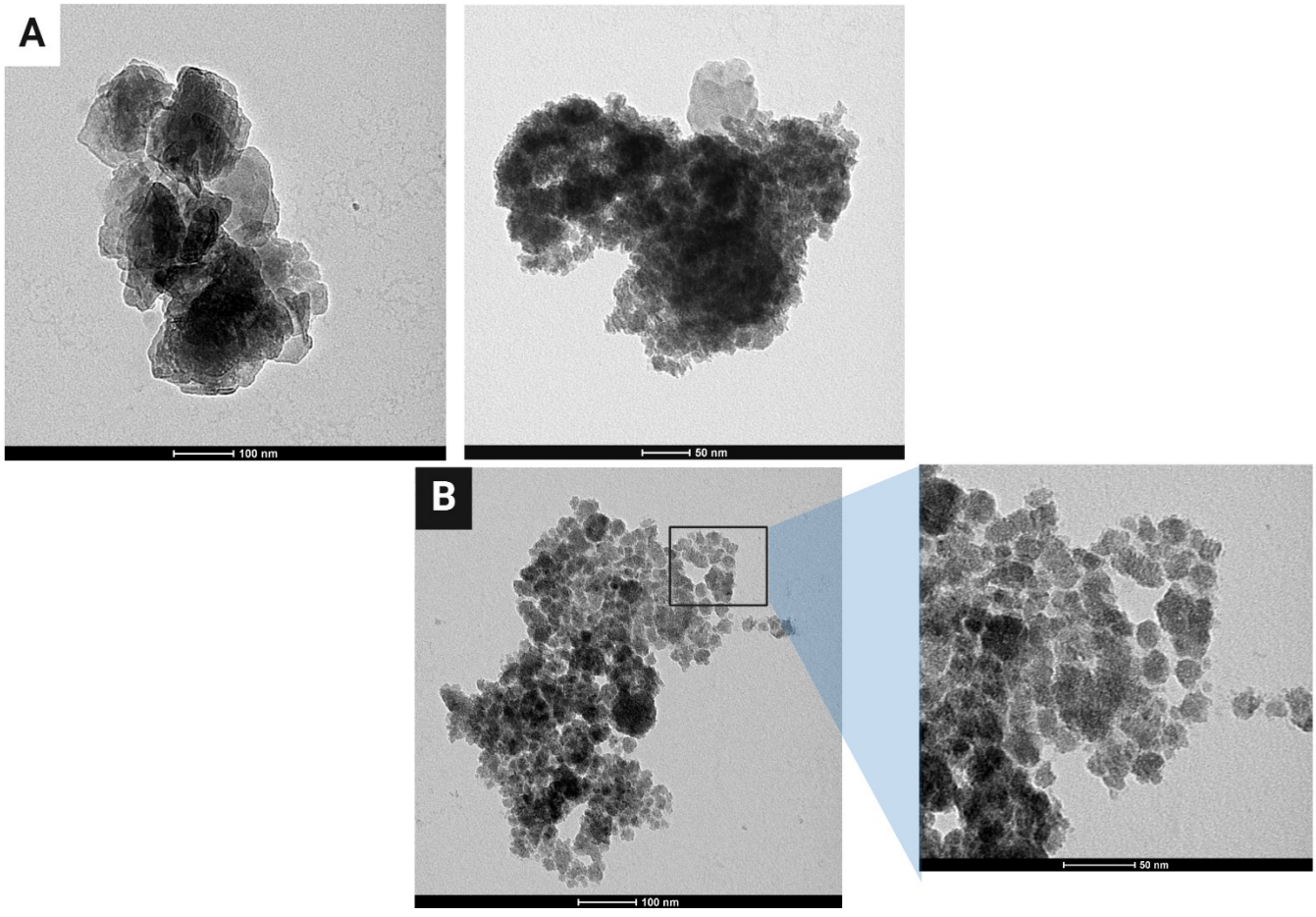

Figure 4.2.18: TEM images of the yttrium vanadate samples obtained exploiting the synthetic method A and B at pH 7.

Finally, as regards the optical band gap, no major differences can be noted with the different exploited synthetic methods (**Figure 4.2.19**). The extrapolated values are comparable with those reported in **Figure 4.2.14**, since a difference of 0.1 or 0.2 eV may arise from a small difference in the plotting of the fit, thus not being to be interpreted among the samples. However, the estimated values are still larger than the reported band-gap value of yttrium vanadate in the literature. The absorption spectra are similar to each other, and to those reported in **Figure 4.2.14**.

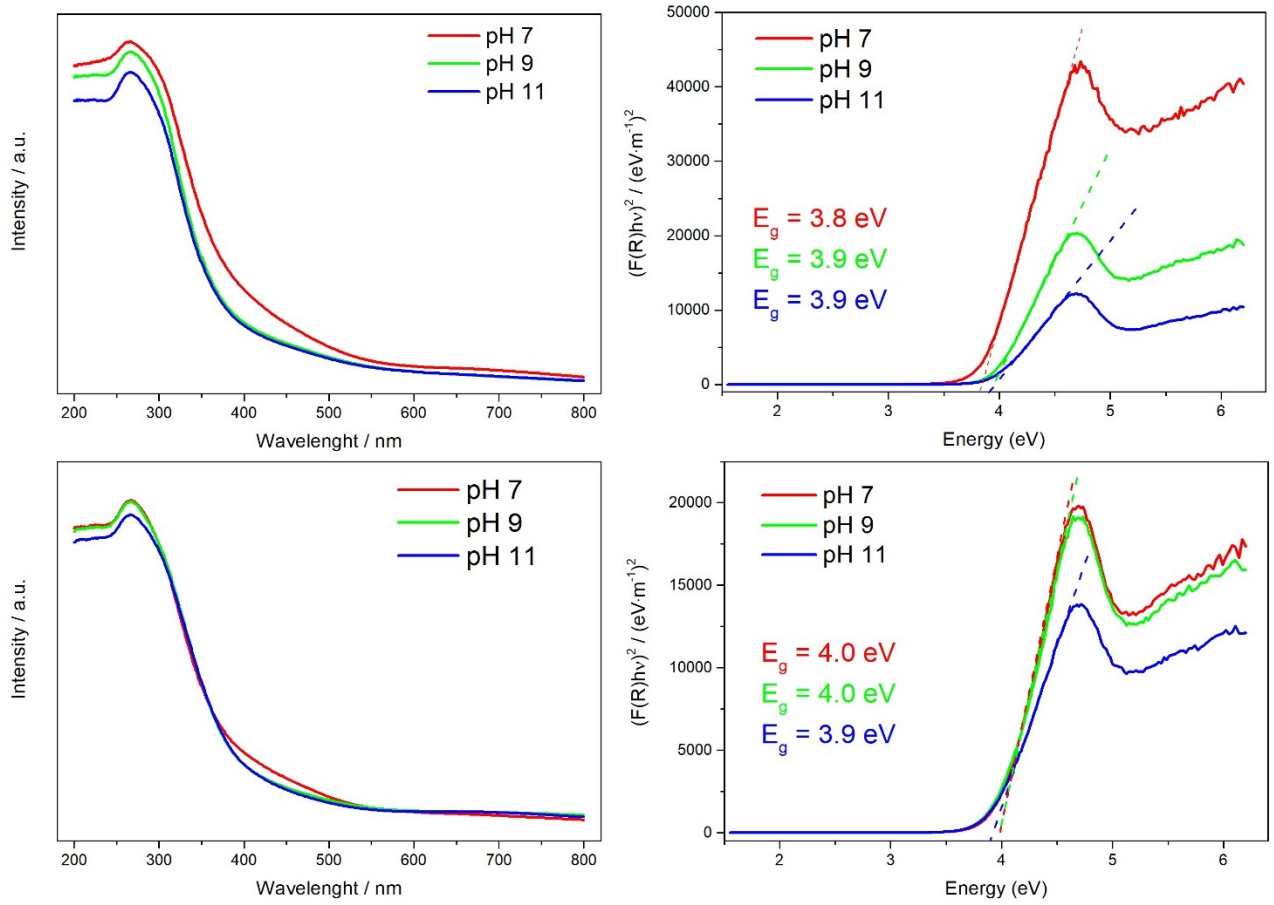

Figure 4.2.19: Absorbance spectra (left) and respective Tauc plot (right) for the yttrium vanadate samples obtained at different pH values, exploiting the synthetic method A (top) and C (bottom).

4.3 Statistic replacement of yttrium vanadate via miniemulsion approach

4.3.1 Structural properties of the samples

The samples were synthesised at different Eu content levels and with different reaction parameters as delineated in paragraph 6.4. The substituted samples resulted in a beige powder as for the non-substituted samples synthesised via the miniemulsion approach. The Eu content was experimentally determined through the EDX technique on selected samples, but a more precise determination of the Eu ions concentration, such as through the ICP-MS analysis, would be required. However, the Eu content

estimated with the EDX analysis is in good agreement with the theoretical one, as highlighted in Table 4.3.1. The list of the different samples can be found in paragraph 6.3.

Table 4.3.1: Europium content, theoretical and experimental (determined through EDX analysis), of the substituted samples.

Sample	Eu content	
	% at. theoretical	% at. experimental
YV-E2	5.0	5.1
YV-E3	10.0	9.5
YV-E4	1.0	1.0
YV-E5	5.0	5.5
YV-E6	10.0	10.5

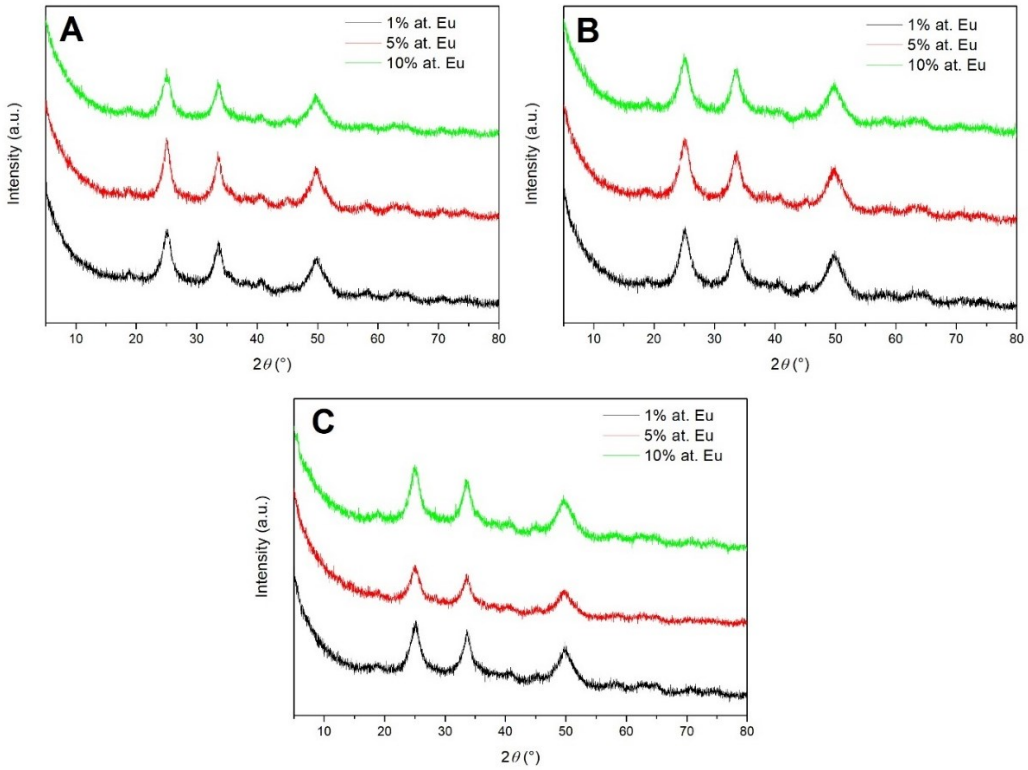

Figure 4.3.1: XRD measurements of the substituted sample. The reaction conditions are: method A, pH 9 (A), method B, pH9 (B), and method A, pH 11 (C).

As regards the crystalline structure, the diffraction patterns of all the different samples (Figure 4.3.1) can be indexed as the tetragonal zircon-type YVO_4, with space group $\mathbf{I}4_1/amd$ and point-group symmetry D_{4h}^{19} thus accounting for a successful insertion of the Eu(III) ions into the crystal structure of the yttrium vanadate samples. Moreover, this means that the substitution of the Y(III) ions with Eu(III) ions does not involve a variation in the crystalline phase, as it can be noted in Figure 4.3.1. However, a calcination step would be required in order to increase the crystallites size, thus making the reflections narrower and allowing a proper determination of the presence of possible phases other than that of the zircon-type

YVO_4. From the XRD measurements reported in **Figure 4.3.1**, it can be stated that no significant differences arise from a different Eu content, with the crystallinity and crystallites size being of roughly 60% and 6 nm respectively, comparable to the non-substituted samples. However, also in this case, a Rietveld refinement would be required to obtain more accurate data.

On the other hand, Raman spectroscopy can also provide insight into the crystalline structure of the samples. In **Figure 4.3.2** the Raman spectrum of the substituted sample obtained with synthetic method B, pH 9 and with 5% at. Eu content (YV-E2) is reported, as well as a comparison with the Raman spectrum of the non-substituted reference sample. The Raman spectra of the other substituted samples are similar to that shown in **Figure 4.3.2** and are reported in the **Appendix A.1**, **Figure 9.1.2**.

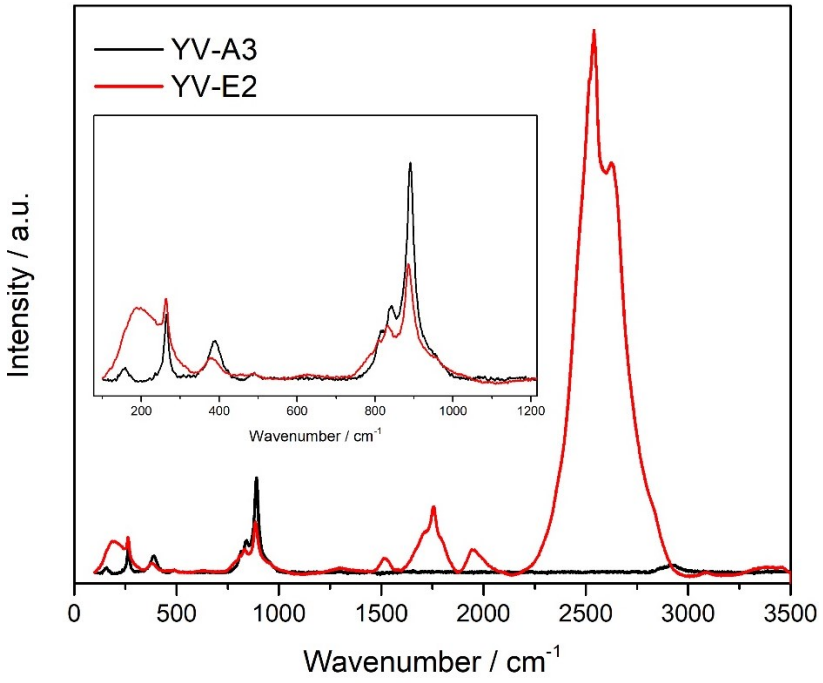

Figure 4.3.2: Raman spectra of the reference sample and of the substituted sample (YV-E2).

As it can be noted from **Figure 4.3.2**, the region of the Raman spectra associated with the internal vibrations of the VO_4^{3-} molecular ion, that is the peaks found in the range from 384 to 891 cm^{-1}, does not significantly change between the non-substituted and the substituted samples, accounting for the retention of the structure of the molecular ion. On the other hand, as regards the region of the Raman spectra associated with the external vibrational modes, that is the peaks found in the range from 264 to 160 cm^{-1}, the same signals can be detected, but an increase in the intensity and a broadening of the signal at 157 cm^{-1} can be noted for the substituted sample. This may be explained by the different interactions in the lattice between Y(III) and VO_4^{3-} due to the replacement of some yttrium ions with europium ones, as in the case of other phosphors (cfr. $CaMoO_4$)[109]. However, the greatest difference relies in the zone of the spectra at wavenumber higher than 1200 cm^{-1}. These signals may be assigned

to the presence of residual surfactant. However, the experimental conditions were the same exploited for the reference sample, but for this sample these signals cannot be detected. Moreover, these signals are very intense, not accounting for the small quantity of residual surfactant present. Further studies on calcined samples (in which the residual surfactant is fully eliminated through combustion) should be performed in order to assess if these signals are actually due to the presence of residual surfactant.

As regards the morphology of the substituted samples, SEM and TEM images were taken for selected samples. Figure 4.3.3 presents the SEM image of the substituted sample obtained exploiting synthetic method A, pH 9 and 1% at. Eu content (YV-E4). From the SEM image, the particles appear to be spherical, and with a diameter of (31 ± 5) nm.

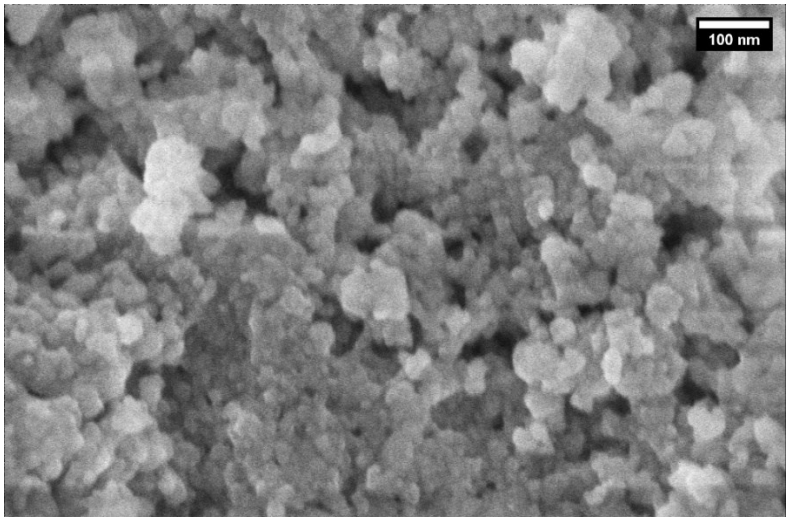

Figure 4.3.3: SEM image of the sample obtained exploiting synthetic method A, pH 9 and 1% at. Eu.

From TEM images (Figure 4.3.4), the quasi-spherical shape of the particles observed in the SEM images was confirmed; however, the morphology is more defined as compared to the non-substituted samples described in the previous paragraph, that is, the particles boundaries are more easily detectable. The particles size was also estimated from TEM images, and the mean diameter is of (27 ± 6) nm, in good agreement with the SEM evaluation. However, the particles of all the samples were aggregated, thus the evaluation of the dimensions must be considered an estimation of the real value, since errors due to the aggregation state of the particles were made. SEM and TEM images of the other samples are similar to those illustrated in Figures 4.3.3 and 4.3.4 and are reported in Appendix A.1, Figure 9.1.3 and Figure 9.1.4.

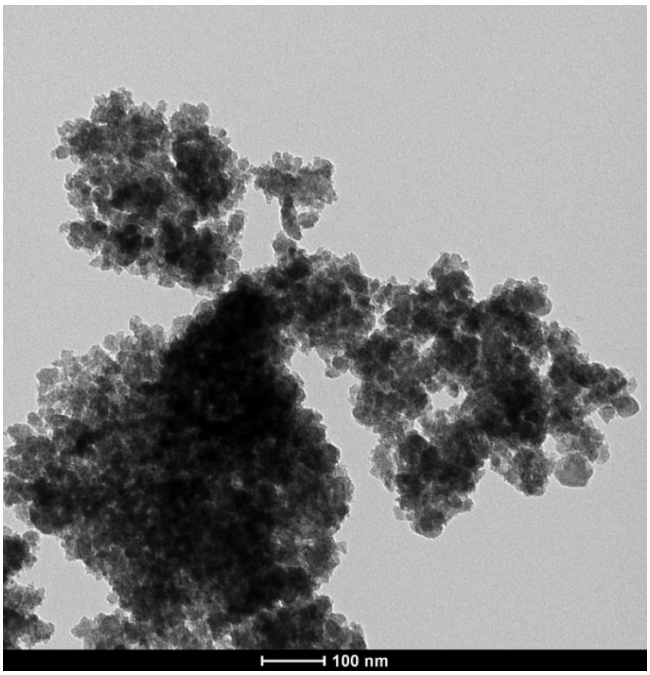

Figure 4.3.4: TEM image of the YV-E4 sample.

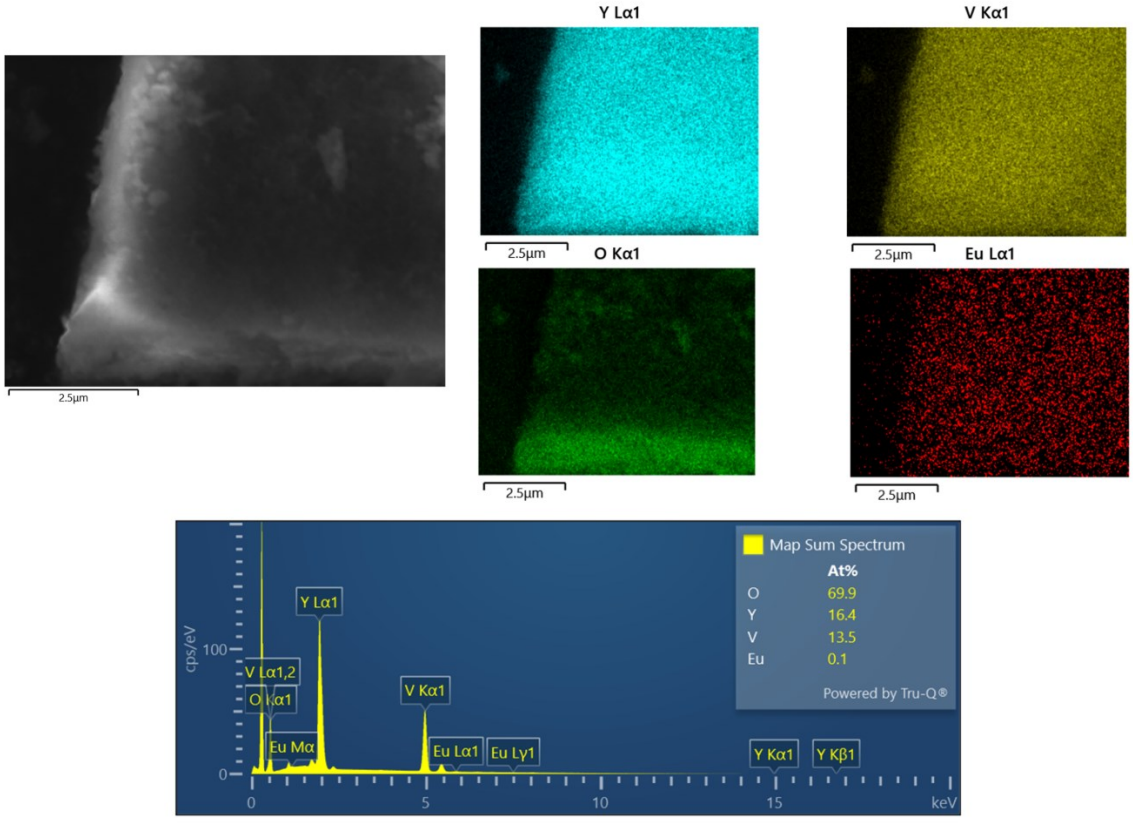

Figure 4.3.5: EDX measurements of the YV-E4 sample.

The EDX image reported in Figure 4.3.5 highlights the homogeneous distribution of the elements throughout the sample, thus accounting for the absence of clusters of europium in the specimen.

Moreover, the relative atomic ratios amongst the elements (Table 4.3.1) are in good agreement with the theoretical formula $Y_{0.99}Eu_{0.01}VO_4$. Moreover, the brighter region on the EDX map of the O atoms is due to a different height of the specimen, which results in a different exposure at the electron beam and therefore a different brightness of the colour, not an effective difference in atomic distribution. This effect in more evident for the O atoms as they are present in higher quantity.

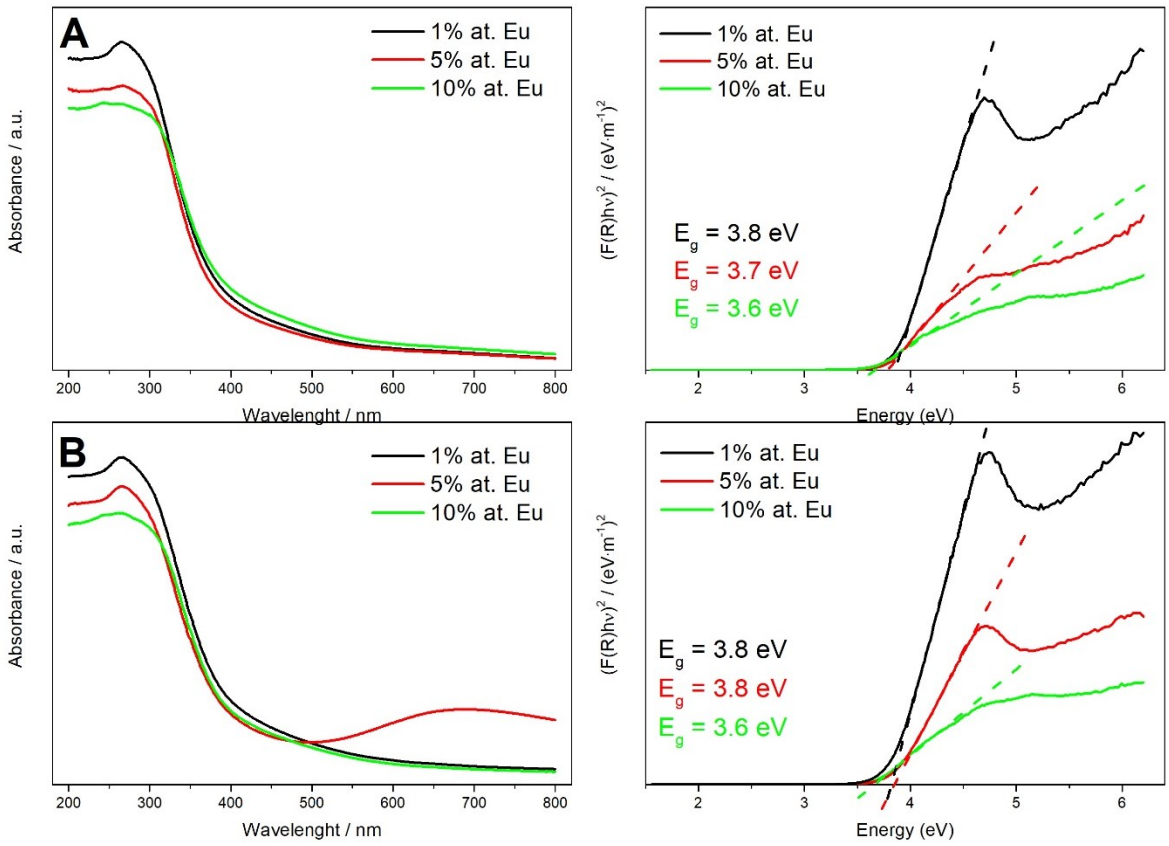

Figure 4.3.6: UV-Vis spectra (left) and Tauc plots (right) of the samples obtained at pH 9 exploiting the synthetic method A (A) or B (B).

As regards the optical properties, a trend in the value of the band gap can be found amongst all the series of increasing Eu content, as reported in Figure 4.3.6 (the reported series are for samples obtained with synthetic methods A and B at pH 9. The last series of sample is reported in Appendix A.1, Figure 9.1.5). The decrease in the E_g is expected, since the presence of the lanthanide ions involves the presence of new localised energy levels between the valence and conduction band, thus allowing an easier electron transfer between the bands.[110] However, as can be noted by Figure 4.3.6, the sample obtained with the synthetic method B, pH 9 and 5% at. Eu (YV-E2) presented a blue colour, as also highlighted by the UV-Vis absorption spectrum. XRD measurements exclude a difference in the structure as an explanation of this behaviour, as the diffractograms are all similar, with no different vanadium or yttrium phases present. Thus, the reason may involve the chemical species and their oxidation state present in the sample. V(IV) possesses a blue colour and may be the responsible for this peculiar property. Also, the

presence of Eu(II) may involve some differences in the colour of the sample, however, Eu(II) is highly unstable when exposed to the air and it would form in a reductive atmosphere, therefore the difference probably relies in the oxidation state of the vanadium. To exclude a possible aleatory result, the synthesis was repeated with the same reaction conditions, and also in the second case the product resulted in a light-blue powder. To evaluate the presence of different oxidation states of the atoms in the specimen, XPS or XAS measurements would be required.

4.3.2 Photoluminescence properties

Photoluminescence studies were carried out on selected substituted samples obtained by miniemulsion approach, checking the differences due to a different Eu content within the same synthetic approach, and those due to the different synthetic approach considering the same Eu content. Thus, samples obtained exploiting the synthetic method B, pH 9 and Eu content levels of 1, 5 and 10% at respectively (YV-E1, YV-E2 and YV-E3), and samples obtained exploiting the synthetic method A, pH 9 and Eu content levels of 1, 5 and 10% at respectively (YV-E4, YV-E5 and YV-E6) were measured, both their fluorescence spectra and their average emission lifetime. As a reference for the emission and excitation spectra of the samples, that of the sample YV-E1 is reported in Figure 4.3.7, with the Eu characteristic emission lines assigned.

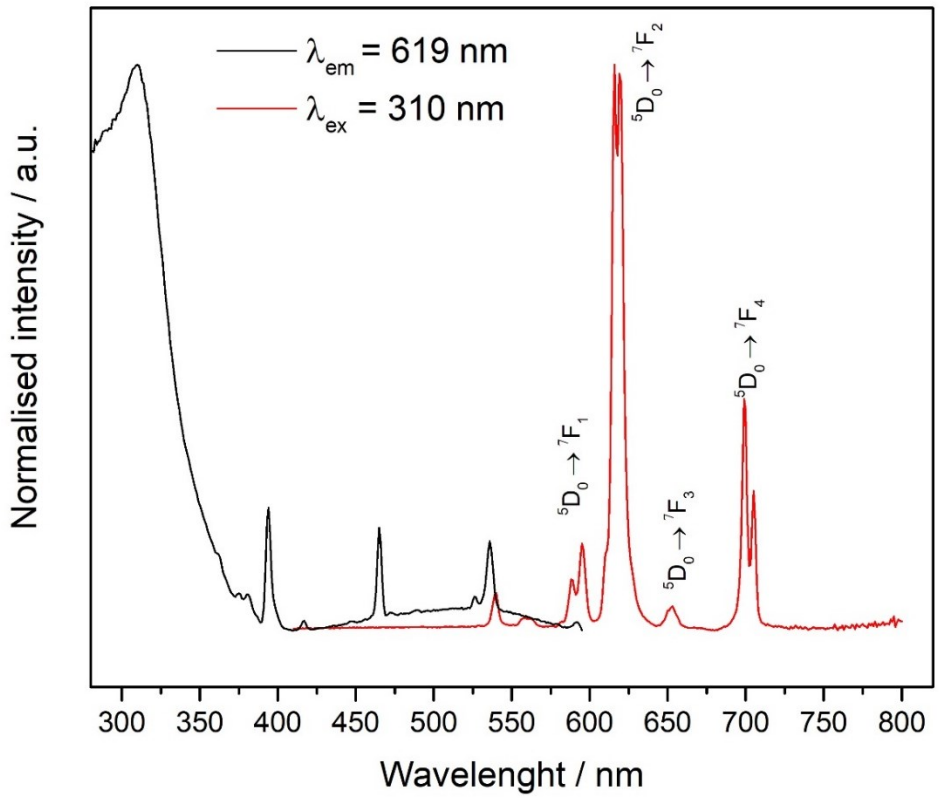

Figure 4.3.7: Excitation (black) and emission (red) spectra of the YV-E1 sample.

As it can be noted by the **Figure 4.3.7**, the excitation of the europium ions can be caused either by a direct excitation of the lanthanide ions (λ_{ex} = 394 nm) or by an energy transfer from the matrix (λ_{ex} = 310 nm). However, the intensity of the light emitted by directly exciting the europium ions (f-f transitions) is lower than that obtained by the excitation of the lanthanide ions by means of energy transfer from the inorganic matrix, accounting for an efficient energy transfer process, in good agreement with the behaviour of the inorganic phosphors. Moreover, the excitation spectrum highlights the presence of two different bands caused by the energy transfer from the matrix (the sharp lines in the range between 350 and 450 nm are due to the direct excitation of the europium ions). The differences with respect to the batch samples are outlined in Paragraph 4.4.2. Another peculiarity of **Figure 4.3.7** relies in the emission spectrum, more in detail in the two signals at 540 and 560 nm respectively. These signals do not belong to the series $^5D_0 \rightarrow {}^7F_J$, and may be due to either the $^5D_1 \rightarrow {}^7F_1$ and $^5D_1 \rightarrow {}^7F_2$ transitions, or to the presence of impurities in the sample. However, the presence of these last two transitions is not very common in Eu(III) substituted inorganic materials. To determine if these signals are due to these transitions, the samples should be synthesised again, and if the signals persisted, time-gated luminescence spectra should be measured through a pulsed excitation source.[96] **Figure 4.3.8** reports different fluorescence spectra of the samples obtained with synthetic method B.

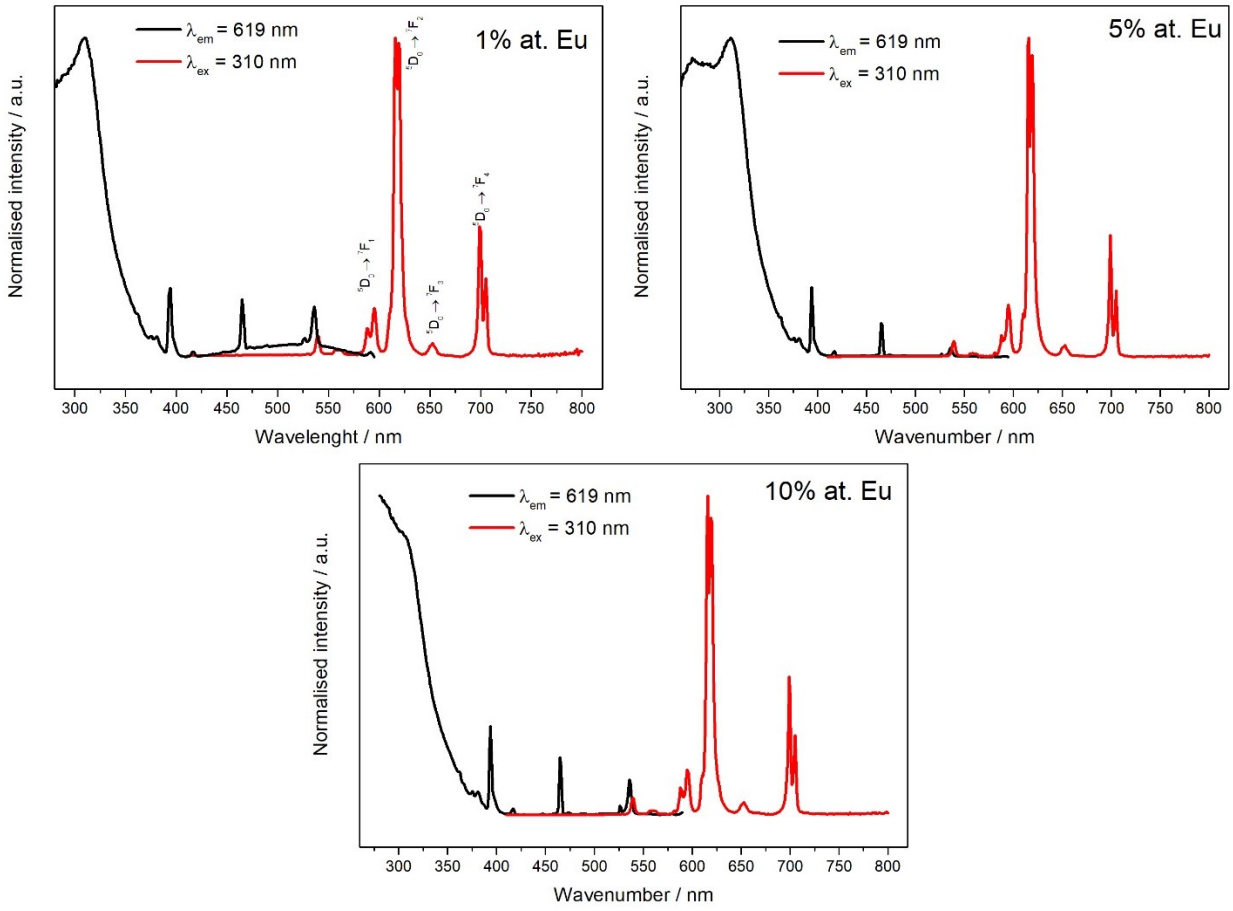

Figure 4.3.8: Excitation (black) and emission (red) spectra of the samples obtained with synthetic method B.

What can clearly be noted is that for samples with higher Eu content, the second excitation band (from 450 to 600 nm) due to the energy transfer from the matrix is not present. Probably, the fewer amount of Eu atoms in the sample (1% at.) led to a less efficient energy transfer process as compared to the other samples, which may explain the different excitation spectra. Moreover, as it can be noted, by increasing the Eu content from 5% at. to 10% at., the intensity of the direct f-f excitation (between 350 and 550 nm) relative to the maximum of the matrix excitation band (310 nm) increases, accounting for a better direct excitation process of the europium ions. This could be due either to the presence of a larger quantity of europium in the sample, or to the presence of a better energy transfer among europium ions with increasing lanthanide content. As regards the YV-E1 sample (synthetic method B, pH 9, 1% at. Eu), it was also noted that, by exciting the sample at 394 nm (thus directly exciting the Eu atoms), an emission band due to the emission of the matrix could be observed (Appendix A.1, Figure 9.1.6). This hints at a back-transfer from the Eu ions to the matrix, more relevant as compared to the other samples, but further experiments are required to definitively prove it.

As regards the samples obtained with the synthetic method A, Figure 4.3.9 summarises the different fluorescence spectra of the samples.

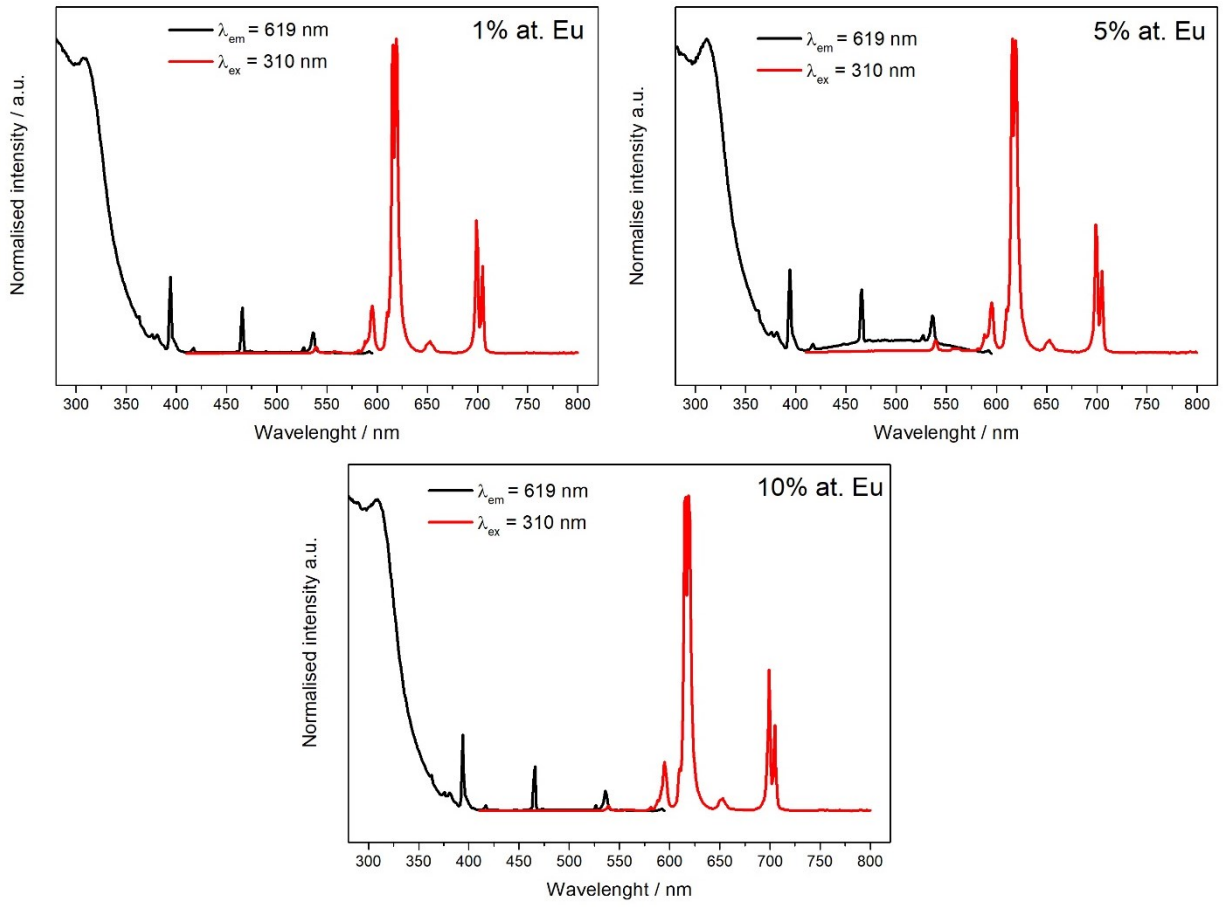

Figure 4.3.9: Excitation (black) and emission (red) spectra of the samples obtained with synthetic method A.

For these samples, similar conclusions as those for the samples obtained with synthetic method B can be drawn, with the YV-E5 sample (5% at. Eu content, synthetic method A, pH 9) being similar to the YV-

E1 sample. Indeed, sample YV-E5 presents two excitation bands probably due to a less significant energy transfer process from the matrix, and also presents a significant energy back-transfer from the Eu ions to the matrix when directly exciting the f-f transition at 394 nm (Appendix A.1, Figure 9.1.6). However, the fact that different synthetic methods led to different outcomes in the photoluminescence measurements highlights that the different methodology of addition of the NaOH had an actual impact on the product properties.

As regards the emission lifetime measured for these samples, no fitting of the decay was possible for the samples obtained with synthetic method B. On the other hand, for samples obtained with synthetic method A, the decay was fitted with a two exponential function, thus confirming the energy transfer process (one term is due to the relaxation of the europium ions directly excited, the other term is due to the relaxation of europium ions excited by means of energy transfer from the matrix).[86] However, the emission lifetime of the samples slightly increased with increasing Eu content, as opposed to what predicted by the literature.[61] This is probably an hint at the non-homogeneous distribution of the Eu ions in the yttrium vanadate matrix, which could not be highlighted by means of EDX measurements because of its different spatial resolution. However, further studies on these systems are required in order to fully comprehend the fluorescence properties of the samples.

4.4 Comparison with batch synthesis

As it was previously anticipated, in this chapter the structural and optical properties of non-substituted and Eu(III)-substituted YVO_4 synthesised in inverse miniemulsion system are compared to the same properties of the YVO_4 synthesised in batch. Also, the dependence of the product properties on the reaction conditions is highlighted. Since the synthesis and characterisation of the yttrium vanadate through a batch approach were conducted as part of a previous work – carried out as part of the Double Degree project in the group of Prof. Dr. Klaus Müller-Buschbaum at the JLU University in Gieβen – in this chapter only the differences as compared to the inverse miniemulsion system are highlighted, not describing the results of the batch synthesis in detail. The variation of the reaction conditions in the batch synthesis were equal to those performed in the miniemulsion system, to allow a proper comparison of the results.

4.4.1 Comparison of structural properties and their dependence with reaction conditions

Variation of the vanadium precursor. As regards the miniemulsion system, in paragraph 4.2.2 it was shown that no major differences regarding both the structural and morphological properties of the products obtained exploiting either the orthovanadate or the metavanadate precursors could be highlighted, apart from the product obtained at autogenic pH 4 for the reasons explained in Paragraph 4.2.2. On the other hand, as regards the yttrium vanadate obtained through a batch synthesis, the effect

of the vanadium precursor on the product morphology and particles' size was quite different. In this regard, as can be noted in Figure 4.4.1, an example of the products obtained at pH 9 and with a reaction time of 3 h, the orthovanadate precursor led to spherical nanoparticles with a diameter of (50 ± 10) nm, whereas the metavanadate precursor led to spindle-like nanoparticles, possessing a length of (120 ± 10) nm. In both cases, the primary particles are aggregated into larger particles with no defined shape.

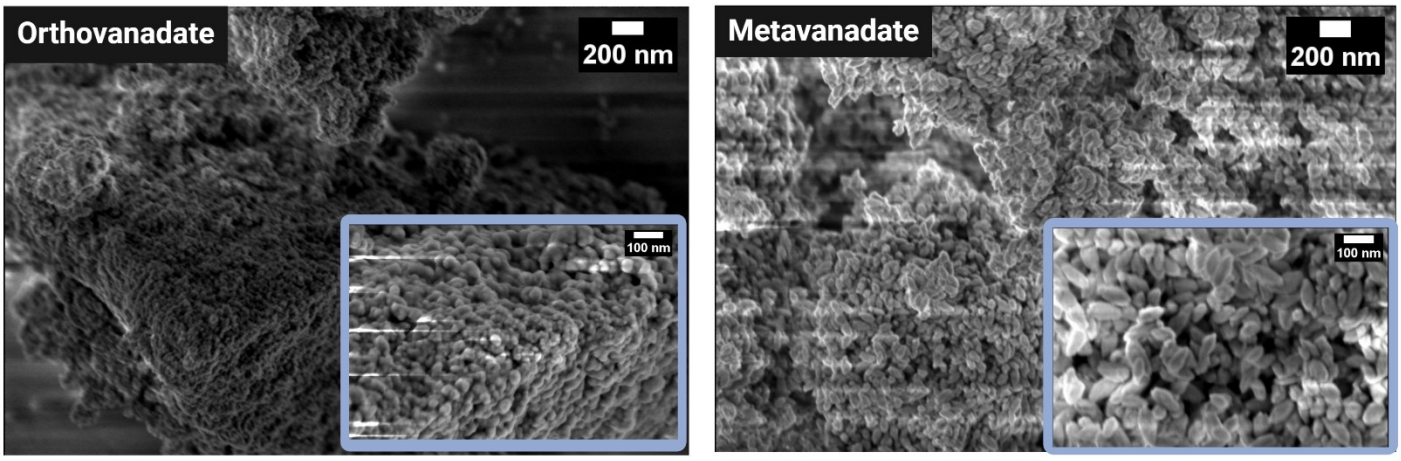

Figure 4.4.1: SEM images of the YVO_4 nanoparticles obtained via a batch synthesis with the two different precursors. The exploited reaction conditions were: 3 h as reaction time, room temperature and pH 9.

As can clearly be noted comparing this image with Figure 4.2.3, the synthesis with metavanadate as vanadium precursor endures a significant variation when transferred to the confined space system. Indeed, both morphology and particles size result to be quite different compared to those of the particles obtained via batch synthesis, as for the miniemulsion approach, the particles resulted spherical and with a diameter of roughly 30 nm. A further difference relies on the synthesis with the metavanadate at pH 4: in the miniemulsion system, the reaction led to almost no yttrium vanadate product (very low intensity signals in the diffractogram) and to the clear presence of other by-products, probably polyoxovanadates species, as described in detail in paragraph 4.2.2. On the other hand, in the batch synthesis there is the clear formation of yttrium vanadate as product and seemingly no by-product, as observed from the XRD pattern, even if the yellow colour of the product powder may indicate the presence of impurities (Figure 4.4.2). However, the calcination of the latter so-obtained product at 500 °C for 2 h led to the formation of V_2O_5 phase, arising from the thermal degradation of polyoxovanadates species, present in the sample even if in lower quantities as compared to the miniemulsion system. The fewer amount can be noted as the signals at 13.1 and 13.8° 2θ for the sample before the calcination treatment are not clearly visible for the batch sample (red line), as noted in the diffractogram reported in Figure 4.4.2, as compared to the diffractogram of the miniemulsion sample (black line), in which these two signals are clearly visible.

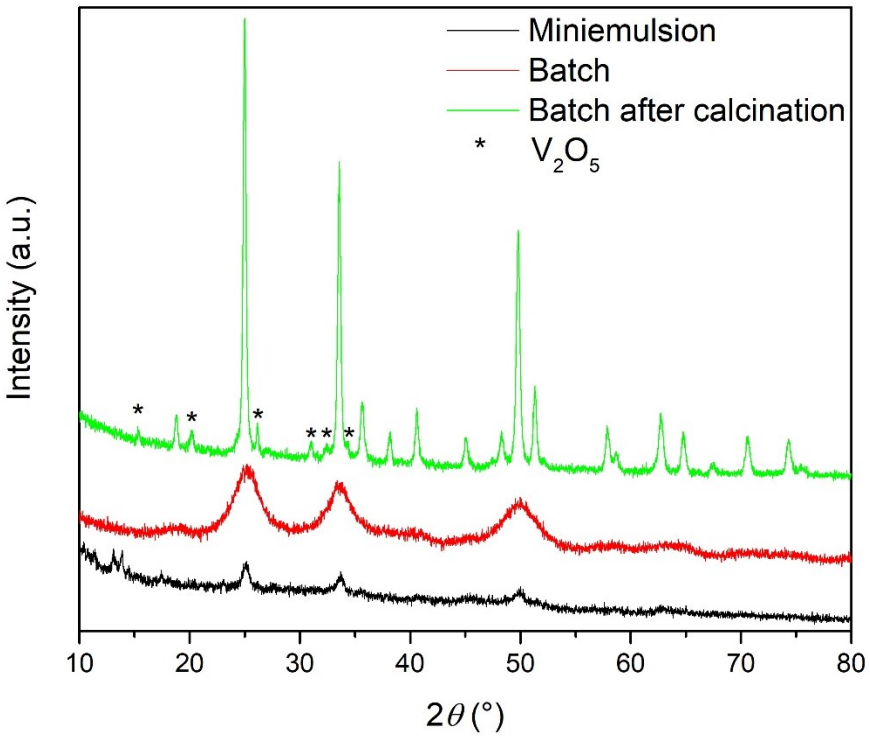

Figure 4.4.2: XRD diffractograms of the YVO_4 obtained in miniemulsion and batch at pH 4 with metavanadate precursor. The diffractogram of the batch sample after calcination is also reported.

Variation of the pH of the reaction environment. As regards the batch synthesis, the different vanadium precursors also present a different behaviour by increasing the pH of the reaction environment, while for the miniemulsion system, the pH value did not significantly affect the product properties (apart for pH value of 4 with the metavanadate as educt). In the batch synthesis, by exploiting the orthovanadate as vanadium precursor, an increase in crystallinity is found up to pH 9, while the product obtained at pH 11 presented a lower degree of crystallinity (Figure 4.4.3).

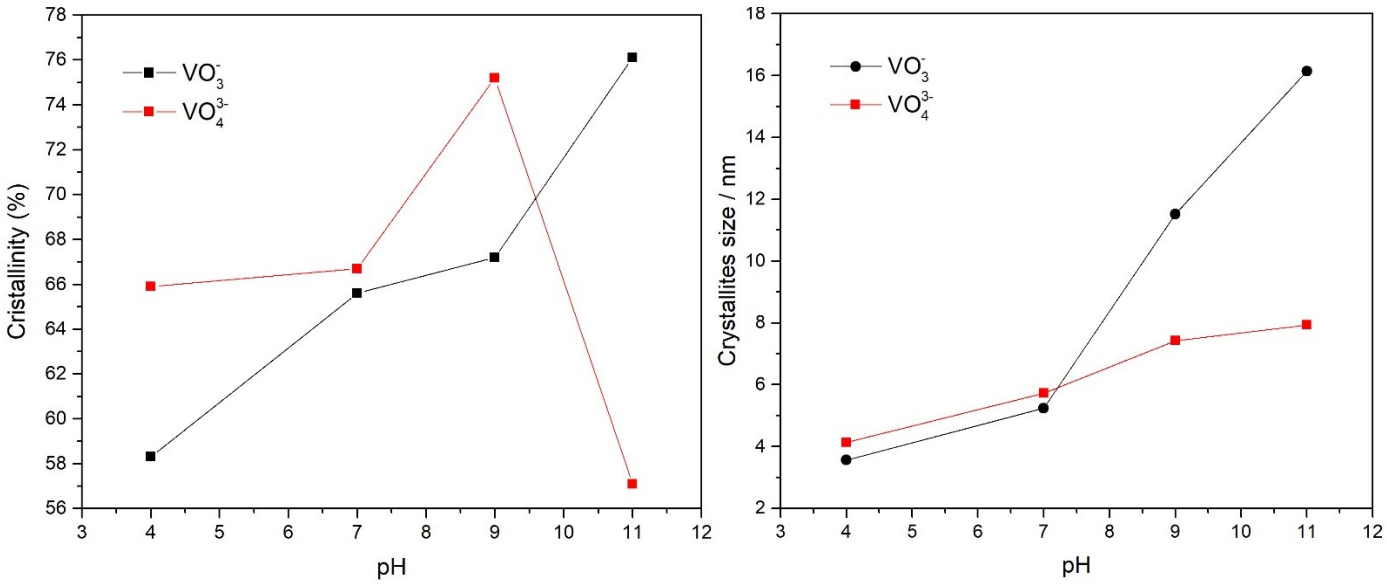

Figure 4.4.3: Crystallinity and crystallites size of the different sample obtained in batch at different pH values with the two different vanadium precursors.

This could be explained with the reaction mechanism, which involves the initial precipitation of $Y(OH)_3$ which then reacts with the VO_4^{3-} ions to yield the product. However, at pH values of 11 or higher, it is possible that the $Y(OH)_3$ formed is more stable and less reactive towards the orthovanadate ions, or else, the complete precipitation of the $Y(OH)_3$ may hinder the reaction with the orthovanadate ions. Thus, it is likely that at higher pH values, a complete precipitation of the $Y(OH)_3$ occurs, while at pH values up to 7 the concentration in solution of Y(III) ions is still non negligible; these free ions may be responsible for the reaction to occur with the orthovanadate ions, while at higher pH values the reaction is slowed down by the reduction of the amount of these Y(III) free ions in solution, resulting in a higher content of $Y(OH)_3$ in the product. This conclusion is also confirmed by the XRD measurement conducted on the sample obtained with the orthovanadate as vanadium precursor at pH 11 after calcination (500 °C, 2 h), in which signals attributed to the presence of Y_2O_3 can be detected (**Figure 4.4.4**), probably deriving from the dehydration of the $Y(OH)_3$.

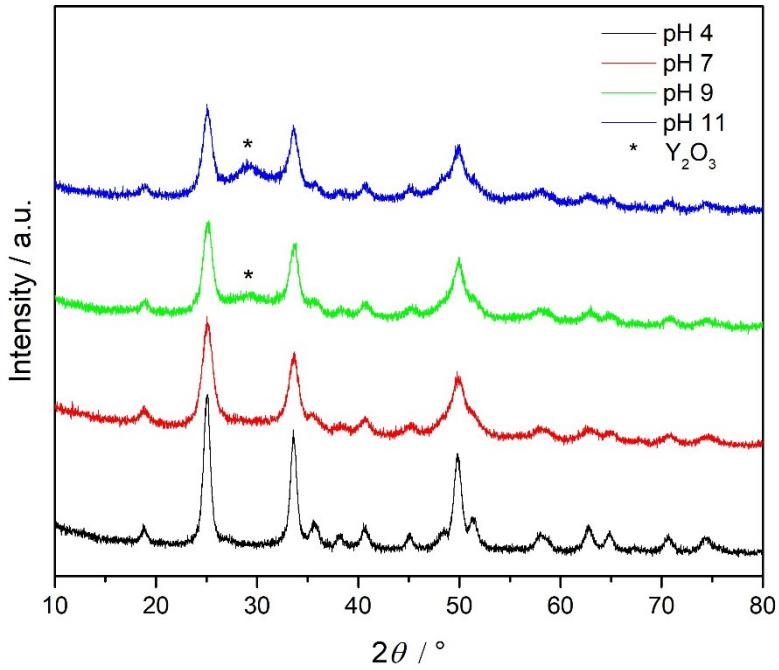

Figure 4.4.4: XRD measurements of the yttrium vanadate samples obtained at different pH of the reaction environment via batch synthesis and by exploiting the orthovanadate as vanadium educt, after calcination.

On the other hand, by exploiting the metavanadate as vanadium precursor, a constant increase in crystallinity and crystallites size with increasing pH value can be detected (Figure 4.4.3). Also in this case, this behaviour can be related to the reaction mechanism, which, in the case of VO_3^- anions, involves the hydroxide ions as intermediate reactants. Indeed, the hydroxide ions react with the metavanadate ions to yield the orthovanadate species, which finally react with the $Y(OH)_3$ to yield the yttrium vanadate, following the proposed mechanism:[80]

$$Y^{3+}_{(aq)} + H_2O \xrightarrow{OH^-} Y(OH)_3 \qquad \textbf{4.2}$$

$$VO^-_{3\,(aq)} + 2OH^-_{(aq)} \rightarrow VO^{3-}_{4\,(aq)} + H_2O \qquad \textbf{4.3}$$

$$Y(OH)_3 + VO^{3-}_{4\,(aq)} \rightarrow YVO_4 + 3OH^-_{(aq)} \qquad \textbf{4.4}$$

Thus, a higher concentration of hydroxide ions may favour the reaction between metavanadate and hydroxide ions themselves, promoting the formation of the product. It is also noteworthy that, in batch synthesis, the order of addition of the metavanadate and hydroxide species to the solution of yttrium nitrate leads to different outcomes of the reaction. Indeed, by adding the metavanadate first, the precipitation of polyoxovanadates species occurs, which then hardly convert to the desired product. On the other hand, by adding the sodium hydroxide first, a more reproducible reaction seems to occur, probably due to the initial precipitation of $Y(OH)_3$ instead of polyoxovanadates species, as highlighted by the XRD measurements. Figure 4.4.5 summarises the XRD measurements of the samples obtained via batch synthesis. Regarding the crystallinity and crystallites size of the products obtained via batch

synthesis compared to those obtained through the miniemulsion system, the orthovanadate educt led to products with similar crystallinity and crystallites size (Figure 4.4.3) On the other hand, the metavanadate precursor led to quite different outcomes in the two different systems: the yttrium vanadate synthesised in batch appears to be more dependent on the reaction conditions – in this case, the pH value – as compared to yttrium vanadate synthesised in miniemulsion, leading to more crystalline products, up to crystallinity values of 70 or 80% at pH 9 and 11 respectively, with bigger crystallites sizes, up to 12 and 16 nm respectively. The values of crystallinity and crystallite size for the products obtained via the batch synthesis are reported in Figure 4.4.3.

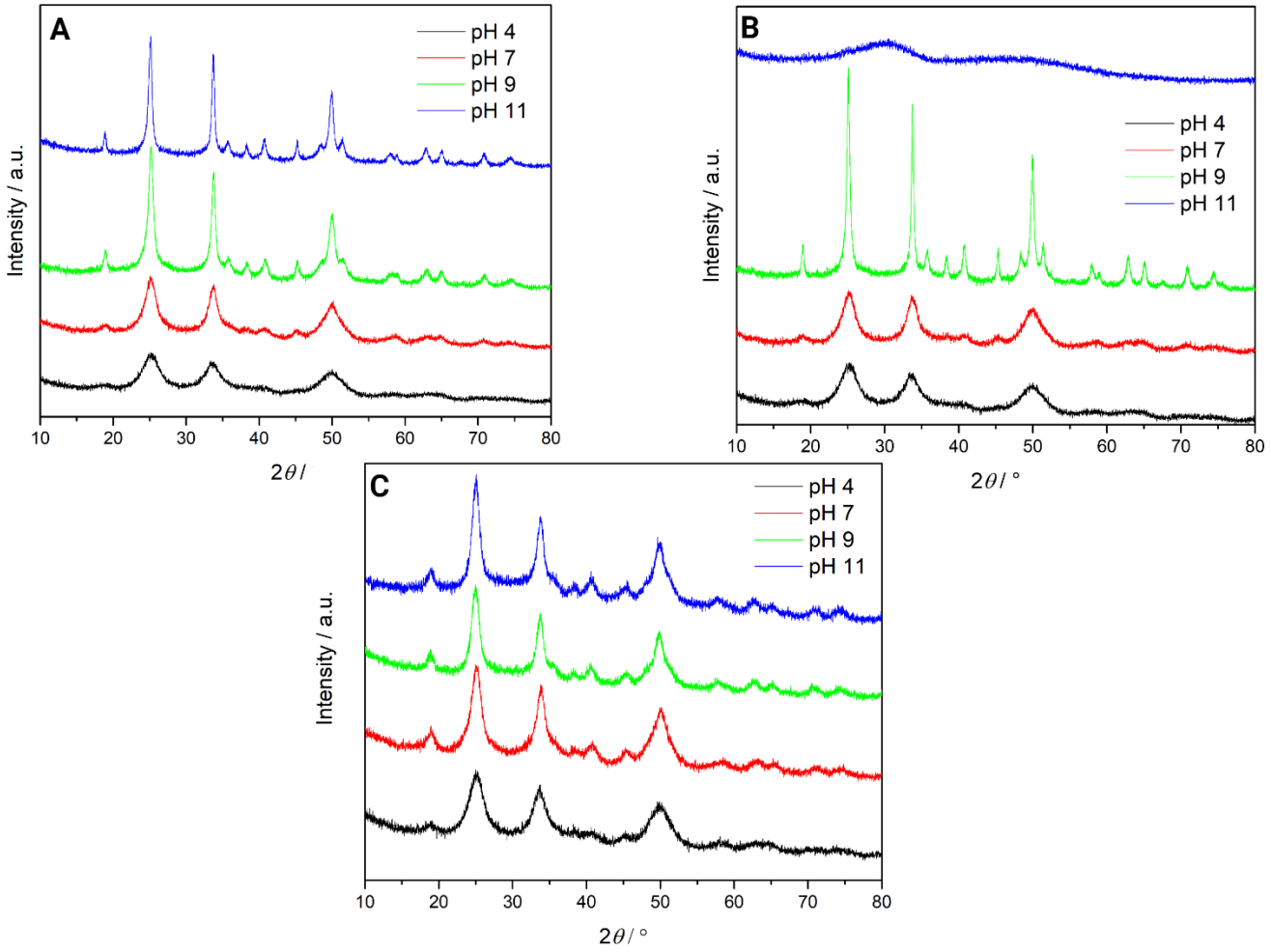

Figure 4.4.5: XRD measurements of the yttrium vanadate obtained via batch synthesis and exploiting either metavanadate, sodium hydroxide added first (A) or last (B), or orthovanadate (C) as vanadium precursors.

As regards the particles size and morphology (Figure 4.4.6) for the products obtained in batch, a higher pH value seems to promote the formation of more shape-defined and independent primary particles, as well as bigger primary particles, highlighting the fundamental role of the hydroxide ions in the reaction mechanism. Moreover, exploiting the metavanadate as vanadium precursor, at pH values of 9 and 11 a clear spindle-like morphology (particles size of (120 ± 10) nm and (160 ± 20) nm respectively) of the particles can be noted by SEM images, even though no possible mechanism for the formation of this morphology could be found in literature. Figure 4.4.6 reports the SEM images of the yttrium vanadate

obtained at different pH values with the two different vanadium precursors. Regarding the SEM images of the products at pH 4 and 7, the estimation of the particle dimensions by the SEM images was not possible, due to the too high degree of aggregation and not well-defined shape of the particles. Comparing the dependence of the properties of the products obtained in batch synthesis with the different pH values just described with the same dependence of the products obtained in the miniemulsion system previously described, a clear difference can be noted. Indeed, the properties of the products obtained in the miniemulsion system do not depend on the experimental pH value, as the particles possess a spherical shape and a diameter of roughly 30 nm regardless of the pH value. This could be due to the fact that the templating action of the droplets of the miniemulsion possesses a stronger effect on the product properties than the pH value. The forming particles are bound to grow in a confined system of a spherical shape, and therefore also the final morphology of the products resulted to be spherical, where in the batch synthesis the morphology resulted as spindle-like.

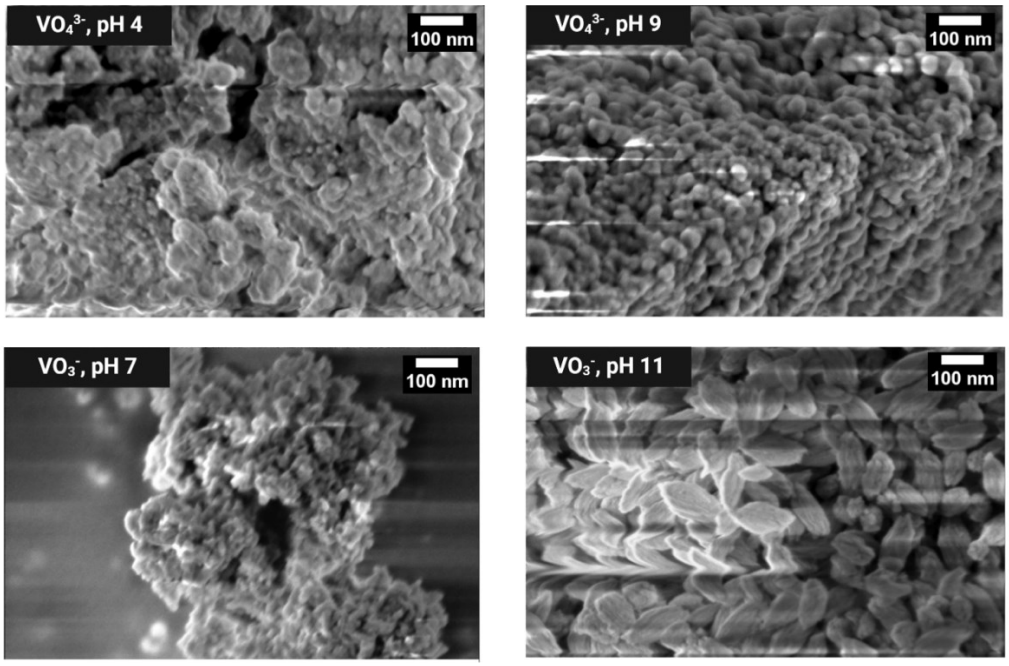

Figure 4.4.6: SEM images of the yttrium vanadate samples synthesised in batch at different pH values and with different vanadium precursors. The reaction time was 3 h.

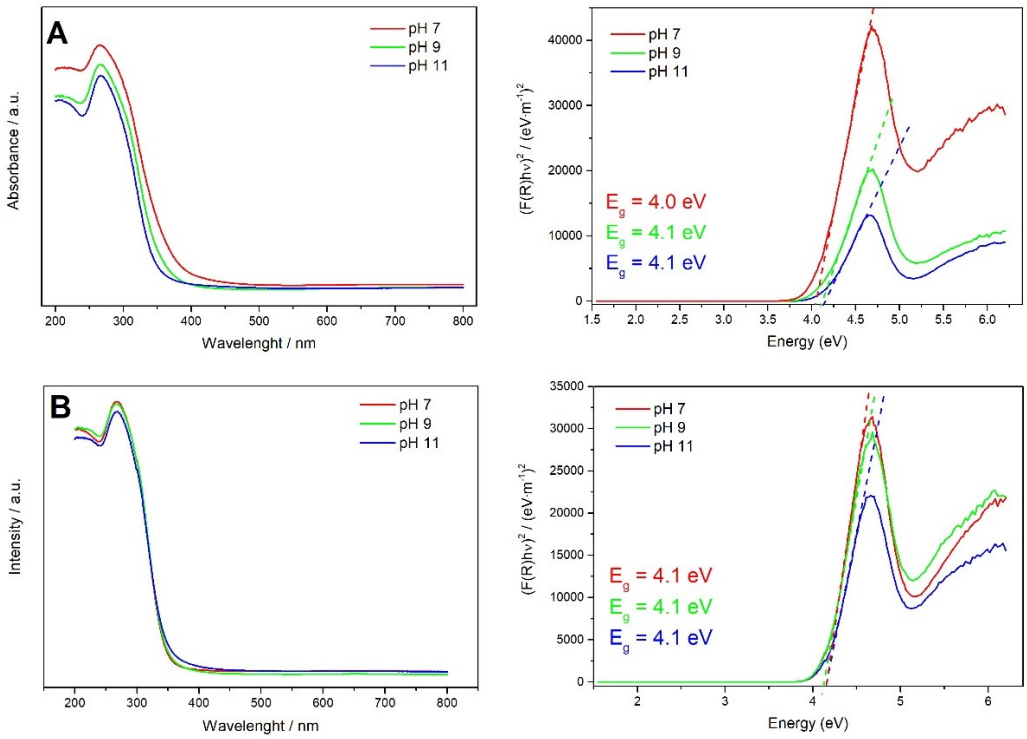

Figure 4.4.7: Absorbance spectra (left) and Tauc plots (right) of the yttrium vanadate synthesised in batch at different pH values and exploiting the metavanadate (sodium hydroxide first) (A) and orthovanadate (B) as vanadium precursors.

As regards the optical bandgap, the samples obtained in batch, both from the orthovanadate and metavanadate precursors, and at different pH values (pH ≥ 7), possess comparable band gap values of roughly 4.0 eV estimated with the Tauc plot (Figure 4.4.7). Moreover, these samples appear as white powders, as opposed to the yttrium vanadate synthesised in miniemulsions, which results as a beiger colour powder. The different colour is also confirmed by the absorption spectra, which, for the case of batch samples, are typical of a white powder, as they don't present absorption in the visible range. The bandgap values are also comparable with the values of the samples obtained via the miniemulsion approach, with the estimated values of the former being slightly higher than those estimated for the miniemulsions samples. The difference in band gap energies between the values estimated for the batch sample and those estimated for the miniemulsion samples is negligible, since the Tauc plot method itself is subjected to errors in the definition of the linear region of the Tauc plot. However, the small difference may be due to a different defects content in the samples, which in this case seems to be higher in the batch samples since they present a slightly higher band gap energy. Another possibility may rely in the quantum confinement effect, which in this case would highlight bigger particles for the batch synthesis as opposed to the miniemulsion samples, since smaller particles are expected to present higher band gap values. However, this is in contrast to the particle size estimated be SEM and TEM images, thus the different particle size may not be the cause of the small difference in band gap value.

Finally, Raman measurements on yttrium vanadate obtained in batch synthesis with metavanadate as vanadium educt and at two different pH values (7 and 11) highlight the presence of the vibration modes

typical of the YVO_4 zircon-type structure, and the absence of the C-H bonds since there is no signal in the region around 3000 cm^{-1}, as expected since no surfactant was used for the batch synthesis (**Figure 4.4.8**).

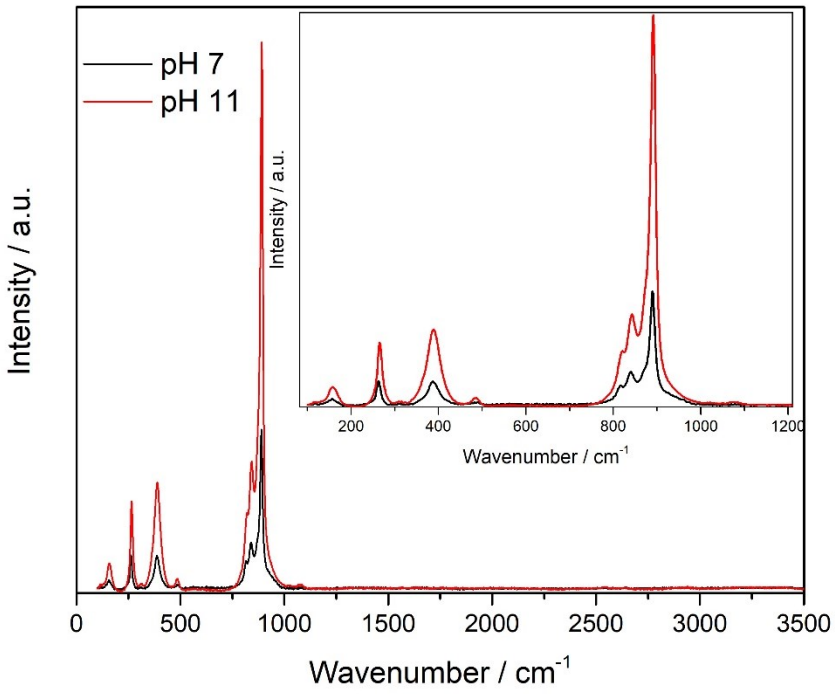

Figure 4.4.8: Raman spectra of YVO_4 samples obtained in batch at two different pH values, using ammonium metavanadate as vanadium precursor.

In conclusion, by comparing the properties of the sample obtained via batch synthesis and via the miniemulsion approach, it can be stated that the implementation of the confined space system in the solution synthesis resulted in severe changes of the product particles shape and size, as well as in the dependence of the reaction outcomes on the variation of the reaction conditions. Indeed, the morphology of the products obtained in the miniemulsion framework results to be quasi-spherical, with both different pH values of the reaction environment and with different exploited vanadium precursor. When considering samples obtained exploiting the metavanadate as vanadium precursor, the particles size is much smaller than that of the particles synthesised in batch synthesis (roughly 30 nm vs particles size up to 160 nm for the batch synthesis) and is roughly constant by varying the pH of the reaction environment. Thus, it can be concluded that for the batch synthesis there is a higher dependence of the reaction outcomes on the reaction parameters, whereas the miniemulsion system is more affected by the miniemulsion system itself rather than the reaction parameters. That is, when exploiting the confined space system, the templating effect due to the confinement of the reaction inside the droplets is more effective on the product properties than the reaction conditions. Moreover, in batch synthesis, the exploited reaction time was of 3 h, while in the miniemulsion system 24 h were chosen because at first after 3 h the reaction was visibly still not completed (yellow colour of the miniemulsion not yet converted to white). This may suggest a slower reaction kinetics in the miniemulsion system – probably due to the slower mixing of the reagents inside the droplets, or a slower reaction between the metavanadate and

hydroxide ions – which may also explain the smaller crystallites size and lower degree of crystallinity of the products as compared to the products obtained in batch synthesis. However, as anticipated in previous paragraphs, a possible alternative explanation could be the stabilisation of a different stage in the Ostwald's step rule when performing the reaction in the confined space, which may also explain the different crystallinity and crystallites size. A longer reaction time should be tested, in order to prove if the obtained product properties may further vary with the proceeding of the reaction, and therefore assess which of the two possible explanations in more reliable. However, for this purpose more stable miniemulsions would be required, since the exploited system was stable for the 24 h chosen, but not for longer time.

On the other hand, as regards the structure, no major differences can be noted amongst the different products, with the zircon-type yttrium vanadate structure being the crystalline structure of all the products. This is also confirmed by the similar Raman spectra of the different products. Moreover, regarding the optical properties, negligible differences in the band gap value can be noted, and the main difference relies in the different absorption spectra, and thus in the colour, of the products obtained via batch synthesis and via the miniemulsion system

4.4.2 Comparison of the luminescence properties

For the batch synthesis, the reference excitation and emission spectra of the non-substituted sample was measured (Figure 4.4.9).

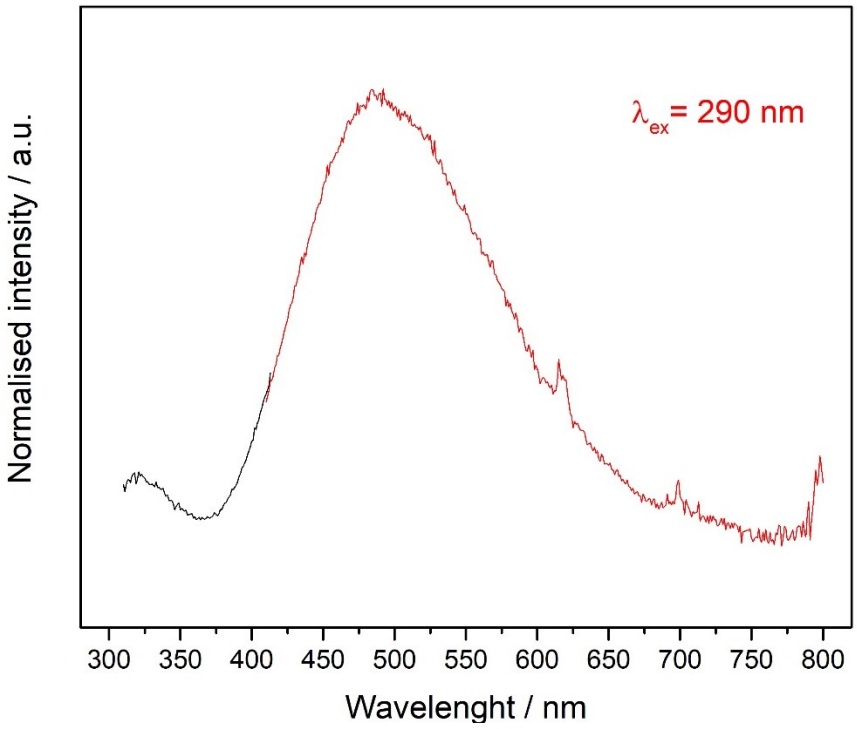

Figure 4.4.9: Excitation (black) and emission (red) spectra of the non-substituted yttrium vanadate synthesised in batch.

As it can be noted, the non-substituted matrix presents a broad emission band centred at 490 nm. In Figure 4.4.9, the presence of some signals attributed to the emission of the Eu(III) ions (at roughly 600 and 700 nm) can be detected, probably due to the presence of impurities in the sample or in the cuvette.

As regards the substituted samples, Figure 4.4.10 summarises the excitation and emission spectra of the different samples.

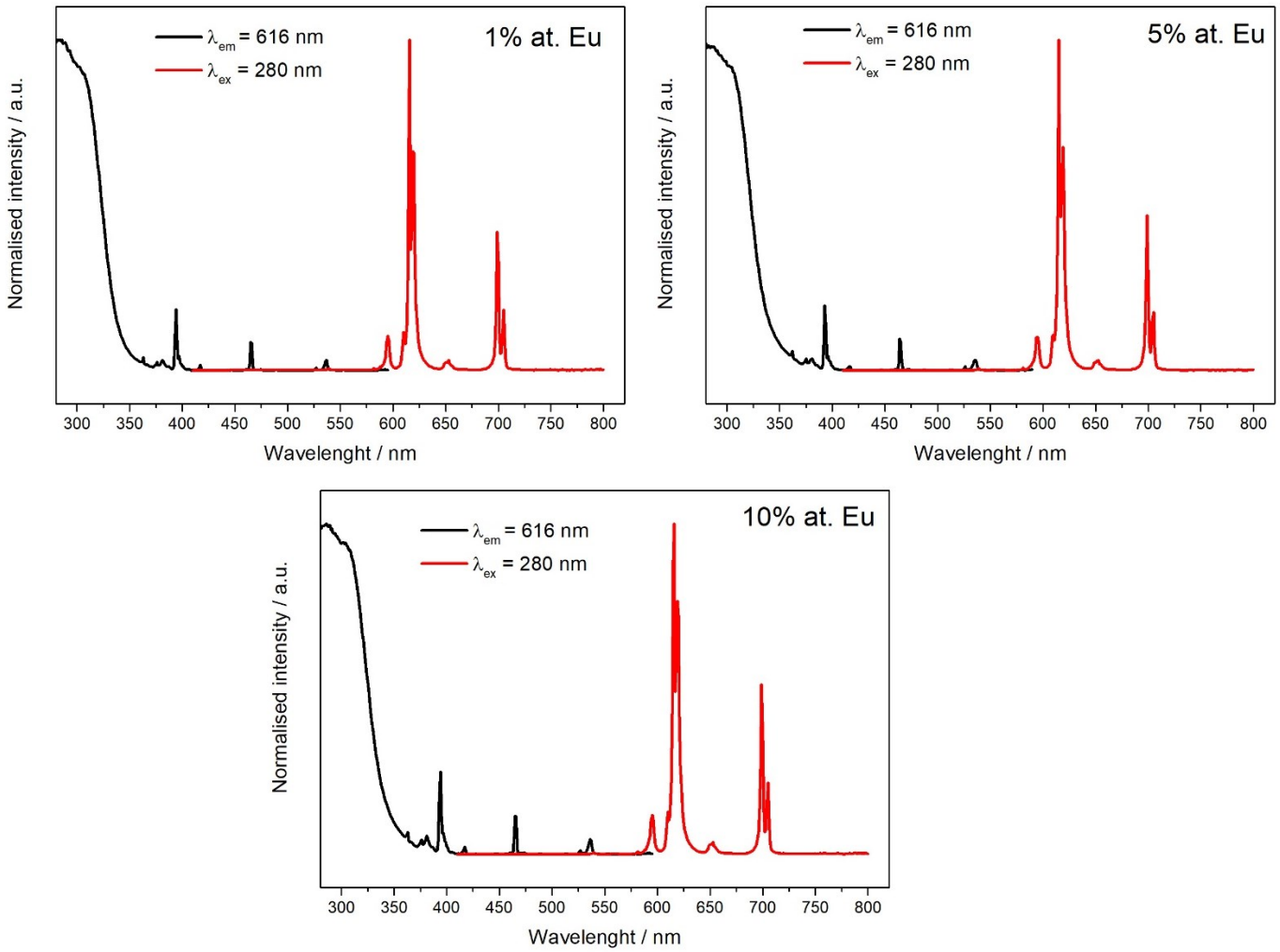

Figure 4.4.10: Excitation (black) and emission (red) spectra of the substituted samples synthesised in batch.

By comparing Figure 4.4.10 with Figure 4.3.8 and Figure 4.3.9, it can be noted that the substituted yttrium vanadate samples obtained through the batch synthesis present a more regular excitation and emission spectra with varying Eu content, with no sample that presents two matrix excitation bands. Moreover, the signals at 540 and 560 nm in the emission spectra are not present, either for a difference in the structure of the samples or for the absence of impurities. By increasing the Eu content in the samples, it can be noted that the intensity of the bands for the direct excitation of the Eu ions (the black lines in the excitation spectra) in the 1% at. Eu and the 5% at. Eu samples increases slightly, accounting for an efficient energy transfer from the matrix to the lanthanide ions. The same bands for the 10% at. Eu sample are more intense, because of the presence of a larger quantity of Eu ions. Another observation

is that by directly exciting the f-f transitions of the Eu ions (λ_{ex} = 394 nm), the emitted intensity was lower as compared to the miniemulsion samples at equal Eu content, which is a signal of a more homogeneous distribution of the Eu ions in the yttrium vanadate matrix in the case of batch samples. Indeed, if the local concentration of Eu ions in higher due to an inhomogeneous distribution of the Eu in the matrix, the overall emission intensity obtained by directly exciting the Eu ions is higher. Moreover, by exciting the f-f transitions of the Eu ions, no energy back-transfer could be noted (Appendix A.1, Figure 9.1.6), again accounting for a more homogeneous distribution of the Eu ions in the yttrium vanadate matrix for batch samples. Finally, considering the average emission lifetime of these samples, a double exponential function was exploited to fit the decay time, confirming the presence of the energy transfer from the matrix. However, as opposed to the miniemulsion samples, with increasing Eu content, the emission lifetime decreases according to the literature, due to the higher probability of ion-ion cross relaxation leading to non-radiative decaying processes.[61]

All these conclusions hint at the fact that in batch samples the Eu ions are distributed more homogeneously as compared to the miniemulsion samples, thus leading to more promising photoluminescence properties. This finding is in good agreement with the observation that the morphology of the miniemulsion samples is not well-defined as opposed to the case of the batch samples, further corroborating the hypothesis that the miniemulsion system may lead to two possible effects for this synthesis: either the reaction kinetic is slower as compared to the batch synthesis, and thus longer reaction times are required, or the fact that in the miniemulsion system, a different stage rather than the thermodynamically stable one in the Ostwald's step rule is stabilised, leading to the different product properties.

4.5 Synthesis of YVO_4 nanoparticles within mesoporous metal oxides

The synthesis of the YVO_4 particles was performed exploiting three different mesoporous metal oxides, that is silica (SiO_2), zirconia (ZrO_2), and titania (TiO_2). Each of these metal oxides was synthesised (and characterised) possessing three different pore size distributions, an example of which is supplied in Figure 4.5.1, in a previous work carried out at the JLU University of Gieβen in the working group of Prof. Dr. Bernd Smarsly. The details of the synthesis of the mesoporous metal oxides exile the scope of this thesis and are not herein discussed, and the general concepts of the synthesis of mesoporous materials are delineated in paragraph 2.2.2.

The synthesis of yttrium vanadate nanoparticles directly inside the pore system of different mesoporous materials was conducted by means of thermal annealing of the precursors previously adsorbed inside the pores through the IWI approach (Paragraph 2.2.3). The molar ratios between the yttrium and vanadium precursors was kept constant and equal to Y^{3+}:VO_4^{3-} (or VO_3^-) = 1:1. The final products analysed consisted of the mesoporous material with the inorganic product adsorbed within the matrix, since the separation of the synthetised YVO_4 from the metal oxides supports was not possible. One exception may

be the YVO_4 supported on mesoporous silica, as the SiO_2 support may be dissolved in a strong alkali environment, whereas the YVO_4 particles should not dissolve in such ambient. However, due to the small amount of sample available (roughly 50 mg considering both the product and the mesoporous support), the possible tests on the YVO_4 particles isolated from the porous matrix were not carried out. Moreover, this part of the thesis represents an initial and preliminary study on the synthesis in the confined space provided by the mesoporous materials, since no comparison could be found in literature and therefore a starting study of the novel synthetic approach was necessary. In this chapter, the results obtained from this preliminary study are reported, also highlighting the critical issues of the system, but further studies on the dependence of the product properties on the reaction conditions have to be addressed in future works.

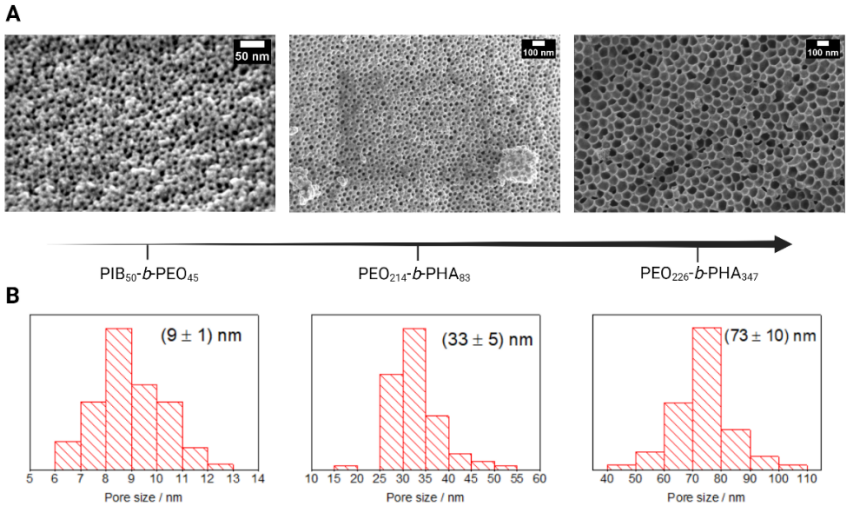

Figure 4.5.1: SEM images of the mesoporous silica supports (A), and the associated pore size distributions estimated from the SEM images (B). On the arrow are reported the names of the polymers exploited for the soft-templating.

The three different pores sizes distributions likely involve different effects on the product features since the effects of the confined space depend on the dimensions of the space itself. As can be noted from Figure 4.5.1, the exploited pores size distributions vary significantly, ranging from 9 nm to 70 nm. However, the work of this thesis primarily focussed on the mesoporous* materials possessing pores size distributions of roughly 30 and 70 nm, with only a sample obtained exploiting the TiO_2 possessing pores of roughly 9 nm in diameter. The sample named YVS-03 (cfr. Paragraph 4.5.1) was chosen as reference sample since all the possible characterisation techniques were performed on the sample, allowing for a proper determination of the outcome of the synthesis. The other samples are introduced and discussed as far as the performed analyses allow.

* In this work, the term "mesoporous" involves also the materials possessing pore diameter larger than 50 nm for a matter of simplicity in writing.

4.5.1 Reference sample

The YVS-03 reference sample was synthesised exploiting as support the mesoporous silica possessing a pores diameter of 30 nm, $Y(NO_3)_3 \cdot 6H_2O$ and NH_4VO_3 as yttrium and vanadium precursor respectively. The details of the synthesis are delineated in paragraph 6.5. The adsorption of the educts into the pore network of the silica support was followed by means of physisorption measurements (**Figure 4.5.2**), which highlighted an effective reduction of the pores volume due to the successful adsorption of the educts. As reference for a complete sequence of physisorption measurements (thus involving also the physisorption measurement after the thermal treatment), those registered for the YVT-01 sample (TiO_2 as support, (9 ± 2) nm pores size and Na_3VO_4 as vanadium educt) are reported in **Figure 4.5.9**, paragraph 4.5.2. In order to follow the steps of the synthesis, Raman measurements were performed on the untreated mesoporous silica, the dried silica adsorbed with the precursors and the impregnated silica after the thermal treatment.

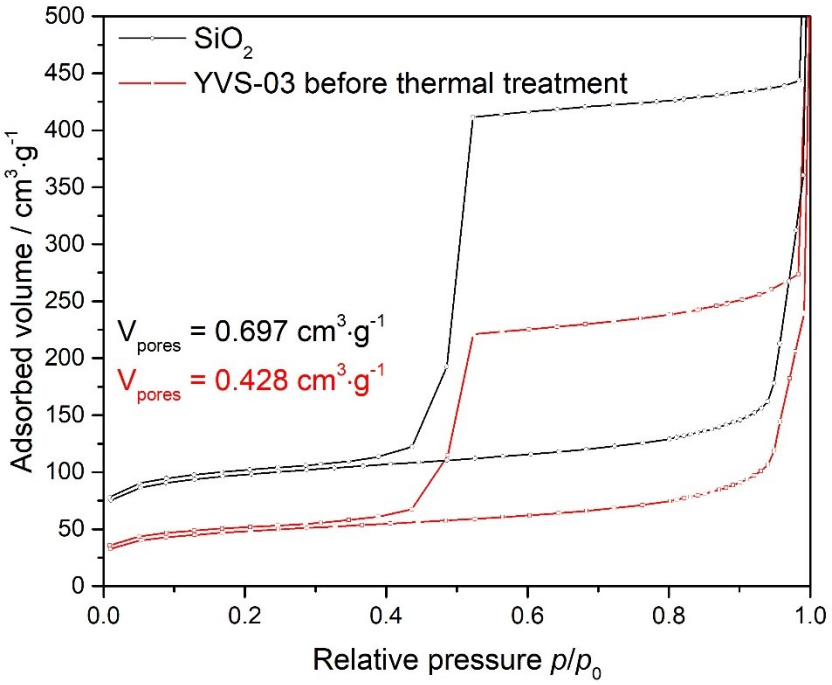

Figure 4.5.2: Physisorption measurements for the reference sample.

As can be noted in **Figure 4.5.3**, the Raman measurements of the two initial cases do not highlight the presence of any signal related to the presence of YVO_4 particles (in the region between 160 – 1000 cm^{-1}), nor to other polyoxovanadate species. On the other hand, after the thermal treatment at 600 °C for 2 h was performed on the adsorbed silica, the Raman spectrum highlighted the presence of the tetragonal zircon-type structure signals attributable to the yttrium vanadate (cfr. section 4.2). However, there are some signals not related to the YVO_4 tetragonal phase, that are the signals at 117, 633 and 715 cm^{-1}. Most probably these signals belong to a vanadium oxide species formed during the

annealing process,[111] but unfortunately the exact assignation could not be done due to the possible superimposition of these other signals with those of the yttrium vanadate tetragonal phase. Moreover, if vanadium oxide species were present, also yttrium oxide signals should be detectable, since, according to the YVO_4 stoichiometry, an equal amount of the two atoms was adsorbed in the mesoporous support, but no signal attributable to the yttrium oxide phase (in the range between 100 and 600 cm^{-1} could be noted from Raman measurements.[112] However, the possibility that these signals arise from some interactions between the product particles and the metal oxide support, due to the fact that the product particles are adsorbed onto the support surface, cannot be excluded. On the other hand, the possible presence of unreacted oxides, either of vanadium or yttrium therefore derived from their thermal decomposition, could therefore hint at an uncompleted reaction, thus suggesting that longer reaction times or higher temperatures would be needed for the reaction to complete.

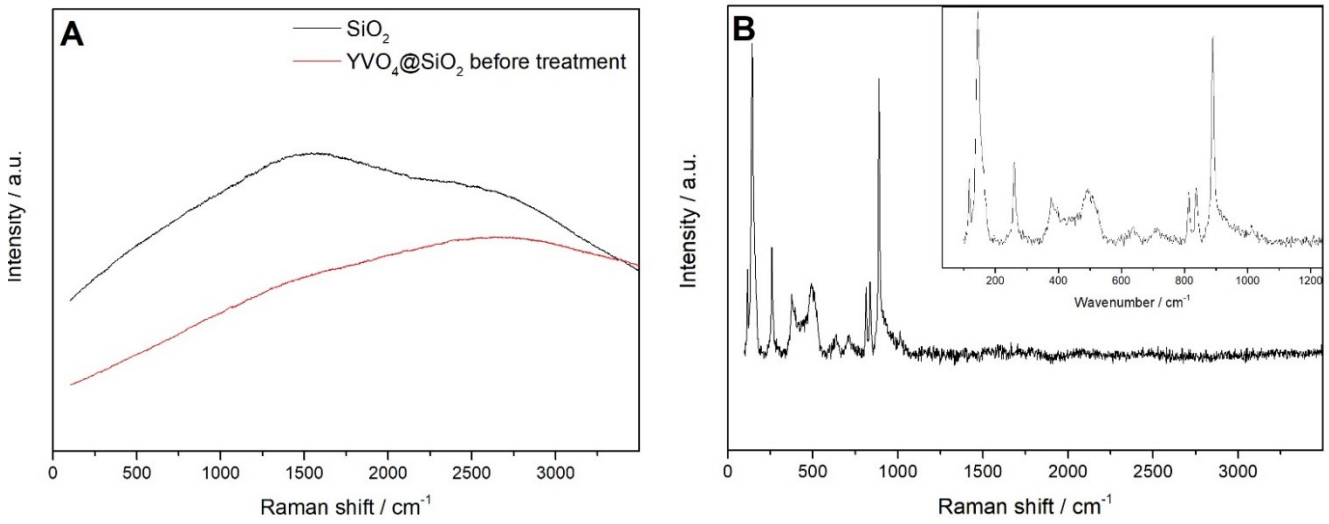

Figure 4.5.3: Raman measurements of the reference sample before the thermal treatment (A) and after (B).

The Raman measurements confirmed the presence of yttrium vanadate in the final product, but this measurement does not provide any information regarding how and where in the matrix the particles formed. For this purpose, TEM measurements were performed on the sample, in order to check where the particles formed, and if the mesoporous silica had maintained its porous structure even if exposed to high temperatures, which could cause the collapse of the porous structure. In Figure 4.5.4, TEM images of the reference sample are reported. Since TEM measurements relies on the transmitted electrons, atoms with higher atomic number possess a higher shielding effect towards the electrons and therefore resulted darker in the TEM image. In the case reported in Figure 4.5.4 the presence of darker particles as compared to the silica support is clearly visible (an example is highlighted with a red circle in the left image). The morphology of these particles is spherical, and by analysing the images with the software ImageJ, a mean diameter of (18 ± 2) nm was determined. The obtained particles are therefore very small, and they are single particles, not aggregated. Noticeably, the effect of the confined space is

evident, with the particles being smaller than the pore size distribution of the support, and the fact that the rigid confined space offered by the mesoporous supports prevented the aggregation of the particles. From the images it can also be noted that the porous structure of the silica is mostly maintained, apart for the external regions of the silica particles, which could be collapsed. The absence of porosity in these regions could arise from the soft-templated sol-gel synthesis itself, which involves some non-porous regions at the boundary of the particles where the surfactant micelles could not form, confirming that the porous structure of the support was still present even after the high temperatures involved during the thermal treatment.

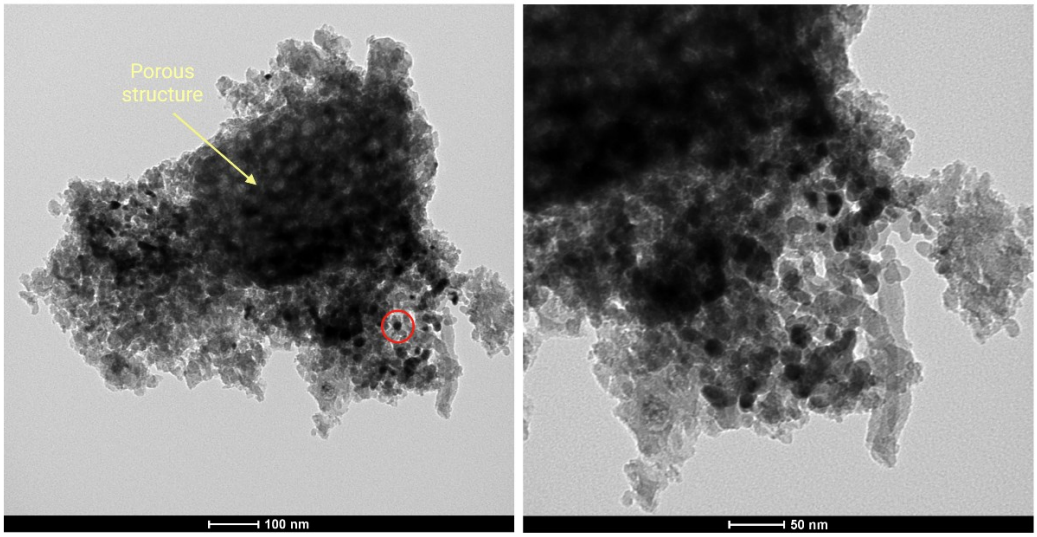

Figure 4.5.4: TEM images of the reference sample. An yttrium vanadate particle is highlighted with a red circle.

To further confirm the presence of YVO_4 particles inside the pore structure of the amorphous silica, TEM images were taken with a higher resolution instrument, with also SAED measurements and EDX mapping. The magnifications provided with the new TEM images allowed to recognise the crystallographic planes of the crystalline particles. This granted the possibility to distinguish between amorphous and crystalline zones in the TEM images, most likely related to the silica and YVO_4 particles, respectively. As showed in Figure 4.5.5, also in this case the porous structure is still distinguishable by the image on the left, while higher magnification of the particles was possible, as noted in the figure on the right. Being able to distinguish the crystallographic planes, it could be possible to obtain a Fourier transform of the planes, obtaining the reflections in the reciprocal space, which could be compared to the literature values to confirm the presence of a particular phase, since it is comparable to a XRD measurement specified for the particular planes visible in the image (Figure 4.5.6). In the specific case reported in Figure 4.5.6, the two reflections are associated with a constructive interference of the X-rays involving planes with interplanar distances of 0.35 and 0.18 nm respectively. Comparing these two reflections with the tabulated values, it appears that those reflections correspond to the reflections at 25.00° and 49.82° 2θ, associated with the (200) and the (312) planes respectively.[113]

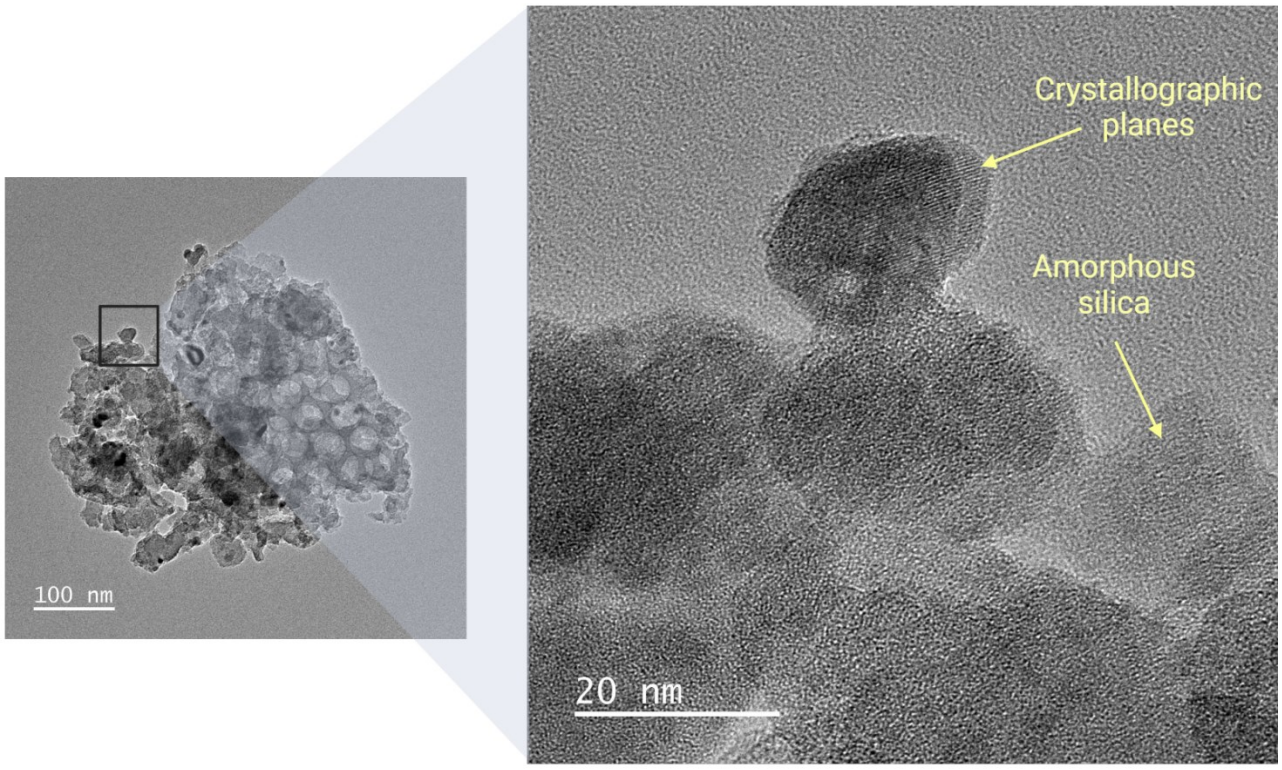

Figure 4.5.5: TEM images of the reference sample. On the left figure, the crystallographic planes of the crystalline particles are detectable.

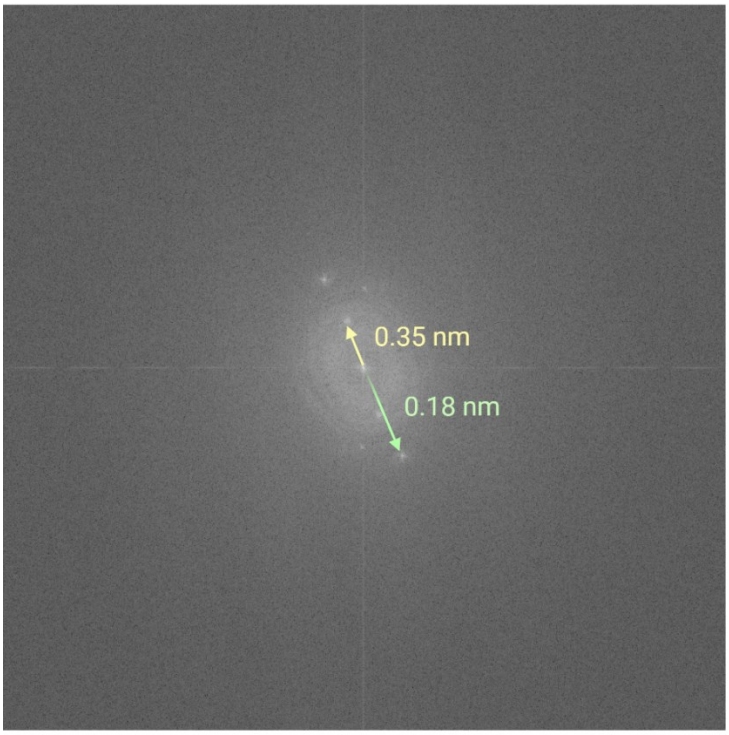

Figure 4.5.6: FFT of the particle highlighted in the right image of Figure 4.5.4.

To further confirm that the crystalline particles noted in Figure 4.5.5 were actually yttrium vanadate, SAED measurements, as well as EDX mapping were performed on the sample. From SAED measurements (Figure 4.5.7), the rings were associated with the interplanar spacings of 0.115, 0.150, 0.220 and 0.275 nm, which are associated with the reflections at 84.04°, 62.70°, 40.60° and 33.56° 2θ respectively and the respective planes are (611), (332), (301) and (112) of tetragonal structure of YVO_4.[113] The quite low intensity of the rings is due to the small dimensions of the particles and the presence of a large quantity of silica, which is amorphous.

As regards EDX mapping, Figure 4.5.8 highlights that in the analysed particles there is the presence of both yttrium and vanadium, thus eliminating the even labile possibility that the previous analysis (TEM images and SAED) could be referred to a species such as yttrium or vanadium oxide. Moreover, EDX measurements underlined the presence of an equal amount of yttrium and vanadium in the particles, accounting for the 1:1 expected atomic ratio for the YVO_4 particles.

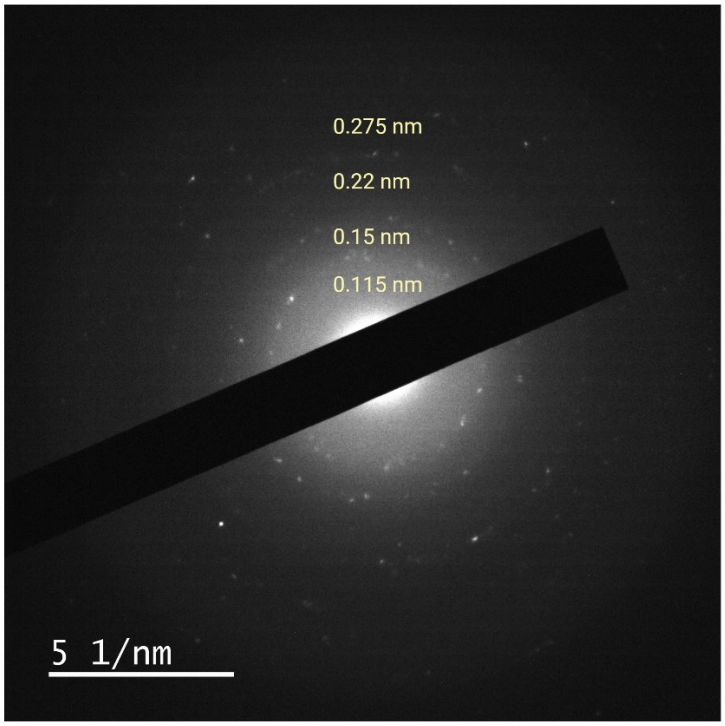

Figure 4.5.7: SAED measurement of the reference sample.

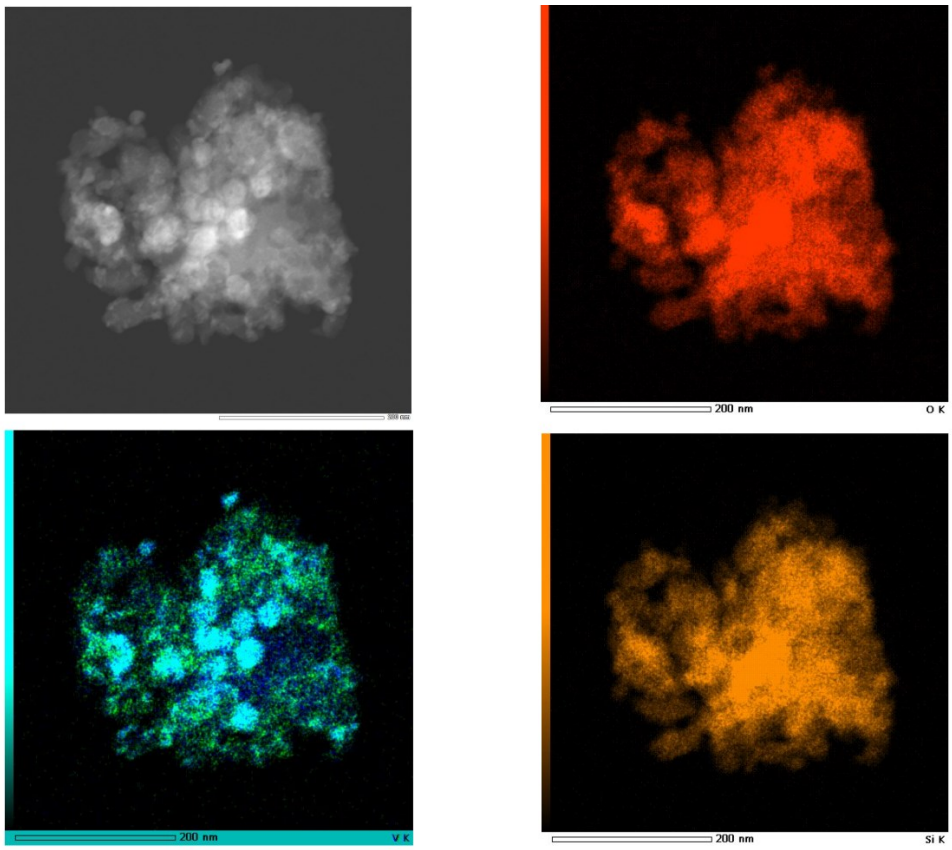

Figure 4.5.8: STEM-EDX measurements of the reference sample. Elements: O (red), Y (blu), V (green) and Si (orange).

As it can be noted in Figure 4.5.8, yttrium and vanadium are concentrated in spherical regions of dimensions of roughly 30 nm, accounting for the formation of the YVO_4 nanoparticles inside the pores. However, the presence of yttrium and vanadium also throughout the structure may hint either at the need of a longer reaction time or higher temperature to favour the completeness of the reaction, or at the fact that the reaction between the educts occurs only inside the pores, and not in other regions of the support (such as the channels between the pores or the external surface).

4.5.2 Variation of the reaction conditions

In this section, the variation of the reaction conditions and their effect on the product properties are discussed. In detail, the varied reaction conditions were: i) the exploited mesoporous metal oxide as support, ii) the vanadium precursor, changed between Na_3VO_4 and NH_4VO_3, and iii) the pores size distribution of the metal oxide.

Variation of the mesoporous metal oxide. The different metal oxides were tested in order to assess which could be the differences ascribed not only to their different chemical composition and the respective

value of the isoelectric pH (the pH value at which the total surface charge of the material is zero), but also the differences brought by their different pore networks (different pore networks may lead to different adsorption profiles of the educts and thus different outcomes of the reaction). Thus, different synthesis exploiting the same reaction conditions except for the metal oxide exploited as support were performed, and the differences observed are herein discussed. As regards the investigation of the different synthesis steps by means of physisorption measurements, a typical trend of the measured isotherms is reported in **Figure 4.5.9** (for mesoporous TiO_2, pores size distribution = (9 ± 2) nm), in which it can be noted that an initial reduction of the pore volume is associated with the adsorption of the precursors, and then, after the thermal treatment, an increase in the pore volume is detected. However the pores volume maintained lower than the initial value (that of the untreated titania), accounting for an effective presence of adsorbed species in the pore network. This last increase is probably associated with the evaporation of NO_x species due to the presence of nitrates and/or ammonium (which could also evaporate as NH_3) because of the adsorbed precursors. Unfortunately, no complete isotherms sequence regarding the reaction involving the silica as support is available, due to instrument issues.

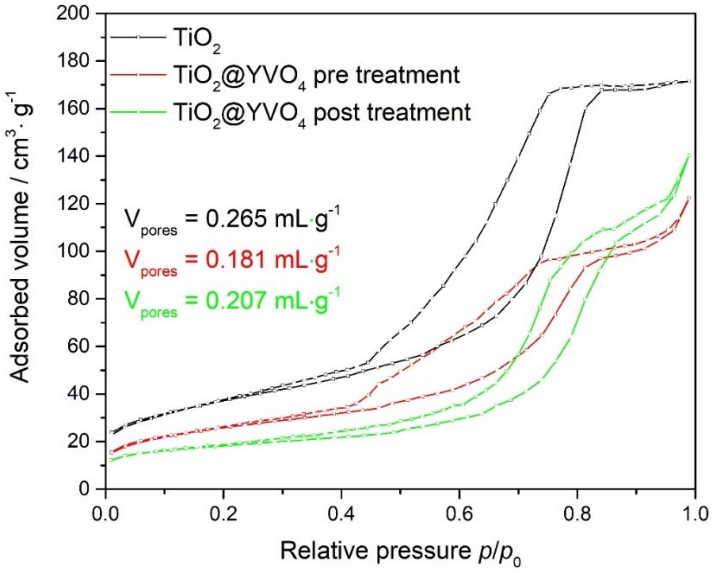

Figure 4.5.9: Physisorption measurements of the YVT-01 sample at different stages during the synthesis.

During the Thesis work, it was not possible to measure the isotherms of the other samples.

As regards the Raman measurements, those involving the silica as support are similar to those reported in **Figure 4.5.3** for the reference sample and are reported in **Appendix A.2**, **Figure 9.2.1**. On the other hand, Raman measurements performed on samples obtained exploiting either zirconia or titania as supports are quite different from those involving the silica. Raman measurements on samples obtained exploiting mesoporous titania as support revealed the presence of the anatase phase of the titania,[114] but after the thermal treatment no further signals are detectable (**Figure 4.5.10**). This is probably due to the very different amount of titania and yttrium vanadate, which could cause the signals of the former to totally overlap with those of the latter, as they are in the same region of the Raman spectrum.

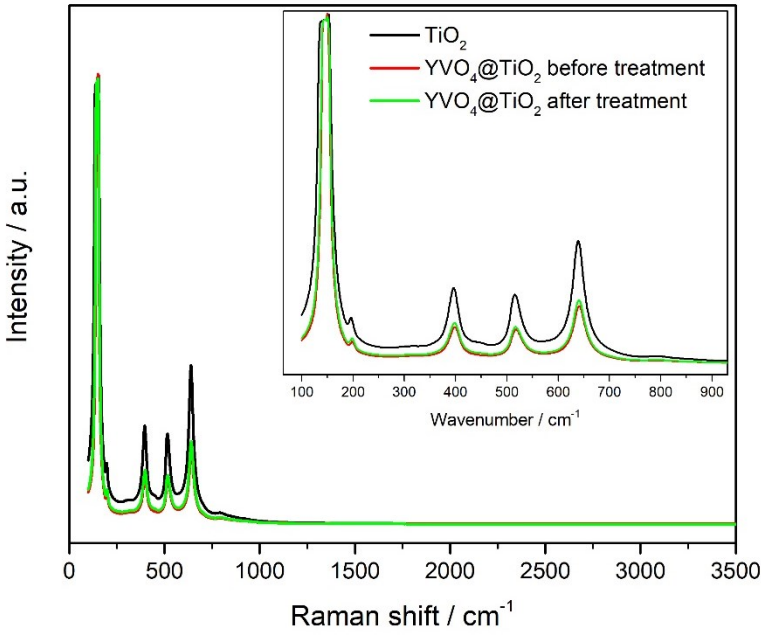

Figure 4.5.10: Raman spectra of the YVT-01 sample at different steps of the synthesis.

As regards the samples obtained exploiting zirconia as support, the Raman spectra of the samples before the thermal treatment do not highlight the presence of the zircon-type structure of the YVO_4, but most importantly, they do not show the presence of the typical zirconia structure either. However, as can be noted in Figure 4.5.11, after the thermal treatment (600 °C, 2 h), the signals of the zirconia (tetragonal phase with weak signals of the monoclinic phase) are clearly distinguishable, but similarly to the case of titania, no signal of the YVO_4 product is detectable. Moreover, the zirconia before the thermal treatment appeared to be of a black colour, while after the thermal treatment the colour turned white. This was probably due to the synthesis process of the zirconia itself, due to possible carbon residues[115] remaining on the zirconia after the calcination step needed to burn out the surfactant (1 h at 350 °C followed by 500 °C for 4 h) for obtaining the porous matrix. The presence of carbon could also explain why no signal of the zirconia could be detected in the first Raman spectra, since the carbon signal may be more intense than those of the zirconia. The Raman spectrum of YVO_4@ZrO_2 after thermal treatment highlighted the presence of mainly tetragonal zirconia, with weak signals related to the presence of monoclinic zirconia,[116] confirming the results obtained through XRD measurements in a previous work carried out at the JLU University in the working group of Prof. Dr. Bernd Smarsly. In the Raman spectrum after thermal treatment, the signal at 570 cm^{-1} could not be assigned to any chemical species, neither zirconia polymorphs nor yttrium vanadate. Therefore, it could be due to some impurities present in the sample.

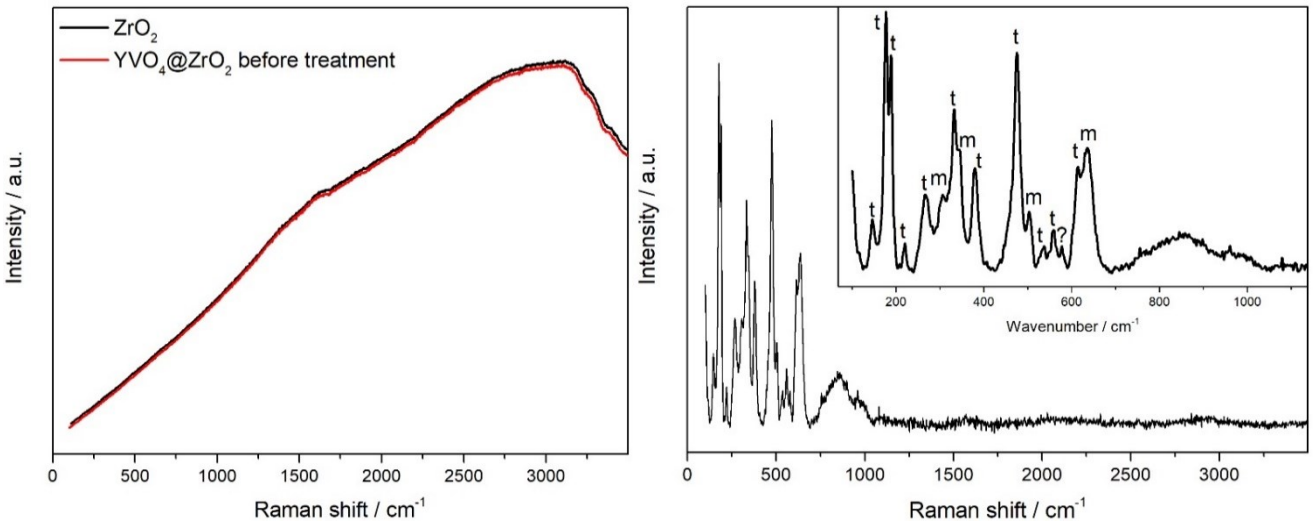

Figure 4.5.11: Raman spectra of the YVZ-01 sample (ZrO_2 as support, (44 ± 5) nm pores size, NH_4VO_3 as vanadium educt) at different stages of the synthesis. In the Raman spectrum of the sample after thermal treatment (right), the signals associated with either the tetragonal (*t*) or the monoclinic (*m*) zirconia are highlighted.

The fact that neither in the samples obtained exploiting the zirconia as support, nor those obtained with the titania as support, the signals of the yttrium vanadate structure were not detectable is probably to ascribe to the fact that these two supports present signals in the same region of the Raman spectrum (150 – 1000 cm^{-1}) as compared to the yttrium vanadate, and therefore a superimposition of the signals is to be expected. Moreover, these two supports presented a much lower pore volume as compared to the porous silica, therefore involving a smaller content of yttrium vanadate particles, which could result in less intense signals. The combination of the lower amount of product in the pores, the fact that these two supports are crystalline, and the possible superimposition of the signals made the determination of the presence of yttrium vanadate in the pores of these crystalline supports very difficult, if not impossible through techniques like the Raman spectroscopy.

For the previously mentioned reasons, TEM measurements of the different samples obtained by exploiting different mesoporous metal oxides as supports were taken. Figures 4.5.12 and 4.5.13 report the TEM images of the samples obtained exploiting zirconia [(23 ± 4) nm] and titania [(38 ± 7) nm] as supports respectively. As can be noted, the porous pattern of the supports is not detectable, even if physisorption measurements reported in Figure 4.5.9 highlighted that the porous nature of the supports is still present after thermal treatment. This could probably be due to the low voltage of the exploited instrument which cannot penetrate properly in atoms denser than the silicon ones, as is the case for titanium and mostly for zirconium. For these samples, higher resolution TEM images, as well as STEM-EDX mapping could be helpful to evaluate the effective presence of yttrium vanadate particles inside the pores. However, SAED measurements would probably not be helpful due to the high presence of crystalline support with respect to the crystalline product, which could cause the signals of the supports to overlap with the signals of the product.

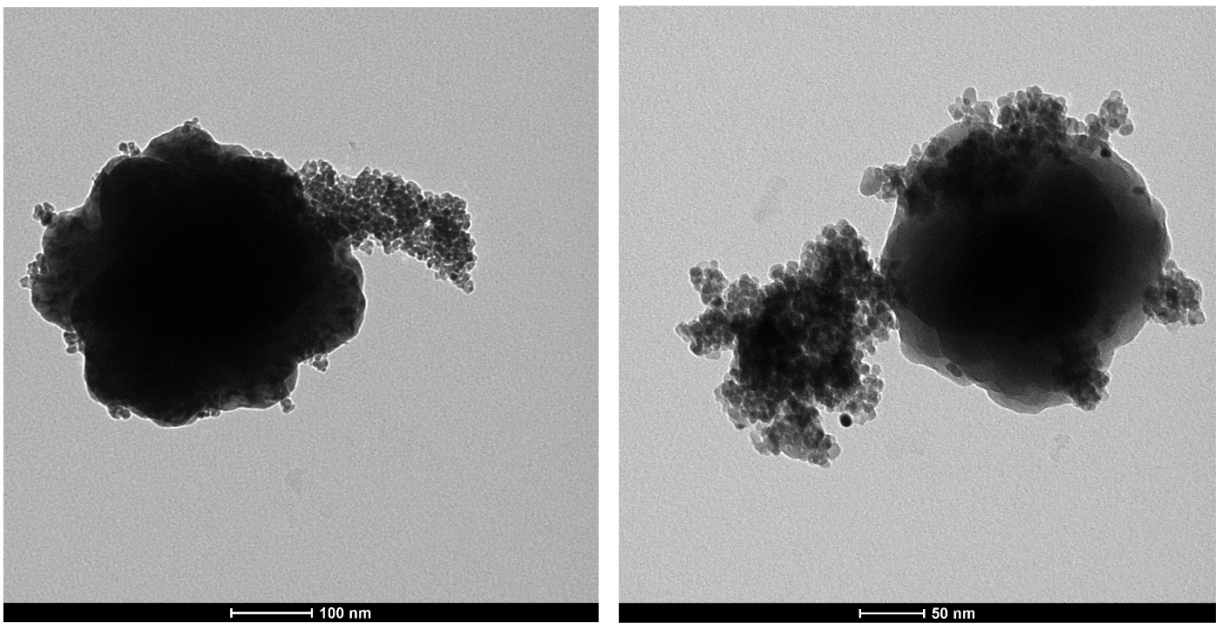

Figure 4.5.12: TEM images of the sample obtained exploiting ZrO_2 as support, (44 ± 5) nm pores size, NH_4VO_3 as vanadium educt.

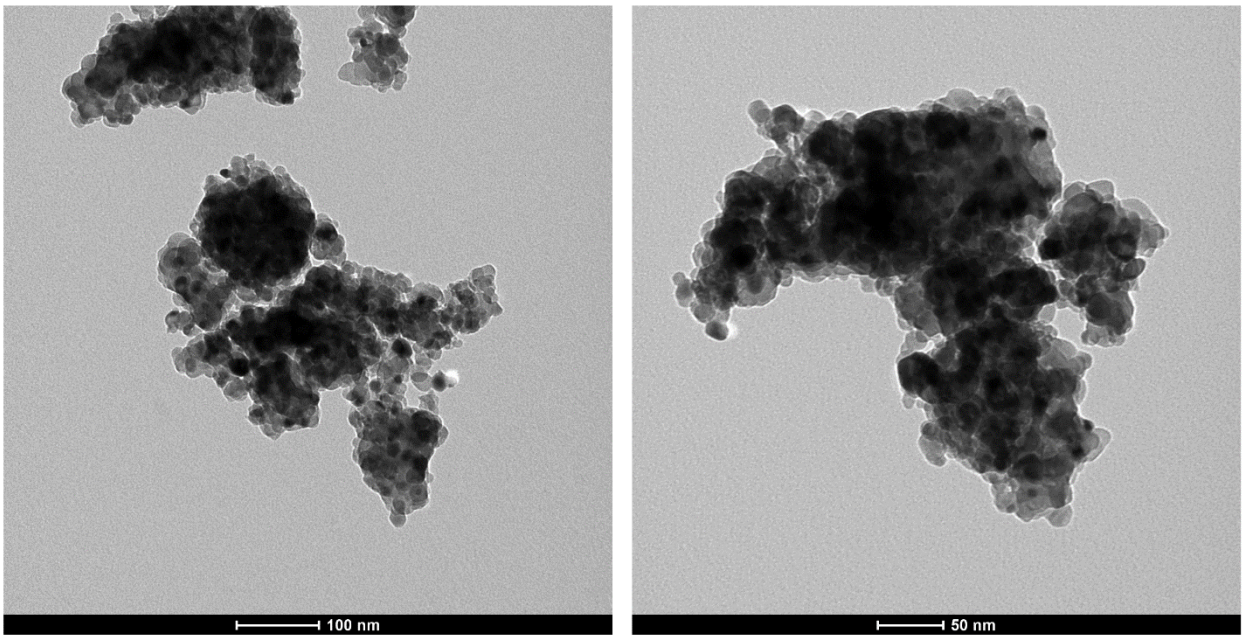

Figure 4.5.13: TEM images of the sample obtained exploiting TiO_2 as support, (38 ± 7) nm pores size, NH_4VO_3 as vanadium educt.

As can be noted from the two figures, these two samples – both obtained with the same reaction conditions apart from the nature of the support – seem to present particles aggregated upon a denser bigger particle (darker colour). The smaller particles could be particles of the supports, since their amount is too large to be product particles, but in order to surely state this, EDX measurements would be required.

Variation of the vanadium precursor. As already mentioned, two different vanadium precursors were tested, that is Na_3VO_4 and NH_4VO_3. As regards the sample obtained with the latter vanadium precursor, an extended discussion was already provided for the reference sample. Within this paragraph, the sample obtained exploiting SiO_2 as support, (73 ± 10) nm pores size and Na_3VO_4 as vanadium educt (YVS-01) is discussed. The mentioned sample was obtained exploiting Na_3VO_4 as precursor, and silica with pore size distribution of (73 ± 10) nm as support. Raman spectra measured at different steps during the synthesis were similar to those measured for the reference sample. One difference is notable in the Raman spectra after the thermal treatment (**Figure 4.5.14**). Indeed, in this case there is only one signal not attributable to the YVO_4 zircon-type phase, which is the signal at 636 cm^{-1}, as opposed to the two different signals present for the reference sample. The possible explanations for this signal are similar to those drawn for the reference sample, that is either the presence of by-products or the presence of particular interactions between the product particles and the silica support.

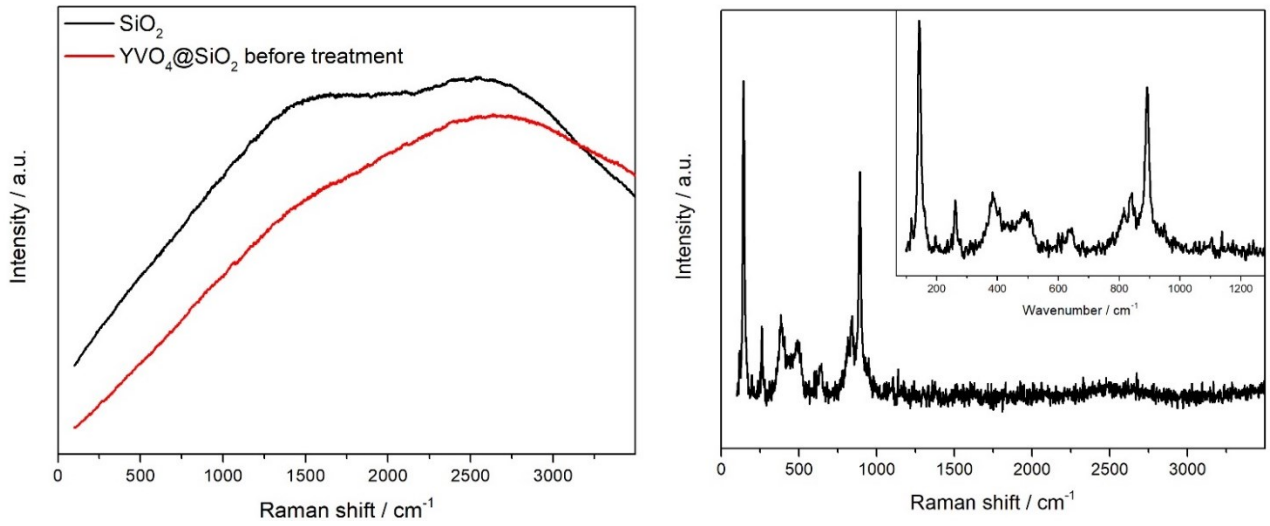

Figure 4.5.14: Raman spectra of the sample obtained exploiting SiO_2 as support, (73 ± 10) nm pores size, Na_3VO_4 as vanadium educt at different steps during the synthesis. The Raman spectrum of the sample after thermal treatment is reported in the image on the right.

However, the main difference between the two different samples could be defined by TEM and STEM-EDX measurements. In the case of sample obtained with the orthovanadate as precursor, the crystalline particles possess so small size, that only the measurements with a higher resolution TEM could detect their presence. In **Figure 4.5.15**, an example of particle is reported (highlighted as red circle), and its very small size can be appreciated, being smaller than 10 nm (the exact estimation is not possible due to the superimposition with the silica support). Also in this case, the crystallographic planes are distinguishable, as opposed to the amorphous silica. The Fourier transform of the crystallographic planes highlighted two specular reflections in the reciprocal space (**Figure 4.5.16**), due to planes with interplanar distance of 0.33 nm, associated with the reflection at 25.00° 2θ in the powder diffraction pattern of tetragonal YVO_4, related to the planes indexed as (200).

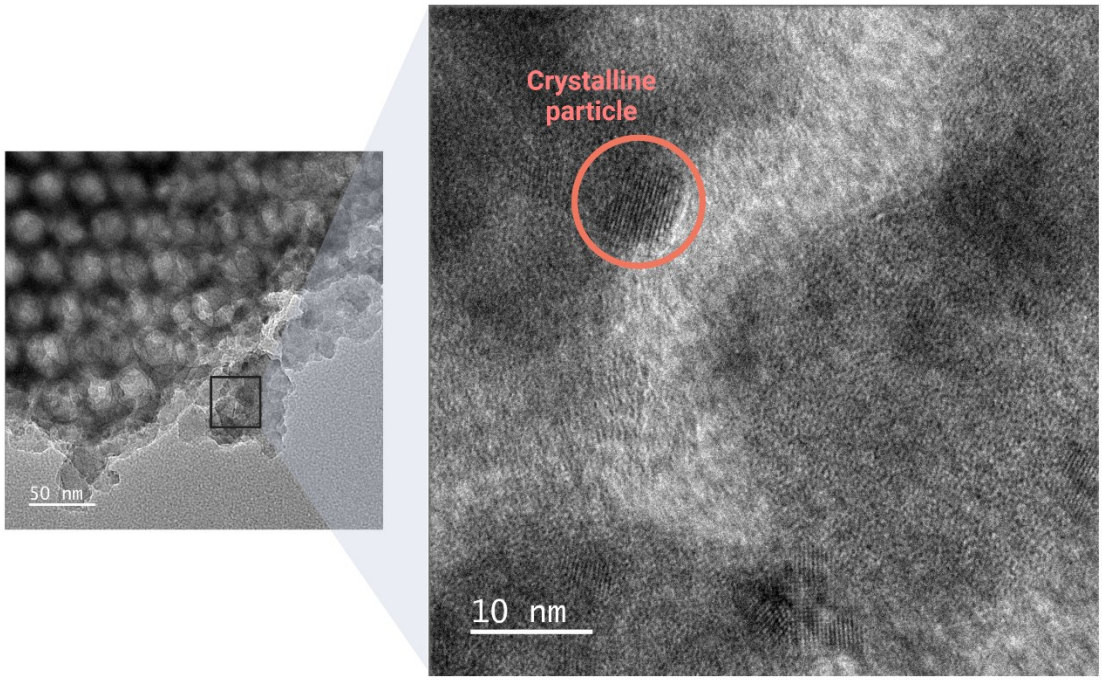

Figure 4.5.15: TEM images of the sample obtained exploiting SiO_2 as support, (73 ± 10) nm pores size and Na_3VO_4 as vanadium educt.

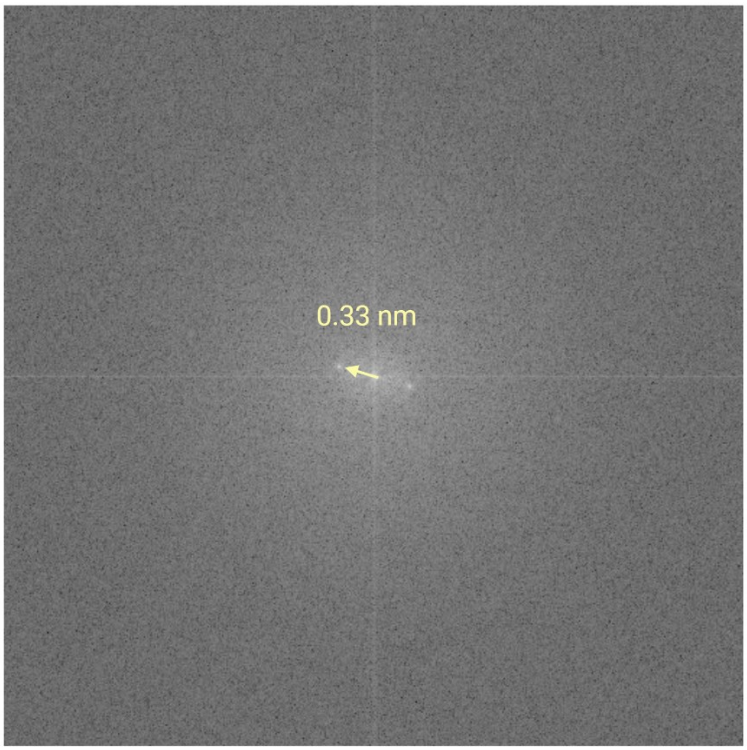

Figure 4.5.16: FFT of the particle highlighted in the right image of Figure 4.5.12.

However, for this sample the particles were too small to perform SAED measurement, resulting in just amorphous signal. On the other hand, STEM-EDX measurements revealed that yttrium and vanadium are equally distributed throughout the structure. This is probably due to the presence of very small

particles combined with the larger pores of the structure: the small particles might be actually confined in the pores, but the number of the particles might be so high that an apparent uniform distribution is found. Moreover, the pores of the support were initially of (73 ± 10) nm, but by the TEM measurements, a rough estimation of 55 nm as pore size was found. Probably, larger pores are more susceptible to the high temperatures, causing a shrinkage of the pores which could have caused the incorporation of forming particles inside the structure. However, from EDX mapping (Figure 4.5.17) it appeared that even the particles formed on the surface possessed small dimensions, thus the cause of these small dimensions may be attributed to the different precursor. A possible explanation is that with the NH_4VO_3 precursor, the ammonium degraded at high temperatures, allowing the presence of only Y(III) and VO_3^- inside the pores, thus probably favouring the interaction, and therefore the reaction, between the reagents. With the Na_3VO_4 precursor this reasoning does not apply, with the Na^+ ion remaining in the pore network, thus probably hindering the reaction between the reagents. That is, the presence of the sodium ions in the support may slow down the reaction between the reagents due to the fact that the vanadium counterion does not degrade (as in the case of the metavanadate precursor), making the vanadium educt less reactive towards the yttrium one. A further explanation may be that the residual sodium ions in the porous support are embedded in the crystal growth of yttrium vanadate, thus hindering the growth of the crystal itself. Indeed, the principles of recrystallisation state that the presence of impurities during the formation of the crystal may hinder the crystallisation process.

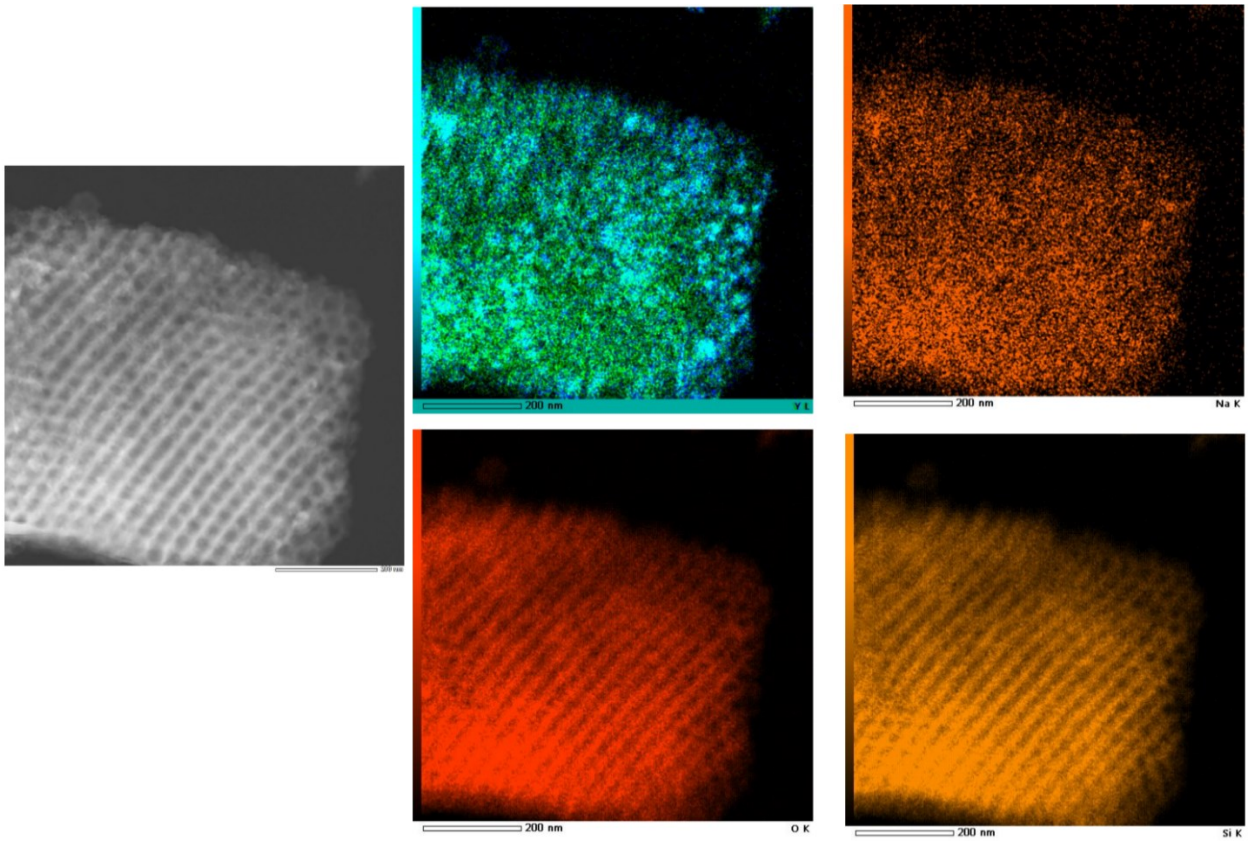

Figure 4.5.17: STEM-EDX measurements of the sample obtained exploiting SiO_2 as support, (73 ± 10) nm pores size and Na_3VO_4 as vanadium educt. Elements: O (red), Y (blu), V (green), Si (light orange) and sodium (dark orange).

Also in this case, as compared to the reference sample, it can be noted by **Figure 4.5.17** how the YVO_4 particles (light blue colour) are mostly confined in the pores, as can be noted by the presence of spherical light blue regions which are superimposable with the pores highlighted in figure on the left. However, as stated above, the particles are so small that an apparent homogeneous distribution of the two elements can be noted. Moreover, in this sample there is a higher content of unreacted Y and V (the separated blue and green colours in the EDX mapping) with respect to YVO_4 particles (cfr. **Figure 4.5.8**, where a major presence of light blue regions was detectable), probably due to the presence of Na^+ as counterion, as hypothesised above.

Variation of the pores size distribution. As regards this last experimental variable, no proper measurements could be performed due to lack of time. The only measurement possible was the Raman spectroscopy, which however gave similar results to those previously discussed within this paragraph, and are therefore reported in the **Appendix A.2**, **Figure 9.2.1**. The only difference was found for the sample obtained exploiting porous silica with pore size distribution of (73 ± 10) nm and NH_4VO_3 as vanadium precursor (YVS-04). In this case, the Raman spectrum highlighted the absence of the signals attributable to the zircon-type structure of the YVO_4 (**Figure 4.5.18**), very different as compared to the reference sample for which the formation of YVO_4 particles inside the pores was thoroughly determined, but further analysis would be required to understand the role of the pore size distribution in the outcome of the reaction.

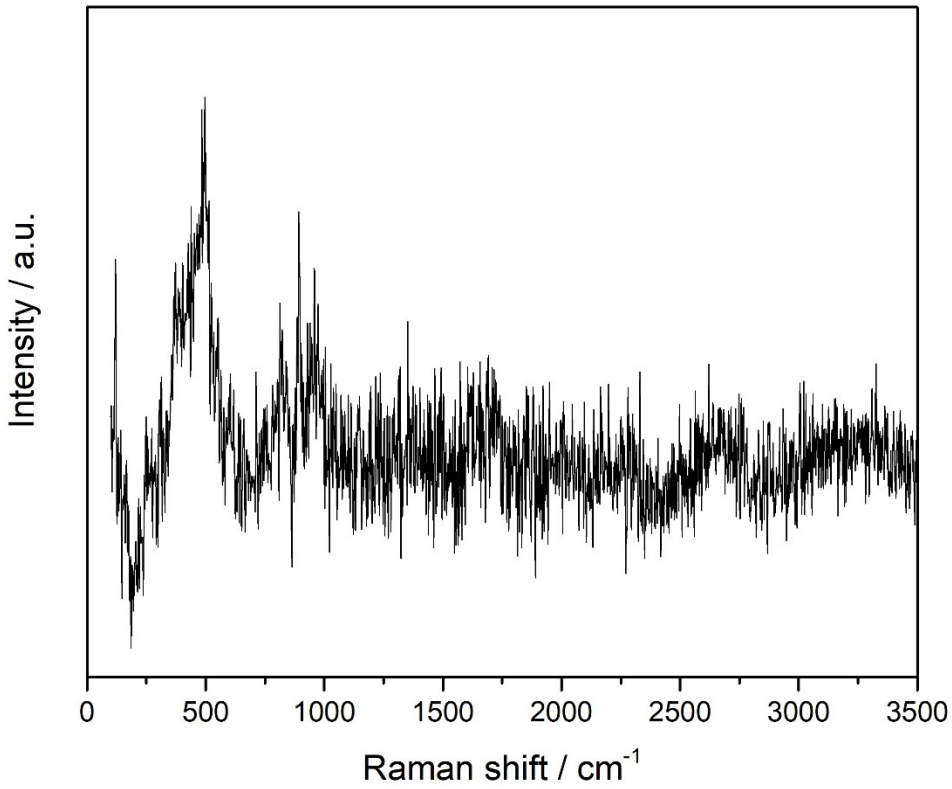

Figure 4.5.18: Raman spectrum of the sample obtained exploiting SiO_2 as support, (73 ± 10) nm pores size and NH_4VO_3 as vanadium educt.

In conclusion, as far as the limited analysis allowed to understand, exploiting silica as support allows for an easier measure of the product properties, since the light Si atoms combined with the amorphous nature of the silica involve a good contrast with the yttrium vanadate particles both in the Raman spectroscopy and in microscopy measurements. However, deeper analysis on the effects of zirconia and titania as supports are needed. As regards the reference sample, it can be inferred that a solid state reaction between the adsorbed precursors was performed, at lower temperatures as compared to classical solid-state reaction carried out through annealing synthesis.[117] Moreover, generally the thermal synthesis of metal oxides inorganic species leads to the formation of large particles, but in our case, the confinement of the reaction within the pores of a mesoporous support led to the obtaining of small nanoparticles, with size comparable to that of the pores (in the case of NH_4VO_3 as vanadium educt, cfr. reference sample discussed above). Thus, an effective space confinement provided by the mesoporous matrix for the solid-state synthesis of inorganic nanoparticles can be highlighted.

5 CHARACTERISATION TECHNIQUES

In this chapter, the characterisation techniques exploited during the experimental work of the thesis are presented and described. A special emphasis is given to particularly important techniques for the thesis, that is the X-ray diffraction and physisorption analysis.

5.1 Physisorption

Physisorption (physical adsorption) is a widely used method to characterize the structural features of micro- and mesoporous materials.[118,119] The term physisorption[5] refers to the adsorption of a gas (adsorbate) on a solid (adsorbent),[120] due to van der Waals forces between the two of them. The counterpart of adsorption is the desorption, in which the amount of adsorbed gas continuously decreases. Adsorption data are usually recorded in terms of the adsorbed amount as a function of pressure of the adsorptive at a constant temperature, thus leading to a so-called isotherm. For subcritical isotherms, the data are reported as a function of p/p_0, where p_0 is the saturation pressure of the bulk fluid.[120] When the two processes of adsorption and desorption do not coincide, depending on the pore size, a hysteresis loop is obtained.[121]

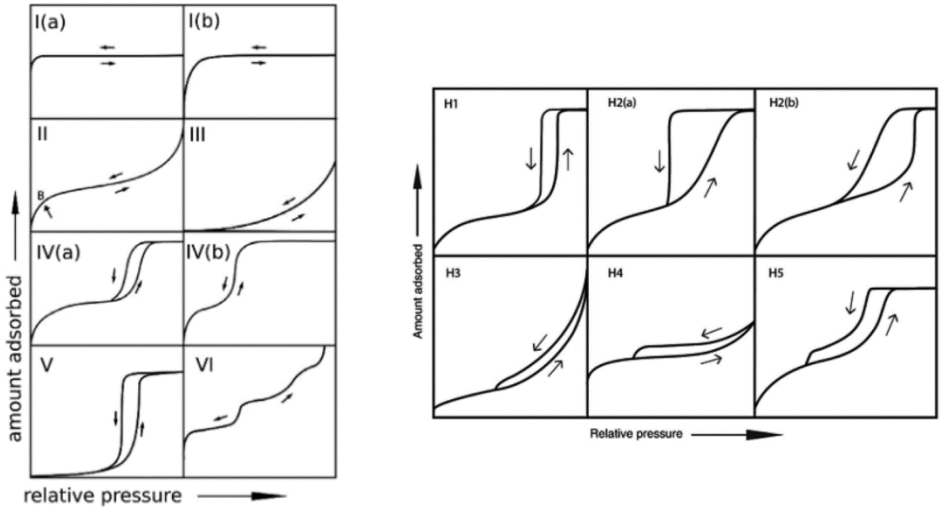

Figure 5.1.1: : Characteristic types of isotherms (left), and typical hysteresis loops (right).[119]

The shape of these isotherms depends on the strength of the interaction of the type fluid-solid and fluid-fluid, therefore on the chosen gas for the experiment, and depends on the adsorbent's pore structure.[120] Therefore, information on the porous material structure can be obtained by analyzing the isotherm's shape. Based on that, IUPAC established a classification of typical isotherms and hysteresis loops that can be observed, as denoted in Figure 5.2.1.[121] In order to be able to analyze the physisorption data, the physical processes that intervene have to be understood. First of all, micro- and mesopore filling differ

substantially, since the former fill out at low relative pressures (p/p_0 < 0.15) and is solely due to the enhanced fluid-solid interactions in the micropores.[118] On the other hand, mesopores fill through pore condensation, i.e., gas-liquid phase transition that occurs at a pressure lower than the saturation pressure of the bulk fluid. This process depends not only on the fluid-solid interactions, but also on the fluid-fluid ones, and is often accompanied by hysteresis loops.[118] Hysteresis occurs when pore width exceeds a certain critical width, which depends on the chosen adsorptive and temperature. Both for nitrogen at 77 K and argon at 87 K, the critical pore width is 4 nm.[120] Hysteresis are associated with pore condensation, and arise from adsorption metastability and pore network effects, which can alter the shape of the hysteresis loop. A complete and detailed analysis of the different types of isotherms, loops, and their origin is provided by the IUPAC technical report.[121]

The surface of a solid can be divided into three different layers, showed in Figure 5.2.2: the van der Waals surface, made up of the van der Waals spheres of the atoms on the surface of the solid; the Connolly surface, defined as the surface drawn by the bottom of a spherical probe molecule rolling over the van der Waals surface,[121] which is the surface assessed with the physisorption measurement; and finally, the *r*-distance surface, located at distance *r* from the Connolly surface.

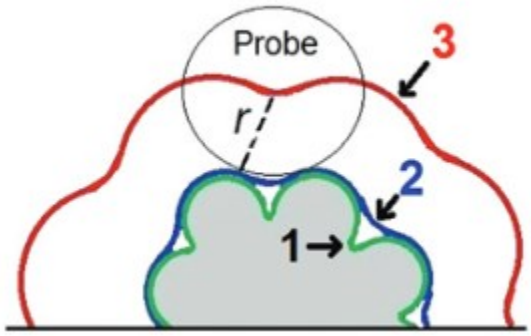

Figure 5.1.2: the three different surfaces of a solid. Van der Waals (1), Connolly (2), and *r*-distance (3).[21]

Since the determined surface is not the real one of the solid, the choice of the correct adsorptive is of fundamental importance. First of all, the accessibility of pores to adsorptive molecules depends on the dimensions of the latter, therefore the recorded value of surface area and pore volume may vary with different adsorptives.[121] Moreover, different molecules may interact differently with the surface atoms of the solid. For example, nitrogen molecules possess a quadrupole moment that can cause interactions with polar surface groups of the solid, leading for example to a preferred orientation of the nitrogen molecules that can bring to errors in the surface estimation.[120] For this reason, argon adsorption an 87 K is recommended by IUPAC for pore size analysis, since argon does not present the quadrupole moment and therefore does not interact with polar surface groups. Moreover, argon is composed of spherical atoms, which therefore possess a clear cross-section, allowing for more accurate measurements compared to nitrogen.

For the assessment of the surface area of a solid, the most widely used method is the Brunauer-Emmett-Teller (BET) method. This method is limited to the evaluation of the surface of solids that give rise to a Type II or Type IV isotherm,[120,121] and the so estimated surface is referred to as the probe accessible

surface. This method exploits the monolayer formation in the mesopores, therefore assuming that no multiple-layer is present in the sample and that all the adsorptive molecules are adsorbed directly to the solid surface. By knowing the cross-sectional area of the adsorbate, i.e., the average area occupied by a single adsorptive molecule in the complete monolayer,[121] and how much of it has been adsorbed to the solid surface, one can obtain the value of the surface area. More in detail, the isotherm is transformed into the 'BET plot', usually in the linear form, **Equation 5.1**,[120] and from that, the monolayer capacity n_m is calculated.

$$\frac{\frac{p}{p_0}}{n(1-\frac{p}{p_0})} = \frac{1}{n_m C} + \frac{C-1}{n_m C}(\frac{p}{p_0}) \qquad \textbf{5.1}$$

Where p is the equilibrium pressure, p_0 is the saturation pressure of the bulk fluid at the selected temperature, n is the amount of adsorbate, nm is the monolayer capacity and C is a constant related to the energy of monolayer adsorption. Linear BET plot is usually found in the range of relative pressure p/p_0 = 0.05 – 0.3. In general, the range of the BET plot is determined by its maximum, and the constant C has to be positive in order to be of physical meaning. Once the monolayer capacity is assessed, the surface area can be calculated according to **Equation 5.2**.[120]

$$S = n_m N_a \sigma \qquad \textbf{5.2}$$

Where N_a is the Avogadro number and σ is the cross-sectional area of the adsorbate molecules. Anyway, care has to be taken since no pore condensation has to be present in the chosen range of pressure, and finally a remark that the BET surface area is an estimation of a probe accessible surface area.

On the other hand, the region associated with mesopores filling by multilayer adsorption and pore condensation is used to assess the pore size and size distribution. The multilayer forms an adsorbed film, which has the same properties as the bulk liquid.[120] When the film reaches a critical thickness, pore condensation occurs. This phenomenon can be described by the modified Kelvin equation, which connects the pore size to the critical film thickness and to the pressure at which pore filling occurs for the given pore size, as shown in **Equation 5.3** (for cylindrical pores).[120]

$$ln(\frac{p}{p_0}) = -\frac{2cos(\theta)}{RT\Delta\rho(r_p - t_c)} \qquad \textbf{5.3}$$

Where R is the universal gas constant, T is the temperature, r_p is the pore radius, t_c is the critical thickness and $\Delta\rho$ is the difference between the density of the liquid and that of the gas. Other thermodynamic, macroscopic theories have been developed in the past years, but all of them cannot describe the critical region of the confined fluid, i.e., the pore condensation and therefore the hysteresis. Therefore, microscopic approaches are based on statistical mechanics like the DFT.[120,121] Among them, NLDFT (non-local density function theory) exploits theoretical kernels (set of isotherms) obtained by fixing the adsorbent, adsorbate, pore morphology, temperature, and pore size. Since the only variable is the pore size, all the obtained kernels are combined in order to fit well the experimental isotherm. From this combination, the pore size distribution can be extrapolated.

One last issue is associated with the assessment of pore network characteristics. Indeed, in complex pore networks various effects can modify the desorption branch. For example, if the pores are connected to the external surface only through small necks (ink-bottle pore shape), the pores remain filled with the fluid until the narrow necks empty at lower pressures. This phenomenon is called pore restriction and can be caused by two effects: either pore blocking or cavitation. The neck width determines which of the two effects is responsible for the pore restriction: below the critical neck width of 5 – 7 nm for nitrogen and argon at 77 and 87 K, respectively, cavitation occurs. Otherwise, pore emptying follows the pore blocking mechanism.[120] In pore blocking, the neck width is smaller than the pore size, therefore the pore remains filled with the fluid until the neck empties at lower pressures; still, the emptying pressure is a function of the neck width. On the other hand, when cavitation occurs, the neck width is smaller than the critical value; in this case, the evaporation is delayed to the point that the liquid in the pore becomes metastable and evaporates as soon as a bubble is formed. Therefore, the emptying pressure is not a function of the neck width. To establish which process is causing the pore restriction, two different approaches can be used: either the comparison of two adsorptives or a hysteresis scan. Remembering that cavitation is a thermodynamic effect while pore blocking is a function of the neck width, the two different processes can be distinguished. Changing the adsorptive, the desorption-branch-derived pore size distribution remains the same in case of pore blocking, since it is a function of the neck width. On the other hand, a dependence on the adsorptive is highlighted if cavitation is occurring, since it is a thermodynamic effect and therefore it depends on the chosen adsorptive. On the other hand, a hysteresis scan experiment can be carried out. In this measurement, a series of partial isotherms is recorded, which means that the pores are not completely filled before emptying. Since cavitation is thermodynamically driven, evaporation is not affected by neighboring pores, and the partial isotherms resemble the shape of the initial one. On the other hand, in pore blocking, the interactions between neighboring pores are crucial in the desorption mechanism.[120] Therefore, a series of different partial isotherms merging into the closure point is obtained. Figure 5.2.3 summarizes all these processes.

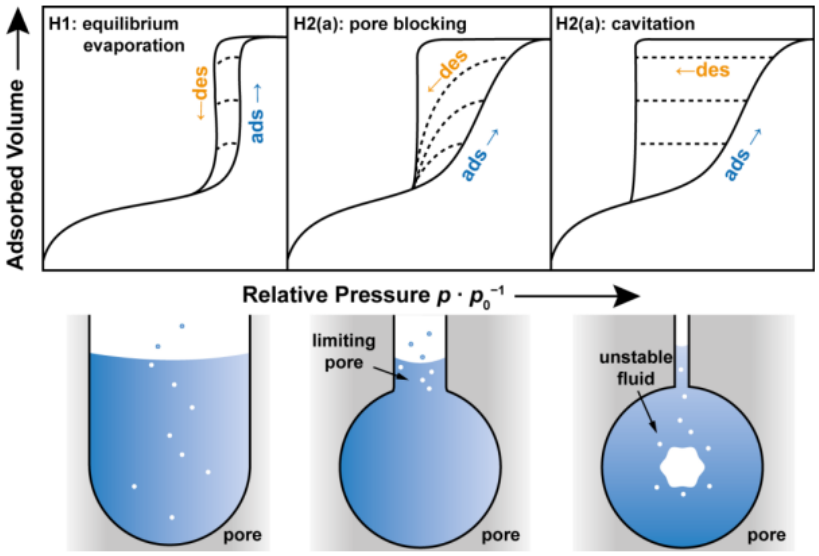

Figure 5.1.3: Different cases of evaporation in mesopores.[122]

As a final remark, when pore restriction is present, a reliable pore size distribution can be calculated only from the adsorption branch, even though it is a metastable and not an equilibrium branch. Finally, since pore blocking depends on the pore neck size and size distribution, information about those can be obtained by considering the desorption branch of the isotherm.[119–121] The measurements were taken with a *Quadrasorb evo* by Quantachrome instruments. The nitrogen physisorption experiments were performed at 77 K, and the data were evaluated with the aid of the software ASiQwin. The model used for the calculation was nitrogen at 77 K on silica, cylindrical pores, NLDFT, and adsorption branch. The samples were degassed at 200 °C for 6 h in order to remove attached gasses or water before the measurement.

5.2 PXRD

X-ray powder diffraction is a non-destructive technique for the analysis of the crystal structure and the mean crystallite size of crystalline powder materials. X-rays are used in this analytical technique because their wavelength is of the same order of magnitude as the interatomic distances in a crystal (10^{-9} m – 10^{-12} m). When the X-rays interact with the crystal, they are diffracted in all directions. The result of the interference between all the diffracted X-rays is a diffractogram. X-rays diffract constructively only when Bragg's law[123] (Equation 5.4) is satisfied, that is when the X-rays are all in phase.

$$n\lambda = 2dsin\theta \qquad \textbf{5.4}$$

Where λ is the wavelength of the radiation, θ is the angle between the incident beam and the crystalline plane and *d* is the distance between two crystalline planes with the same *hkl* indices. The atoms in a crystal structure can be seen as lying in planes, whose distance is the parameter *d* in Bragg's law. In a crystalline powder sample, the coherent scattering domains are oriented in all the possible directions, but only the diffracting planes which are orthogonal to the incident beam and satisfy the Bragg's law diffract the radiation, making the analysis reproducible. Differently from a single crystal XRD (which provides a 3D reflection pattern), the PXRD analysis gives only a 2D diffractogram as a function of the angle between the incident beam and the diffracting planes. The diffraction pattern obtained provides information about the phase identity, phase purity, mean crystallite dimensions and crystal strains of the sample. Indeed, every crystalline material has a specific arrangement of atoms in space, i.e., the crystal structure, which can be classified in a specific crystalline system, and which corresponds to a specific diffraction pattern. Because of that, the position of the reflections gives information about the crystalline system, and the distance between the planes. If more than one diffraction pattern is detectable for one sample, it means that the sample presents more than just one crystalline phase. On the other hand, the width of the diffraction peaks is related to the dimensions of the crystallites, which are the smallest coherent scattering domains in the particle.[124,125] This determination is possible by using Scherrer's equation,[126] which states that:

$$L = \frac{K\lambda}{\beta cos\theta} \qquad \textbf{5.5}$$

Where *L* is the mean crystallites size, *K* is the dimensionless Scherrer's constant related to the symmetry of the crystalline unit cell (0.9), β is the full width at half maximum (FWHM) of the reflection, θ is the Bragg angle and λ is the wavelength of the incident radiation (in this study: $\lambda_{Cu\text{-}K\alpha}$ = 1.54 Å). For the yttrium vanadate system, the data were collected between 5-80° 2θ, and the reflection at 25° 2θ was chosen for the estimation of the mean crystallite size with the Scherrer equation. However, estimating the crystallite size by using Scherrer's equation is an approximation. In order to have a more precise estimation of the crystallites size and unit cell parameters, a Rietveld Refinement should be performed. The identification of the crystalline phases was conducted with the Diffract EVA software, and the measurements were taken with the Panalytical X'pert PRO instrument.

5.3 Scanning electron microscopy (SEM) and Energy dispersive x-ray analysis (EDX)

SEM (Scanning Electron Microscopy) is a type of microscopy that uses electron beams instead of light beams. The signal depends on the interactions between the electron beam and the specimen, and those can be divided into elastic and inelastic interactions. The elastic interactions are characterized by no energy loss and entail interactions of the beam with outer shell electrons or with the nucleus. Usually, electrons scattered by these elastic processes change their direction of motion of a wide angle, and when this angle is larger than 90°, they are called back scattered electrons (BSE). The back scattered electrons are then used for imaging. On the other hand, inelastic processes involve transfer of energy from the electron beam to the specimen through multiple possible mechanisms, which depend on the atomic

number of the specimen and the voltage of the beam. The most important of these mechanisms is the ionization of the sample which emits electrons after the interaction with the electron beam. These emitted electrons are called secondary electrons (SE), and are used for imaging and analyzing the sample. The electron beam does not get diffracted immediately when it impacts with the specimen on the surface, but it goes deeper in the sample for a certain distance before encountering an atom which diffracts the beam. This distance depends on the beam voltage and the atomic number of the specimen. The higher the atomic number, the higher the number of electrons that can interact with the beam. Both BSE and SE are used to generate the images of the sample.[127,128]

Among the possible inelastic processes, when a primary electron collides with an atom, one of its inner shell electrons can be displaced; then, one of the outer electrons can fall into the electron hole. In this case a radiation with an energy equal to the energy difference between the two electronic levels is emitted. Given that the energy of inner electronic levels strongly depends on the type of atom, the energy of the emitted radiation is characteristic of the atom. By analyzing the energy of the emitted radiations is therefore possible to analyze the composition of the specimen both qualitatively and quantitatively, according to the EDX (Energy Dispersive X-ray spectroscopy) analysis.[127,129] The SEM analysis were performed with a ZEISS GeminiSEM 560 field emission scanning electron microscope, with an Inlens SE detector at 1.00 kV and a working distance of 2.5 mm. The images were evaluated with the ImageJ software.

5.4 Transmission electron microscopy

TEM measurements were exploited to evaluate the dimensions of the yttrium vanadate particles synthesised via the miniemulsion approach and to evaluate the presence of yttrium vanadate particles in the pore network of the mesoporous metal oxides. The measurements were performed with a microscopy FEI Tecnai G2 (Department of Biology, University of Padua), working at 100 kV, equipped with an Olympus Veleta camera and a TVIPS F114 camera. For the sample preparation, one droplet of a suspension of each sample under investigation in ethanol was deposited on a carbon coated copper grating. The higher resolution images were acquired with a high-angle annular dark-field (HAADF) scanning transmission electron microscopy (HAADF-STEM) using TEM JEOL F200. Elemental analysis and mapping were performed using a JEOL 100 mm2 silicon drift energy dispersive X-ray spectrometer (EDX). The analysis of the dimensions of the nanoparticles was carried out using the ImageJ software.

5.5 Raman spectroscopy

The crystal structure and the variation in the crystal lattice due to the statistical substitution, as well as the possible presence of impurities in the synthesised yttrium vanadate samples, and the evaluation of the presence of yttrium vanadate particles inside the mesoporous metal oxides after thermal treatment were investigated through Raman spectroscopy. For this characterisation, a Raman microscopy Thermo

Scientific DXR (Department of Chemical Science, University of Padova), equipped with a solid-state laser with λ=532 nm, is employed. The Raman spectra are recorded in the range 100-3000 cm^{-1}, using a 50X lens and setting the laser power to 9 mW.

5.6 Dynamic light scattering (DLS)

The primary evaluation of the dimensions of the hydrodynamic radius of the droplets obtained after sonication and the evaluation of the yttrium vanadate powder particle size was conducted with the DLS technique. The exploited instrument was a Stabisizer, Particlemetrix (Department of Analytical and Inorganic Chemistry, JLU University). For the determination of the yttrium vanadate particle size, a suspension in water of the product powder was exploited.

5.7 UV-Vis diffuse reflectance spectroscopy

The band gap of the non-substituted and Eu(III)-statistically substituted yttrium vanadate samples was estimated with the UV-Vis diffuse reflectance spectroscopy. The employed spectrometer was a UV-Vis-NIR Cary 5E (Department of Analytical and Inorganic Chemistry, JLU University). The spectra were recorded in the range from 200 to 800 nm, and the baseline was acquired by measuring a 100 % reflectance (%R) reference. The band gap was calculated according to the Kubelka-Munk function (Equation 5.6)[130]:

$$F(R) = \frac{K}{S} = \frac{(1-R)^2}{2R} \qquad \textbf{5.6}$$

Where *K* is the molar absorption coefficient, *S* is the scattering factor, *R* is the %R divided by 100. To evaluate the band gap, the function $[F(R)\cdot E]^n$ vs E(eV) was plotted, and the intersection between the linear section of the curve with the x axis was determined. For a direct transition, as in the case of yttrium vanadate, the n coefficient is equal to 2.

5.8 TGA-DTA

The measurements were performed at the JLU University of Gieβen, in the Department of Analytical and Inorganic Chemistry, in the working group of Prof. Dr. Klaus Müller-Buschbaum. The measurements were taken with a STA 409 PC Luxx® coupled to a QMS 403 Aëlos Quadro mass spectrometer both from *NETZSCH*. The samples were measured in synthetic air atmosphere, with a gas flow of 30 $mL\cdot min^{-1}$, and

heating rate of 5 K·min^{-1}, in the temperature range 25-1000 °C. The exploited crucibles were composed of alumina, and the sample holder thermocouple was of type S.

5.9 Photoluminescence

The photoluminescence investigations of the non-substituted and substituted samples are performed in collaboration with Prof. Dr. Klaus Müller-Buschbaum at the Justus Liebig University of Giessen. Excitation and emission spectra are recorded using the HORIBA Jobin Yvon Spex Fluorolog 3 spectrometer equipped with a dual lamp housing (FL-1040A), a UV Xe short-arc lamp (450 W, USHIO), a UV xenon flaslamp (Exelitas FX-1102), a TCSPC (time-correlated single-photon counting) upgrade, double-grated excitation and emission monochromators, and a photomultiplier tube (R928P) using a FluoroEssence™ software. Excitation and emission spectra are corrected for the spectral response of the monochromators and the detector using spectral corrections provided by the manufacturer. Additionally, excitation spectra are corrected for the spectral distribution of the lamp intensity by the use of a photodiode reference detector. An edge filter (cutoff 455 nm, Newport) is used during the collection of emission spectra (for λex = 271 or 285 nm, for emission above 500 nm) and all excitation spectra. Overall emission process decay times are determined with the above-mentioned Fluorolog 3 instrument using a DataStation software. Exponential tail fitting is used for calculation of resulting intensity decay using Decay Analysis Software 6. Equation for luminescence lifetime fit:

$$I(t) = A + \sum_i B_i \cdot e^{-\frac{t}{\tau_i}} \qquad \textbf{5.7}$$

Where *I(t)* is the intensity of the emission dependent on the time, B_i are pre-exponential values, t is the time and τ_i is the lifetime of luminescence.

6 EXPERIMENTAL PROCEDURES

In this chapter, the experimental procedures exploited to carry out the optimisation of the stability of the miniemulsion system, the syntheses of yttrium vanadate in miniemulsion and the syntheses within the mesoporous metal oxides are described.

6.1 Chemicals

Table 6.1.1: Chemicals exploited in the synthesis of non-substituted, Eu(III)-substituted yttrium vanadate, and for the optimisation of the stability of the miniemulsion system.

Chemical	Molecular weight ($g \cdot mol^{-1}$)	CAS	Supplier
$Y(NO_3)_3 \cdot 6H_2O$	383.01	13494-98-9	thermoscientific
Na_3VO_4	183.91	13721-39-6	thermoscientific
NH_4VO_3	116.98	7803-55-6	thermoscientific
NaOH	40.00	1310-73-2	Sigma-Aldrich
C_6H_{12}	84.16	110-82-7	thermoscientific
Span80	428.62	1338-43-8	Sigma-Aldrich
$Eu(NO_3)_3 \cdot 6H_2O$	446.06	10031-53-5	abcr
$FeCl_3$	162.20	7705-08-0	-*
$K_4[Fe(CN)_6]$	422.39	14459-95-1	-*

*: chemical found in a substitutional bottle

For the synthesis within the mesoporous metal oxides supports, silica (SiO_2), titania (TiO_2) and zirconia (ZrO_2) were used. These mesoporous materials were synthesised in a previous work carried out at the JLU university of Gieβen in the group of Prof. Dr. Bernd Smarsly, under the supervision of M. Sc.. Lysander Wagner.

6.2 Optmisation of the miniemulsions stability

Yttrium nitrate system. In this scenario, the stability of miniemulsions obtained with $Y(NO_3)_3 \cdot 6H_2O$ as inorganic salt was studied, not performing the reaction between the two Y and V precursors. For the optimisation of the stability of the miniemulsion system, different miniemulsions with the aqueous phase consisting of a 0.1 M solution of $Y(NO_3)_3 \cdot 6H_2O$ were prepared, varying the experimental parameters one at a time to study the respective influence on the stability. As a general procedure, the continuous phase (oil phase) was prepared by adding a specific amount of surfactant with respect to the cyclohexane, considering the mass ratio (% w/w), and stirring until the surfactant was dissolved. Then, a specific amount of aqueous phase (the salt solution) was added to the oil phase, also in this case considering the mass ratio (w/w). After being mechanically stirred for a few minutes (roughly 5 minutes, until the mixture of the two phases appears turbid), the mixture was sonicated for a specific time with a Branson SFX550

sonicator, exploiting a titanium tip of 3 mm of diameter and a sonication pulse of 1 s / 0.5 s as sonication pulse / rest time, and at a specific working percentage amplitude of the maximum power. In any case, an ice-water bath was used to cool the system while forming the miniemulsion. Thus, the experimentally varied parameters were: i) the applied percentage amplitude, ii) the water to oil ratio, iii) the surfactant amount and iv) the sonication time. In the following tables, the different obtained miniemulsions are grouped according to the specific varied parameter.

Table 6.2.1: Miniemulsions prepared by varying the applied percentage power, keeping constant the other experimental parameters (sonication time, water to oil ratio and surfactant amount).

Sample name	Applied percentage power
ANG-01	50%
ANG-02	60%
ANG-03	70%

Table 6.2.2: Miniemulsions prepared by varying the water to oil ratio, keeping constant the other experimental parameters (sonication time, applied power and surfactant amount).

Sample name	Water to oil ratio (w/w)
ANG-01	1:3
ANG-04	1:4

For the case of a water to oil ratio of 1:3, 6 g of aqueous phase were added to 18 g of oil phase. On the other hand, for a 1:4 ratio, 5 g of aqueous phase were added to 20 g of oil phase.

Table 6.2.3: Miniemulsions prepared by varying the surfactant amount, keeping constant the other experimental parameters (sonication time, water to oil ratio and applied percentage power).

Sample name	Surfactant amount (% wt of the oil phase)
ANG-01	1.5%
ANG-06	2.3%
ANG-07	3.0%

For the case of 1.5% wt, 0.2676 g (0.62 mmol) of Span80 were added to 17.83 g (0.211 mol) of cyclohexane. For the 2.3% wt, 0.4137 g (0.96 mmol) of Span80 were added to 17.58 g (0.209 mol) of cyclohexane. For the 3.0% wt, 0.5251 g (1.22 mmol) of Span80 were added to 17.48 g (0.208 mol) of cyclohexane. In all cases, the oil phase resulted in 18 g total.

Table 6.2.4: Miniemulsions prepared by varying the sonication time, keeping constant the other experimental parameters (applied percentage power, water to oil ratio and surfactant amount).

Sample name	Sonication time (min)
ANG-01	2
ANG-08	4

As a reference for the initial $Y(NO_3)_3 \cdot 6H_2O$ solution, the weighted mass of the salt, the corresponding moles and concentration (in 25 mL of water) of the prepared solution is given in Table 6.2.5.

Table 6.2.5: Example of a starting solution of yttrium nitrate for the preparation of the miniemulsions.

Weighted mass (g)	Moles (mol)	Concentration ($mol \cdot L^{-1}$)
0.9604	$2.507 \cdot 10^{-3}$	0.10

Prussian blue system. As anticipated in paragraph 4.1, the optimisation of the stability of the miniemulsion system exploiting the reaction for the formation of the Prussian blue was carried out after the first synthesis attempt of the yttrium vanadate highlighted the material exchange amongst the droplets even without sonication. Thus, an optimisation of the experimental parameters for obtaining stable miniemulsions was carried out also considering this different system, which however was more reliable since a literature comparison was available. In this regard, starting solutions of $FeCl_3$ and $K_4[Fe(CN)_6]$ were prepared by dissolving a stoichiometric amount of the two precursors in deionised water, following the stoichiometry of the Reaction 6.1:

$$4Fe^{3+} + 3[Fe^{II}(CN)_6]^{4-} \rightarrow Fe_4[Fe(CN)_6]_3 \qquad \textbf{6.1}$$

The inverse miniemulsions of the two precursors were prepared as described for the yttrium nitrate system, and also in this case the parameters were varied one at a time. For these trials, the applied percentage power of the maximum power was kept constant at 50%, as well as the water to oil ratio was kept constant to w:o = 1:3. In this case the following tables refer to the miniemulsion resulting from the mixing of the miniemulsions of the two reagents. Also in this case, the different obtained miniemulsions are grouped according to the specific varied parameter. The samples are labelled as PB (Prussian blue).

Table 6.2.6: PB miniemulsions prepared by varying the sonication time, keeping constant the other experimental parameters (applied percentage power, water to oil ratio and surfactant amount).

Sample name	Sonication time (min)
PB-01	1
PB-02	2
PB-03	5

PB-04	15

The sonication time refers to both the miniemulsions of the reagents (sonicated separately), which were than mixed.

Table 6.2.7: PB miniemulsions prepared by varying the surfactant amount, keeping constant the other experimental parameters (sonication time, water to oil ratio and applied percentage power).

Sample name	Surfactant amount (% wt of the oil phase)
PB-01	1.5
PB-05	2.3
PB-06	3.0
PB-07	5.0
PB-08	10.0

Also in this case, the sum of the masses of the surfactant and cyclohexane was kept equal to 18 g, in order to maintain as constant the water to oil ratio of the resulting miniemulsion.

As a reference for the starting $FeCl_3$ and $K_4[Fe(CN)_6]$ solutions, the weighted mass of the salts, the corresponding moles and concentration (in 25 mL of water) of the two prepared solutions are given in Table 6.2.8.

Table 6.2.8: Example of two starting solutions of the reagents for the preparation of the PB miniemulsions.

Chemical	Weighted mass (g)	Moles (mol)	Concentration ($mol \cdot L^{-1}$)
$FeCl_3$	0.4047	$2.495 \cdot 10^{-3}$	0.10
$K_4[Fe(CN)_6]$	0.8025	$1.9 \cdot 10^{-3}$	0.076

6.3 Synthesis via inverse miniemulsion

For the synthesis of non-substituted YVO_4 via inverse miniemulsion, solutions of $Y(NO_3)_3 \cdot 6H_2O$ and NH_4VO_3 (or Na_3VO_4) precursors were prepared by dissolving a stoichiometric amount of the precursors salts in deionised water. The dispersed phase (water) was about 6 g of an aqueous solution of the precursor at the desired concentration. The continuous phase (oil) was prepared by adding 0.4140 g of Span80 (0.97 mmol, 2.3% wt) as surfactant to 17.58 g of cyclohexane (0.21 mol). The inverse miniemulsions of the two precursors were prepared in the same way independently. In total, 18 g of the continuous phase (cyclohexane + 2.3 % wt of surfactant) were added to 6 g of the dispersed phase (water) in order to have a water to oil ratio of 1:3 w/w. The emulsion mixtures of the reagents were mechanically stirred until the mixture resulted turbid. To adjust the pH of the synthesis, sodium hydroxide (3.97 M) was added. Three different synthetic approaches for the mixing of the reagents were tested, as described below. All the sonication steps were carried out exploiting an ice-water bath to cool down the system while forming the miniemulsions.

Method A (co-homogenisation + diffusion).

According to this synthetic method, the mixtures of the two reagents were sonicated separately for 1 min to obtain the respective miniemulsions. Then, the two miniemulsions of the reagents were mixed together and sonicated for 1 min in order to allow the fission and fusion of the droplets. Then, a specific amount of a 3.97 M solution of sodium hydroxide was added to the mixture, and it was let diffusing inside the droplets to adjust the pH of the solution. The amount of sodium hydroxide needed to obtain the desired pH value of the solution was calculated based on the amount of sodium hydroxide added to the same reactions carried out in batch, keeping constant the molar ratios amongst the reagents. Specifically, 330 µL (1.31 mmol), 490 µL (1.95 mmol) and 545 µL (2.16 mmol) of the 3.97 M solution of sodium hydroxide were added to the miniemulsion to reach pH values of 7, 9 and 11 respectively. Figure 6.3.1 summarises the synthetic method A.

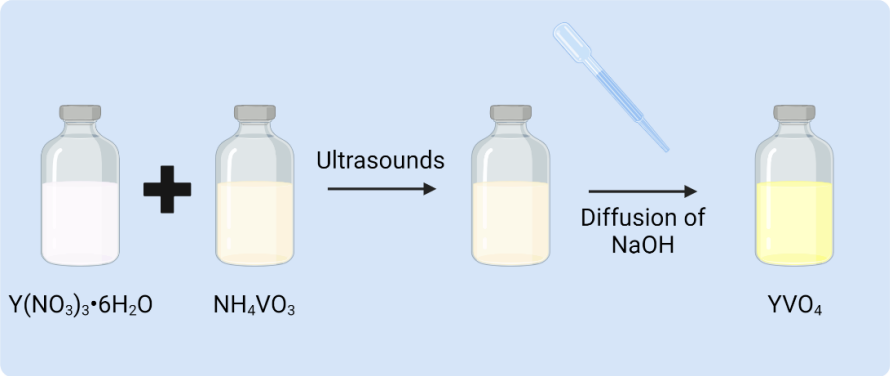

Figure 6.3.1: Schematic representation of the synthetic method A.

Method B (precipitation + co-homogenisation).

According to this synthetic method, the starting mixture of the yttrium educt was sonicated for 30 s in order to obtain an initial miniemulsion of this reagent. Then, a specific volume of NaOH solution (equal to that described for method A) was added to this miniemulsion, and the mixture was sonicated for further 30 s (a total of 1 min), causing the precipitation of the yttrium hydroxide inside the droplets. The initial sonication to form an initial miniemulsion of the yttrium educt is necessary, since the direct addition of the NaOH solution to the mixture (aqueous and organic phase not sonicated) itself would cause the precipitation of the $Y(OH)_3$, which would not then be included in the forming droplets. Finally, the two miniemulsions were mixed and sonicated for a further minute. Figure 6.3.2 summarises the synthetic method B.

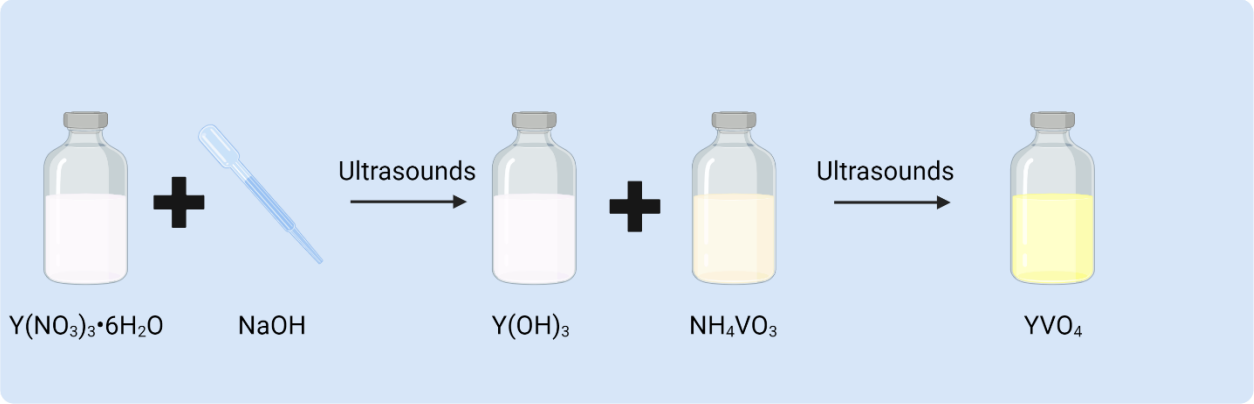

Figure 6.3.2: Schematic representation of the synthetic method B.

Method C (co-homogenisation).

As regards the synthetic method C, the starting mixture of the reagents were sonicated for 1 min to obtain the respective miniemulsions. Then, they were mixed and a specific volume of NaOH solution (cfr. method A and B) was added. Finally, the mixture of the two miniemulsions and NaOH solution was sonicated for a further minute in order to obtain the final miniemulsion. Figure 6.3.3 summarises the synthetic method C.

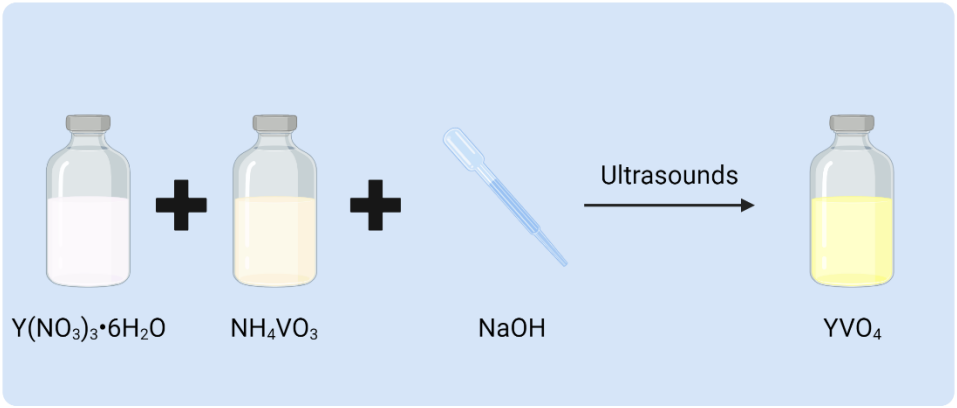

Figure 6.3.3: Schematic representation of the synthetic method C.

In all cases, the final miniemulsion obtained after sonication was turbid and of a yellow colour. The reaction mixture was left under mechanical stirring at room temperature for 24 h, and during this period, the miniemulsion gradually turned white. In order to isolate the product, roughly 20 mL of acetone were added to the miniemulsions in order to destabilise the miniemulsion droplets, and the solid was recovered through centrifugation at 9000 rpm for 7 min. Then, the solid was washed two times with 20 mL of acetone, two times with 20 mL of water and finally a further time with 20 mL of acetone. Each time, the solid was recovered by centrifugation at 9000 rpm for 7 min. Finally, the powder was dried in an oven at 50 °C overnight, and eventually ground.

For the synthesis in miniemulsion system, two reaction conditions were varied: the pH of the aqueous phase and the synthetic method. The synthesis of YVO_4 exploiting the Na_3VO_4 as vanadium precursor following the synthetic method B was also carried out to study possible differences due to the different vanadium precursor. The following tables group the samples according to the synthetic approach. The synthesis carried out at autogenic pH was conducted only once, since it was equivalent for all the different synthetic approaches.

Table 6.3.1: Yttrium vanadate samples obtained exploiting the different synthetic methods and at different pH values.

Sample name	Vanadium precursor	Synthetic method	V_{NaOH} (µL)	$NaOH/Y^{3+}$ molar ratio	pH
YV-A1	NH_4VO_3	A	330	2.08	7
YV-A2	NH_4VO_3	A	490	3.13	9
YV-A3	NH_4VO_3	A	545	3.61	11
YV-B1	NH_4VO_3	B	0	0	4 (autogenic)
YV-B2	NH_4VO_3	B	330	2.08	7
YV-B3	NH_4VO_3	B	490	3.13	9
YV-B4	NH_4VO_3	B	545	3.61	11
YV-C1	NH_4VO_3	C	330	2.08	7
YV-C2	NH_4VO_3	C	490	3.13	9
YV-C3	NH_4VO_3	C	545	3.61	11
YVO-01	Na_3VO_4	B	0	0	4 (autogenic)
YVO-02	Na_3VO_4	B	130	0.86	7
YVO-03	Na_3VO_4	B	235	1.55	9
YVO-04	Na_3VO_4	B	290	1.89	11

For the synthesis involving the orthovanadate as vanadium precursor, smaller quantities of sodium hydroxide were needed since the orthovanadate educt solution itself possesses a higher pH value (pH = 11-12), and therefore less hydroxide needs to be added.

As a reference for the starting solutions of the reagents, the weighted mass of the salts, the corresponding moles and concentration (in 25 mL of water) of the prepared solutions are given in Table 6.3.2.

Table 6.3.2: Example of three starting solutions of the reagents for the preparation of the miniemulsions.

Chemical	Weighted mass (g)	Moles (mol)	Concentration ($mol \cdot L^{-1}$)
$Y(NO_3)_3 \cdot 6H_2O$	0.9570	$2.50 \cdot 10^{-3}$	0.10
NH_4VO_3	0.2924	$2.50 \cdot 10^{-3}$	0.10
Na_3VO_4	0.4586	$2.49 \cdot 10^{-3}$	0.10

6.4 Synthesis of the Eu(III)-substituted yttrium vanadate via inverse miniemulsion

The substituted systems were synthesised exploiting the same protocols for the synthesis of non-substituted YVO_4 described in the previous paragraph. The fixed reaction conditions were NH_4VO_3 and $Y(NO_3)_3{\cdot}6H_2O$ (0.1 M) as vanadium and yttrium precursors respectively, room temperature, and 24 h as reaction time. Europium nitrate hexahydrate ($Eu(NO_3)_3{\cdot}6H_2O$) was chosen as Eu(III) precursor. The Eu(III) precursor was added in a stoichiometric amount to the Y(III) precursor solution. The syntheses were carried out with the same steps described for the synthesis in miniemulsion system, according to the different synthetic methods (A and B). The pale-yellow powder was isolated and purified with the same steps described in the previous paragraph. The Eu content (% at.) is calculated as Eu/(Eu+Y) molar ratio. The molar ratio between (Eu+Y) and VO_4^{3-} was kept constant and equal to 1:1 throughout all the synthesis of the substituted samples. Different Eu contents were tested – 1, 5 and 10 % at. – with different synthetic methods and different pH values, as described in Table 6.4.1.

Table 6.4.1: Eu(III)-substituted samples synthesised via miniemulsion approach with the different reaction conditions.

Sample name	Stoichiometry (theoretical)	Synthetic method	pH of aqueous phase	Eu content (% at.)	Y(III) mmol	VO_4^{3-} mmol	Eu(III) mmol
YV-E1	$Y_{0.99}Eu_{0.01}VO_4$	B	9	1	$5.77{\cdot}10^{-1}$	$5.87{\cdot}10^{-1}$	$5.69{\cdot}10^{-3}$
YV-E2	$Y_{0.95}Eu_{0.05}VO_4$	B	9	5	$5.54{\cdot}10^{-1}$	$5.90{\cdot}10^{-1}$	$2.92{\cdot}10^{-2}$
YV-E3	$Y_{0.9}Eu_{0.1}VO_4$	B	9	10	$5.23{\cdot}10^{-1}$	$5.84{\cdot}10^{-1}$	$5.80{\cdot}10^{-2}$
YV-E4	$Y_{0.99}Eu_{0.01}VO_4$	A	9	1	$5.76{\cdot}10^{-1}$	$5.85{\cdot}10^{-1}$	$5.68{\cdot}10^{-3}$
YV-E5	$Y_{0.95}Eu_{0.05}VO_4$	A	9	5	$5.53{\cdot}10^{-1}$	$5.92{\cdot}10^{-1}$	$2.92{\cdot}10^{-2}$
YV-E6	$Y_{0.9}Eu_{0.1}VO_4$	A	9	10	$5.26{\cdot}10^{-1}$	$5.94{\cdot}10^{-1}$	$5.83{\cdot}10^{-2}$
YV-E7	$Y_{0.99}Eu_{0.01}VO_4$	A	11	1	$5.75{\cdot}10^{-1}$	$5.87{\cdot}10^{-1}$	$5.67{\cdot}10^{-3}$
YV-E8	$Y_{0.95}Eu_{0.05}VO_4$	A	11	5	$5.53{\cdot}10^{-1}$	$5.81{\cdot}10^{-1}$	$2.92{\cdot}10^{-2}$
YV-E9	$Y_{0.9}Eu_{0.1}VO_4$	A	11	10	$5.24{\cdot}10^{-1}$	$5.86{\cdot}10^{-1}$	$5.81{\cdot}10^{-2}$
YV-E10	$Y_{0.95}Eu_{0.05}VO_4$	B	9	5	$5.65{\cdot}10^{-1}$	$5.84{\cdot}10^{-1}$	$3.14{\cdot}10^{-2}$

The starting solutions of yttrium and europium nitrate (in 20 mL) were prepared as described in Table 6.4.2.

Table 6.4.2: Solutions of the europium and yttrium precursors and respective density.

Percentage of europium (% at.)	Mass of yttrium nitrate (g)	Mass of europium nitrate (g)	Density ($g{\cdot}mL^{-1}$)
1	0.7570	0.0087	1.03
5	0.7273	0.0447	1.03
10	0.6897	0.0890	1.03

6.5 *Synthesis within mesoporous metal oxides*

The synthesis within mesoporous metal oxides was performed in three different metal oxides, previously synthesised and characterised during a laboratory work in the working group of Prof. Dr. Bernd Smarsly of the JLU University of Gieβen. For these syntheses, $Y(NO_3)_3 \cdot 6H_2O$ was chosen as yttrium educt, and Na_3VO_4 and NH_4VO_3 were chosen as vanadium educts. As regards the mesoporous metal oxides, silica (SiO_2), zirconia (ZrO_2) and titania (TiO_2) were tested as supports. For each metal oxide different pore size distributions and pore volumes were tested. The exploited precursors solutions had a concentration of 0.2 M, apart from the NH_4VO_3 solution which was 0.1 M because of solubility issues.

In general, the synthesis of YVO_4 particles was performed directly into the pores of the mesoporous materials exploiting a solid state reaction at high temperatures. The synthetic process was similar for all the exploited supports. A specific amount of mesoporous metal oxide was weighted and placed in a mortar. Then, knowing the specific pore volume (from previous physisorption analysis) and the weighted mass of the metal oxide – thus knowing the total pore volume – an exact volume, equal to the pore volume of the metal oxide, of precursor solution was added dropwise to the metal oxide powder and ground to favour the adsorption of the solution inside the pores (incipient wetness impregnation, IWI). Subsequently, the powder was slowly dried by a controlled drying step at 60 °C for 7 h in air. The impregnation step was repeated two times for each precursor, adsorbing the yttrium precursor first (when exploiting the NH_4VO_3 precursor, the impregnation step was repeated four times due to its halved concentration). Finally, the impregnated powders were thermally treated at 600 °C for 2 h in an alumina crucible, with temperature ramps of 5 °C·min^{-1}. The products were analysed as yttrium vanadate adsorbed into the porous matrix, without purification. Table 6.5.1 summarises all the exploited mesoporous metal oxides and their properties.

Table 6.5.1: Experimental conditions exploited for the impregnation of the different mesoporous metal oxides.

	Sample name	Pore size distribution (nm)	Specific V_{pores} ($cm^3 \cdot g^{-1}$)	Vanadium precursor	m mesoporous metal oxide (g)	Total V_{pores} (µL)
Mesoporous Silica	YVS-01	73 ± 10	0.693	Na_3VO_4	0.0504	35
	YVS-02	33 ± 5	0.684	Na_3VO_4	0.0524	36
	YVS-03	33 ± 5	0.684	NH_4VO_3	0.0532	36.5
	YVS-04	73 ± 10	0.693	NH_4VO_3	0.0611	42
Mesoporous Titania	YVT-01	9 ± 2	0.265	Na_3VO_4	0.0492	13
	YVT-02	84 ± 12	0.145	Na_3VO_4	0.0509	7.5
	YVT-03	38 ± 7	0.286	Na_3VO_4	0.0533	15.5
	YVT-04	38 ± 7	0.286	NH_4VO_3	0.0553	16
	YVT-05	84 ± 12	0.145	NH_4VO_3	0.0617	9
Mesoporous Zirconia	YVZ-01	23 ± 4	0.334	NH_4VO_3	0.0604	20
	YVZ-02	44 ± 5	0.179	NH_4VO_3	0.0618	11

7 CONCLUSIONS AND OUTLOOK

The main purpose of this Thesis project was to investigate how the space confinement influences the properties of yttrium vanadate nanoparticles in comparison to non-confined synthesis methods. For this reason, three different systems were tested, namely the batch synthesis (as not confined space system), the miniemulsion system and the mesoporous metal oxides. Moreover, yttrium vanadate was chosen as model inorganic compound since it can easily be synthesised even by a simple co-precipitation method or by thermal annealing. However, the synthesis in solution of this particular compound proceeds by following the Ostwald's step rule, which states that the product does not directly form in its thermodynamically stable form, but it proceeds through intermediate steps closer in energy to the starting situation (Paragraph 3.2). This particular behaviour allowed also to explore the consequences of performing this type of reaction in a confined space system (inverse miniemulsion).

In order to assess the influence of a confined space system, the synthesis of non-substituted and Eu(III)-substituted yttrium vanadate nanoparticles were conducted by systematically varying the reaction conditions, in a parallel way between batch and miniemulsion synthesis. By analysing the obtained results, it was possible to affirm that a successful synthesis of non-substituted and Eu(III)-substituted yttrium vanadate was performed, since no previous study was found in the literature. The miniemulsion system brought differences in the product properties as compared to the batch synthesis, with the main difference being the less sensitivity of the product properties (such as particles size and morphology) to the different reaction conditions, as compared to the batch synthesis. In the miniemulsion system, the morphology of the particles resulted to be quasi-spherical with all the different reaction conditions (even when exploiting the metavanadate as vanadium precursor), and the particles size was always comprised between roughly 30 and 40 nm, whereas for the batch synthesis, exploiting the metavanadate as vanadium precursor, the morphology of the particles was spindle-like and the particles size reached values up to 160 nm at pH 11. This difference is a clear sign of the templating effect of the miniemulsion droplets. However, the particles obtained via the miniemulsion system resulted to be aggregated (still individually distinguishable) and not well separated, as it would be expected by exploiting the miniemulsion confined space. As regards the synthesis of the substituted samples, a successful synthesis was performed in both systems. However, as far as their luminescence properties are concerned, the miniemulsion samples presented emission lifetimes that either did not follow a specific trend (method B) or followed an inverse trend as compared to that predicted by the literature, with the emission lifetime increasing with increasing lanthanide concentration (method A). On the other hand, batch samples reported a shorter emission lifetime with increasing Eu concentration, a trend which was in agreement with the literature. This could be due to a different distribution of the europium ions in the matrix in the samples obtained with the two different synthetic approaches (i.e. miniemulsion and batch), with the batch sample presenting a more homogeneous europium distribution. Moreover, the europium emission spectra of the samples obtained in batch differ from those obtained in miniemulsion, highlighting a possible structural difference, perhaps due to the presence of distortion in the matrix for the miniemulsion samples and/or phase separation in very low amounts. However, more in depth analysis, as well as the repetition of the synthesis of the miniemulsion samples to exclude occurrence of

experimental errors, are needed to draw more precise conclusions. The not well-defined morphology, the rather small crystallite sizes and the low crystallinity degree as well as the non-homogeneous distribution of europium ions in the matrix may present two possible explanations. The first is a not completed reaction, probably due to a slower reaction kinetics in the miniemulsion system. The second is the possibility that the miniemulsion system stabilises a different step in the Ostwald's step rule mechanism of the crystallisation of the yttrium vanadate. In order to check which is the more reliable explanation, longer reaction times should be employed: if no variations would occur in the particle properties with longer reaction times, thus the stabilisation of an intermediate step in the Ostwald's step rule mechanism would represent the more reliable explanation.

As regards the synthesis within the pore system of different mesoporous metal oxides, the work conducted within this Thesis project represents a preliminary study of the possibility to conduct a synthesis through thermal annealing within the pore system itself, since also in this case no comparison could be found in literature. The main issues of pursuing such a synthesis are the difficulty of purifying the yttrium vanadate particles from the support (in this case, the silica is the most promising of the three exploited metal oxides), and the thermal stability of the mesoporous metal oxides: above a defined temperature, the pore system starts to collapse. However, it can be stated that a successful synthesis of yttrium vanadate nanoparticles within the pore system of mesoporous silica was conducted and the obtained composite systems were thoroughly investigated, highlighting the possibility to obtain the formation of the target system by thermal annealing within the mesoporous system. The reaction was conducted at 600 °C for 2 h, much lower temperature and reaction time as compared to the usual values for thermal annealing synthesis. Moreover, the morphology and particles size of the reference sample (YVS-03) were comparable with those of the pores of the mesoporous silica. This means that it was possible to obtain spherical yttrium vanadate nanoparticles with size in the range of roughly 20 nm by thermal annealing, as opposed to typical particles obtained by thermal annealing with sizes up to the micrometer range.[131] This highlights the remarkable control over the product properties that can be reached by exploiting a reaction within the pores of a mesoporous material. On the other hand, as regards the zirconia and titania supports, the characterisation of the product properties was hindered by the crystalline nature of the two supports, which made impossible the estimation of the presence of yttrium vanadate in the powder by XRD or Raman measurements, and by the higher atomic weight of zirconium and titanium atoms, which made analysis by TEM images more challenging. Thus, further analysis of the properties of the product obtained with these supports have to be addressed.

However, for both systems – syntheses in miniemulsions and within mesoporous materials − further analysis have to be performed in order to draw more precise conclusions. More in detail, for the miniemulsion samples, a thorough analysis of the europium emission spectra may provide better insights into the structure of the different samples. Moreover, *in-situ* X-ray total scattering analysis at the Diamond synchrotron (Didcot, UK) will be carried out in January 2025, which may help to better understand the mechanism of the yttrium vanadate crystallisation, and thus understand the cause of the differences between the batch and miniemulsion syntheses.

On the other hand, as regards the synthesis within mesoporous metal oxides, the synthesis will be conducted exploring the wide experimental parameters space, for instance by varying the reaction

temperature, the reaction time or the quantity of adsorbed precursors. Moreover, thorough characterisation of the product properties will be performed with all the different samples, with also the possibility to dissolve the silica in a strong alkali environment to obtain the purified yttrium vanadate nanoparticles. The synthesis of Eu(III)-substituted samples within the mesoporous matrix will also be addressed.

Finally, it is possible to state that a successful synthesis of yttrium vanadate in both confined space systems was achieved, with the critical points highlighted. Also, a thorough investigation of the products properties was conducted, underlining the effective role of the confined space in determining the product properties.

8 BIBLIOGRAPHY

(1) Jiang, Q.; Ward, M. D. *Chem. Soc. Rev.* **2014**, *43* (7), 2066.

(2) Kumar, A.; Dutta, S.; Kim, S.; Kwon, T.; Patil, S. S.; Kumari, N.; Jeevanandham, S.; Lee, I. S. *Chem. Rev.* **2022**, *122* (15), 12748.

(3) Antonietti, M.; Landfester, K. *ChemPhysChem* **2001**, *2* (4), 207.

(4) Higuchi, W. I.; Misra, J. *Journal of Pharmaceutical Sciences* **1962**, *51* (5), 459.

(5) *The IUPAC Compendium of Chemical Terminology: The Gold Book*, 4th ed.; Gold, V., Ed.; International Union of Pure and Applied Chemistry (IUPAC): Research Triangle Park, NC, 2019.

(6) Zhu, X.; Cho, H.; Pasupong, M.; Regalbuto, J. R. *ACS Catal.* **2013**, *3* (4), 625.

(7) Luo, A.; Du, G.; Lai, H.; Shi, W. *Materials Science in Semiconductor Processing* **2014**, *23*, 20.

(8) Cardew, P. T. *Crystal Growth & Design* **2023**, *23* (6), 3958.

(9) Fleury, B.; Neouze, M.-A.; Guigner, J.-M.; Menguy, N.; Spalla, O.; Gacoin, T.; Carriere, D. *ACS Nano* **2014**, *8* (3), 2602.

(10) Becker, J.; Trügler, A.; Jakab, A.; Hohenester, U.; Sönnichsen, C. *Plasmonics* **2010**, *5* (2), 161.

(11) *Nanoparticles: From Theory to Application*, 1st ed.; Schmid, G., Ed.; Wiley, 2003.

(12) Kamat, P. V. *J. Phys. Chem. C* **2007**, *111* (7), 2834.

(13) Sun, L.; Yuan, G.; Gao, L.; Yang, J.; Chhowalla, M.; Gharahcheshmeh, M. H.; Gleason, K. K.; Choi, Y. S.; Hong, B. H.; Liu, Z. *Nat Rev Methods Primers* **2021**, *1* (1), 5.

(14) Navas, D.; Fuentes, S.; Castro-Alvarez, A.; Chavez-Angel, E. *Gels* **2021**, *7* (4), 275.

(15) LaGrow, A. P.; Besenhard, M. O.; Hodzic, A.; Sergides, A.; Bogart, L. K.; Gavriilidis, A.; Thanh, N. T. K. *Nanoscale* **2019**, *11* (14), 6620.

(16) Baláž, M.; Achimovičová, M.; Baláž, P.; Dutková, E.; Fabián, M.; Kováčová, M.; Lukáčová Bujňáková, Z.; Tóthová, E. *Current Opinion in Green and Sustainable Chemistry* **2020**, *24*, 7.

(17) Mahadule, R. K.; Arjunwadkar, P. R.; Mahabole, M. P. *International Journal of Metals* **2013**, *2013*, 1.

(18) Mietner, J. B.; Brieler, F. J.; Lee, Y. J.; Fröba, M. *Angew Chem Int Ed* **2017**, *56* (40), 12348.

(19) Landfester, K.; Bechthold, N.; Tiarks, F.; Antonietti, M. *Macromolecules* **1999**, *32* (16), 5222.

(20) Landfester, K. In *Colloid Chemistry II*; Antonietti, M., Ed.; De Meijere, A., Kessler, H., Ley, S. V., Thiem, J., Vögtle, F., Houk, K. N., Lehn, J.-M., Schreiber, S. L., Trost, B. M., Yamamoto, H., Series Eds.; Topics in Current Chemistry; Springer Berlin Heidelberg: Berlin, Heidelberg, 2003; Vol. 227, pp 75–123.

(21) Muñoz-Espí, R.; Weiss, C. K.; Landfester, K. *Current Opinion in Colloid & Interface Science* **2012**, *17* (4), 212.

(22) Dolcet, P.; Casarin, M.; Maccato, C.; Bovo, L.; Ischia, G.; Gialanella, S.; Mancin, F.; Tondello, E.; Gross, S. *J. Mater. Chem.* **2012**, *22* (4), 1620.

(23) Mazzariol, C.; Tajoli, F.; Sedykh, A. E.; Dolcet, P.; Grunwaldt, J.-D.; Müller-Buschbaum, K.; Gross, S. *ACS Appl. Nano Mater.* **2023**, *6* (17), 15510.

(24) Tajoli, F.; Massagrande, M. V.; Muñoz-Espí, R.; Gross, S. *Nanomaterials* **2023**, *13* (6), 1046.

(25) Morgese, G.; Dolcet, P.; Feis, A.; Gellini, C.; Gialanella, S.; Speghini, A.; Badocco, D.; Pastore, P.; Casarin, M.; Gross, S. *Eur J Inorg Chem* **2017**, *2017* (20), 2745.

(26) Benedetti, C.; Flouda, P.; Antonello, A.; Rosenauer, C.; Pérez-Pla, F. F.; Landfester, K.; Gross, S.; Muñoz-Espí, R. *Nanotechnology* **2017**, *28* (36), 365603.

(27) *Colloid science: principles, methods and applications*; Cosgrove, T., Ed.; Blackwell Pub: Oxford, UK ; Ames, Iowa, 2005.

(28) Landfester, K. *Macromol. Symp.* **2000**, *150* (1), 171.

(29) Tajoli, F. Space Matters: crystallization of inorganic systems in confined spaces, Università di Padova, Ph.D. Thesis, 2023.

(30) Antonietti, M.; Landfester, K. *Prog. Polym. Sci.* **2002**.

(31) Diodati, S.; Dolcet, P.; Casarin, M.; Gross, S. *Chem. Rev.* **2015**, *115* (20), 11449.

(32) Schuchmann, H. p.; Schubert, H. *Engineering in Life Sciences* **2003**, *3* (2), 67.

(33) *Handbook of green chemistry and technology*, Repr.; Clark, J., Ed.; Blackwell Science: Oxford, 2005.

(34) *Colloids and Colloid Assemblies: Synthesis, Modification, Organization and Utilization of Colloid Particles*, 1st ed.; Caruso, F., Ed.; Wiley, Weinheim, 2003.

(35) Goodwin, J. W. *Colloids and Interfaces with Surfactants and Polymers - An Introduction*; John Wiley & Sons, Ltd: Chichester, UK, 2004.

(36) Schiller, R.; Weiss, C. K.; Landfester, K. *Nanotechnology* **2010**, *21* (40), 405603.

(37) Landfester, K. *Adv. Mater.* **2001**, *13* (10), 765.

(38) Landfester, K. *Annu. Rev. Mater. Res.* **2006**, *36* (1), 231.

(39) *The Chemistry of Metal-Organic Frameworks: Synthesis, Characterization, and Applications: Synthesis, Characterization, and Applications*; Kaskel, S., Ed.; Wiley-VCH Verlag GmbH & Co. KGaA: Weinheim, Germany, 2016.

(40) Luque, R.; Ahmad, A.; Tariq, S.; Mubashir, M.; Sufyan Javed, M.; Rajendran, S.; Varma, R. S.; Ali, A.; Xia, C. *Materials Today* **2024**, *73*, 105.

(41) Parlett, C. M. A.; Wilson, K.; Lee, A. F. *Chem. Soc. Rev.* **2013**, *42* (9), 3876.

(42) Zhang, Y.; Zhang, T.; Huang, Z.; Yang, J. *Advanced Science* **2022**, *9* (7), 2105084.

(43) Kjellman, T.; Reichhardt, N.; Sakeye, M.; Smått, J.-H.; Lindén, M.; Alfredsson, V. *Chem. Mater.* **2013**, *25* (9), 1989.

(44) Martínez, C.; Corma, A. In *Comprehensive Inorganic Chemistry II*; Elsevier, Valencia, 2013; pp 103–131.

(45) Cundy, C. S.; Cox, P. A. *Chem. Rev.* **2003**, *103* (3), 663.

(46) Kresge, C. T.; Leonowicz, M. E.; Roth, W. J.; Vartuli, J. C.; Beck, J. S. *Nature* **1992**, *359* (6397), 710.

(47) Brinker, C. J.; Scherer, C. W. *Sol-Gel Science: the physics and chemistry of sol-gel processing.*; Elsevier Science: St Louis, 2014.

(48) Danks, A. E.; Hall, S. R.; Schnepp, Z. *Mater. Horiz.* **2016**, *3* (2), 91.

(49) Poolakkandy, R. R.; Menamparambath, M. M. *Nanoscale Adv.* **2020**, *2* (11), 5015.

(50) Marcos-Hernández, M.; Villagrán, D. In *Composite Nanoadsorbents*; Elsevier, 2019; pp 265–293.

(51) Brinker, C. J.; Lu, Y.; Sellinger, A.; Fan, H. *Adv. Mater.* **1999**, *11* (7), 579.

(52) Grosso, D.; Cagnol, F.; Soler-Illia, G. J. de A. A.; Crepaldi, E. L.; Amenitsch, H.; Brunet-Bruneau, A.; Bourgeois, A.; Sanchez, C. *Adv Funct Materials* **2004**, *14* (4), 309.

(53) Mahoney, L.; Koodali, R. *Materials* **2014**, *7* (4), 2697.

(54) Komiyama, M. *Catalysis Reviews* **1985**, *27* (2), 341.

(55) Lekhal, A.; Glasser, B. J.; Khinast, J. G. *Chemical Engineering Science* **2001**.

(56) Roggenbuck, J.; Waitz, T.; Tiemann, M. *Microporous and Mesoporous Materials* **2008**, *113* (1–3), 575.

(57) Maatman, R. W.; Prater, C. D. *Ind. Eng. Chem.* **1957**, *49* (2), 253.

(58) Li, G.; Yao, B. Q.; Meng, P. B.; Duan, X. M.; Ju, Y. L.; Wang, Y. Z. *Optical Materials* **2011**, *33* (6), 937.

(59) Li, H.; Wu, X.; Song, R. *Materials Characterization* **2008**, *59* (8), 1066.

(60) Huang, C.-H.; Chen, J.-C.; Hu, C. *Journal of Crystal Growth* **2000**.

(61) Wiglusz, R. J.; Marciniak, L.; Pazik, R.; Strek, W. *Crystal Growth & Design* **2014**, *14* (11), 5512.

(62) Brecher, C.; Samelson, H.; Lempicki, A.; Riley, R.; Peters, T. *Phys. Rev.* **1967**, *155* (2), 178.

(63) Finch, R. J. *Reviews in Mineralogy and Geochemistry* **2003**, *53* (1), 1.

(64) Miller, S. A.; Caspers, H. H.; Rast, H. E. *Phys. Rev.* **1968**, *168* (3), 964.

(65) Jayaraman, A.; Kourouklis, G. A.; Espinosa, G. P.; Cooper, A. S.; Van Uitert, L. G. *Journal of Physics and Chemistry of Solids* **1987**, *48* (8), 755.

(66) Baes, C. F., 1924-; Mesmer, R. E., 1934-. *The hydrolysis of cations*; Wiley-Interscience publication; Wiley: New York, 1976.

(67) *Vanadium Compounds: Chemistry, Biochemistry, and Therapeutic Applications*; Tracey, A. S., Crans, D. C., Eds.; ACS Symposium Series; American Chemical Society: Washington, DC, 1998; Vol. 711.

(68) Karthika, S.; Radhakrishnan, T. K.; Kalaichelvi, P. *Crystal Growth & Design* **2016**, *16* (11), 6663.

(69) Jun, Y.-S.; Zhu, Y.; Wang, Y.; Ghim, D.; Wu, X.; Kim, D.; Jung, H. *Annu. Rev. Phys. Chem.* **2022**, *73* (1), 453.

(70) Mer, V. K. L. *Ind. Eng. Chem.* **1952**, *44* (6), 1270.

(71) Sugimoto, T. *Journal of Colloid and Interface Science* **2007**, *309* (1), 106.

(72) Chu, D. B. K.; Owen, J. S.; Peters, B. *J. Phys. Chem. A* **2017**, *121* (40), 7511.

(73) Ostwald, W. *Phys. Chem* **1897**, *22*, 289−330.

(74) Cölfen, H.; Mann, S. *Angew Chem Int Ed* **2003**, *42* (21), 2350.

(75) Huignard, A.; Buissette, V.; Laurent, G.; Gacoin, T.; Boilot, J.-P. *Chem. Mater.* **2002**, *14* (5), 2264.

(76) Bauzá, A.; Mooibroek, T. J.; Frontera, A. *CrystEngComm* **2016**, *18* (1), 10.

(77) Chander, H. *Materials Science and Engineering: R: Reports* **2005**, *49* (5), 113.

(78) Chen, L.; Liu, G.; Liu, Y.; Huang, K. *Journal of Materials Processing Technology* **2008**, *198* (1–3), 129.

(79) Xia, S.; Guan, A.; Chen, P.; Wang, G.; Geng, Y.; Zhou, L. *Superlattices and Microstructures* **2016**, *97*, 319.

(80) Zhu, L.; Li, J.; Li, Q.; Liu, X.; Meng, J.; Cao, X. *Nanotechnology* **2007**, *18* (5), 055604.

(81) Yan, C.-H.; Sun, L.-D.; Liao, C.-S.; Zhang, Y.-X.; Lu, Y.-Q.; Huang, S.-H.; Lü, S.-Z. *Applied Physics Letters* **2003**, *82* (20), 3511.

(82) Kunimoto, T.; Fujita, Y.; Okura, H. *IEICE Trans. Electron.* **2016**, *E99.C* (11), 1249.

(83) Chang, Y.-S.; Huang, F.-M.; Tsai, Y.-Y.; Teoh, L.-G. *Journal of Luminescence* **2009**, *129* (10), 1181.

(84) Piz, M.; Filipek, E.; Klukowski, D.; Kochmański, P. *Sustainability* **2023**, *15* (19), 14606.

(85) Reitz, C.; Smarsly, B.; Brezesinski, T. *ACS Appl. Nano Mater.* **2019**, *2* (2), 1063.

(86) Hsu, C.; Powell, R. C. *Journal of Luminescence* **1975**, *10* (5), 273.

(87) *Phosphor handbook*, 2nd ed.; Yen, W. M., Shionoya, S., Yamamoto, H., Eds.; The CRC Press laser and optical science and technology series; CRC Press/Taylor and Francis: Boca Raton, FL, 2007.

(88) Blasse, G. In *Handbook on the Physics and Chemistry of Rare Earths*; Elsevier, 1979; Vol. 4, pp 237–274.

(89) Dolgos, M. R.; Paraskos, A. M.; Stoltzfus, M. W.; Yarnell, S. C.; Woodward, P. M. *Journal of Solid State Chemistry* **2009**, *182* (7), 1964.

(90) Matsushima, Y.; Sato, A.; Kitaura, M.; Kominami, H.; Hara, K. *J. Ceram. Soc. Japan* **2019**, *127* (9), 627.

(91) Rothschild, S. *Br. J. Appl. Phys.* **1955**, *6* (S4), S32.

(92) Mohamed, R. M.; Harraz, F. A. *Journal of Materials Research and Technology* **2020**, *9* (3), 5666.

(93) Boudreaux, D. S.; La France, T. S. *Journal of Physics and Chemistry of Solids* **1974**, *35* (7), 897.

(94) http://abulafia.mt.ic.ac.uk/shannon/ptable.php.

(95) Palilla, F. C.; Levine, A. K.; Rinkevics, M. *J. Electrochem. Soc.* **1965**, *112* (8), 776.

(96) Binnemans, K. *Coordination Chemistry Reviews* **2015**, *295*, 1.

(97) Adamou, P.; Harkou, E.; Hafeez, S.; Manos, G.; Villa, A.; Al-Salem, S. M.; Constantinou, A.; Dimitratos, N. *Ultrasonics Sonochemistry* **2023**, *100*, 106610.

(98) Rharbi, Y.; Winnik, M. A. *Advances in Colloid and Interface Science* **2001**, *89–90*, 25.

(99) *Powder diffraction: theory and practice*; Dinnebier, R. E., Billinge, S. J. L., Eds.; Royal Society of Chemistry: Cambridge, 2008.

(100) Dinnebier, R. E.; Leineweber, A.; Evans, J. S. O. *Rietveld refinement: practical powder diffraction pattern analysis using TOPAS*; De Gruyter: Berlin ; Boston, 2019.

(101) Wang, F.; Yu, L.; Zhu, Y.; Zhu, Z.; Meng, X.; Lv, Y.; Peng, S.; Yang, L. *Journal of Alloys and Compounds* **2023**, *968*, 172259.

(102) Socrates, G. *Infrared and Raman characteristic group frequencies: tables and charts*, 3rd ed.; Wiley: Chichester ; New York, 2001.

(103) Barbour, A.; Luttrell, R. D.; Choi, J.; Musfeldt, J. L.; Zipse, D.; Dalal, N. S.; Boukhvalov, D. W.; Dobrovitski, V. V.; Katsnelson, M. I.; Lichtenstein, A. I.; Harmon, B. N.; Kögerler, P. *Phys. Rev. B* **2006**, *74* (1), 014411.

(104) Khademolhoseini, S.; Mazaheri, S. *J Mater Sci: Mater Electron* **2017**, *28* (2), 2221.

(105) Messekine, S.; Sahnoun, M.; Driz, M.; Daul, C. *Zeitschrift für Kristallographie* **2010**, *225* (11).

(106) Trajić, J.; Rabasović, M. S.; Savić-Šević, S.; Ševic, D.; Babić, B.; Romčević, M.; Ristić-Djurović, J. L.; Paunović, N.; Križan, J.; Romčević, N. *Infrared Physics & Technology* **2016**, *77*, 226.

(107) Yu, P. Y.; Cardona, M. *Fundamentals of semiconductors: physics and materials properties ; with 52 tables and 116 problems*, 3., rev.enl. ed., 3., corr. print.; Springer: Berlin Heidelberg, 2005.

(108) Brus, L. *J. Phys. Chem.* **1986**, *90* (12), 2555.

(109) Becerro, A. I.; Allix, M.; Laguna, M.; González-Mancebo, D.; Genevois, C.; Caballero, A.; Lozano, G.; Núñez, N. O.; Ocaña, M. *J. Mater. Chem. C* **2018**, *6* (47), 12830.

(110) Karacaoglu, E.; Yildirim, O. A.; Ozturk, T.; Gul, M. *Journal of Materials Research* **2023**, *38* (14), 3536.

(111) Shvets, P.; Dikaya, O.; Maksimova, K.; Goikhman, A. *J Raman Spectroscopy* **2019**, *50* (8), 1226.

(112) Husson, E.; Proust, C.; Gillet, P.; Itié, J. P. *Materials Research Bulletin* **1999**, *34* (12–13), 2085.

(113) H E Swanson; Standard x-ray diffraction powder patterns, US Department of Commerce, National Bureauof Standards. **1955**, *25*.

(114) Ohsaka, T.; Izumi, F.; Fujiki, Y. *J Raman Spectroscopy* **1978**, *7* (6), 321.

(115) Ferrari, A. C. *Solid State Communications* **2007**, *143* (1–2), 47.

(116) Phillippi, C. M.; Mazdiyasni, K. S. *Journal of the American Ceramic Society* **1971**, *54* (5), 254.

(117) Sivakumar, T.; Gopalakrishnan, J. *Chem. Mater.* **2002**, *14* (9), 3984.

(118) Thommes, M.; Cychosz, K. A. *Adsorption* **2014**, *20* (2–3), 233.

(119) Condon, J. B. *Surface area and porosity determinations by physisorption: measurements and theory*, 1st ed.; Elsevier: Amsterdam ; Boston, 2006.

(120) Schlumberger, C.; Thommes, M. *Adv Materials Inter* **2021**, *8* (4), 2002181.

(121) Thommes, M.; Kaneko, K.; Neimark, A. V.; Olivier, J. P.; Rodriguez-Reinoso, F.; Rouquerol, J.; Sing, K. S. W. *Pure and Applied Chemistry* **2015**, *87* (9–10), 1051.

(122) Wagner, L. Q.; Novel Polymeric Templates for the Preparation of Mesoporous Metal Oxides, Master Thesis, Gieβen. **2021**.

(123) Elton, L. R. B.; Jackson, D. F. *American Journal of Physics* **1966**, *34* (11), 1036.

(124) Nasrazadani, S.; Hassani, S. In *Handbook of Materials Failure Analysis with Case Studies from the Oil and Gas Industry*; Elsevier, 2016; pp 39–54.

(125) Scrivens, G.; Ticehurst, M.; Swanson, J. T. In *Accelerated Predictive Stability*; Elsevier, 2018; pp 175–206.

(126) Muniz, F. T. L.; Miranda, M. A. R.; Morilla Dos Santos, C.; Sasaki, J. M. *Acta Crystallogr A Found Adv* **2016**, *72* (3), 385.

(127) Zhou, W.; Apkarian, R.; Wang, Z. L.; Joy, D. In *Scanning Microscopy for Nanotechnology*; Zhou, W., Wang, Z. L., Eds.; Springer New York: New York, NY, 2006; pp 1–40.

(128) Mohammed, A.; Abdullah, A.; (2018, November). Scanning electron microscopy (SEM): A review. In Proceedings of the 2018 International Conference on Hydraulics and Pneumatics—HERVEX, Băile Govora, Romania (Vol. 2018, pp. 7-9). .

(129) Ismail, A. F.; Khulbe, K. C.; Matsuura, T. In *Reverse Osmosis*; Elsevier, 2019; pp 57–90.

(130) Makuła, P.; Pacia, M.; Macyk, W. *J. Phys. Chem. Lett.* **2018**, *9* (23), 6814.

(131) Voloshina, O. V.; Baumer, V. N.; Bondar, V. G.; Kurtsev, D. A.; Gorbacheva, T. E.; Zenya, I. M.; Zhukov, A. V.; Sidletskiy, O. Ts. *Nuclear Instruments and Methods in Physics Research Section A: Accelerators, Spectrometers, Detectors and Associated Equipment* **2012**, *664* (1), 299.

9 APPENDIX

9.1 APPENDIX A.1: MINIEMULSION AND BATCH SAMPLES

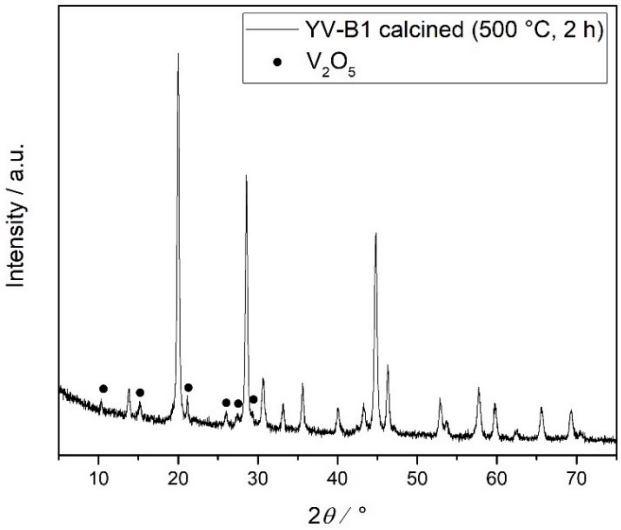

Figure 9.1.1: Diffractogram of the sample obtained exploiting synthetic method B, pH 4, NH_4VO_3 as vanadium educt after calcination.

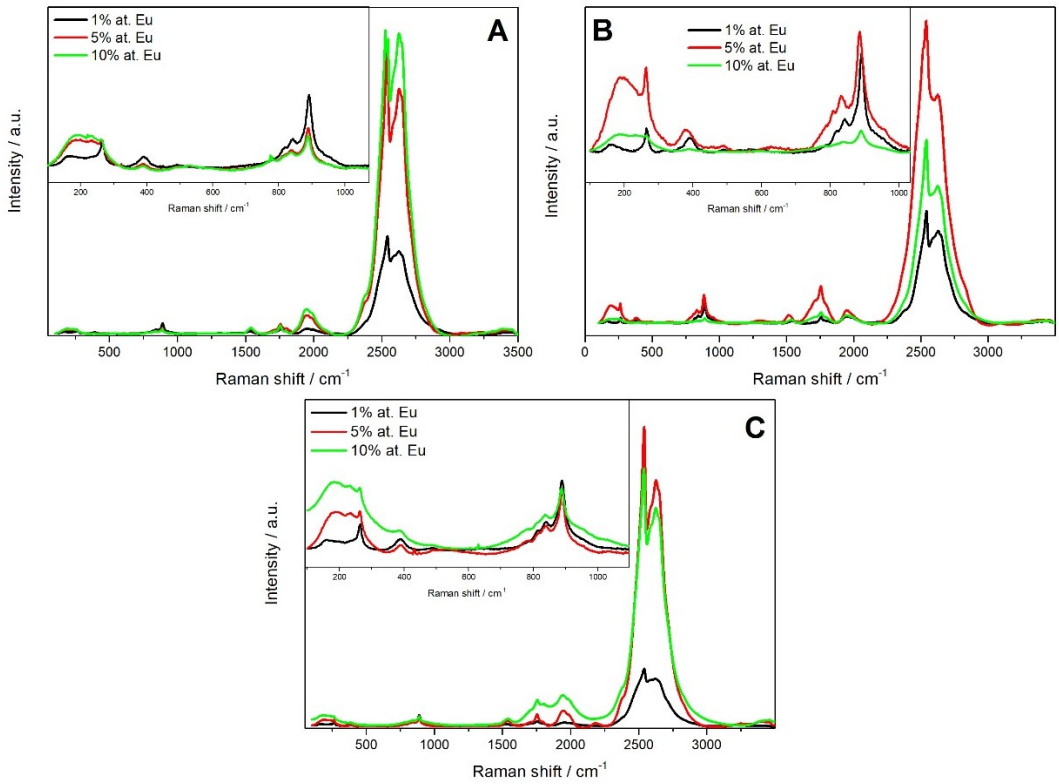

Figure 9.1.2: Raman spectra of the Eu(III)-substituted samples obtained through synthetic method A pH 9 (A), method B, pH 9 (B) and method A, pH 11 (C).

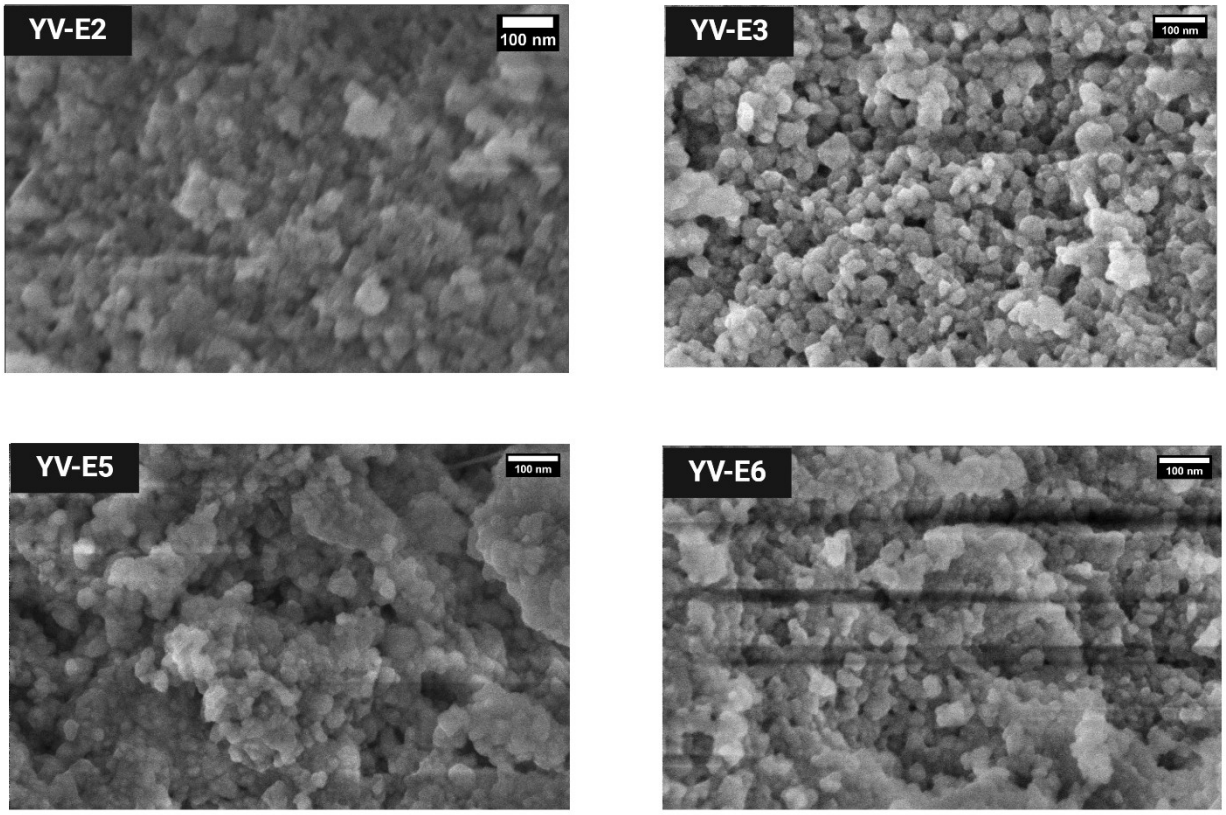

Figure 9.1.3: SEM images of the Eu(III)-substituted samples.

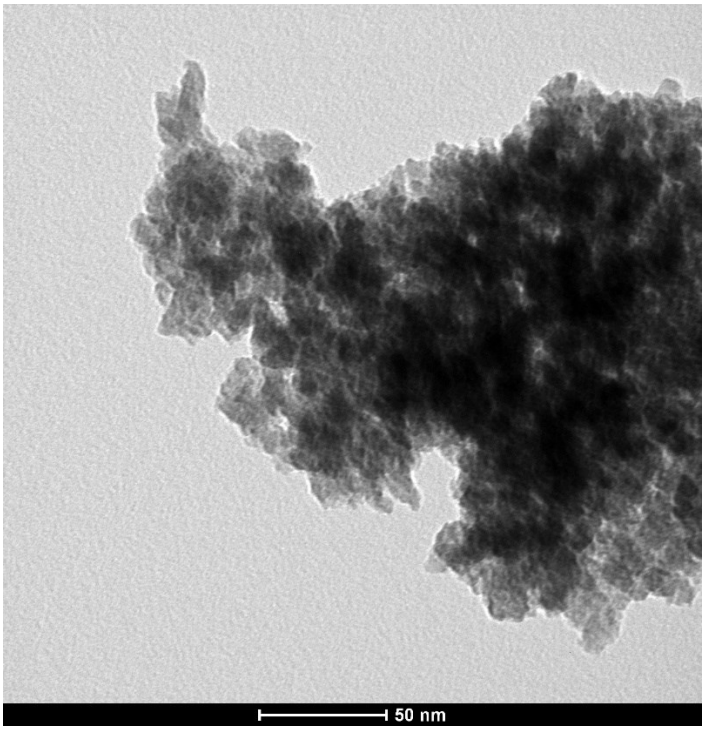

Figure 9.1.4: TEM image of the sample obtained exploiting synthetic method A, pH 9 and 10% at. Eu.

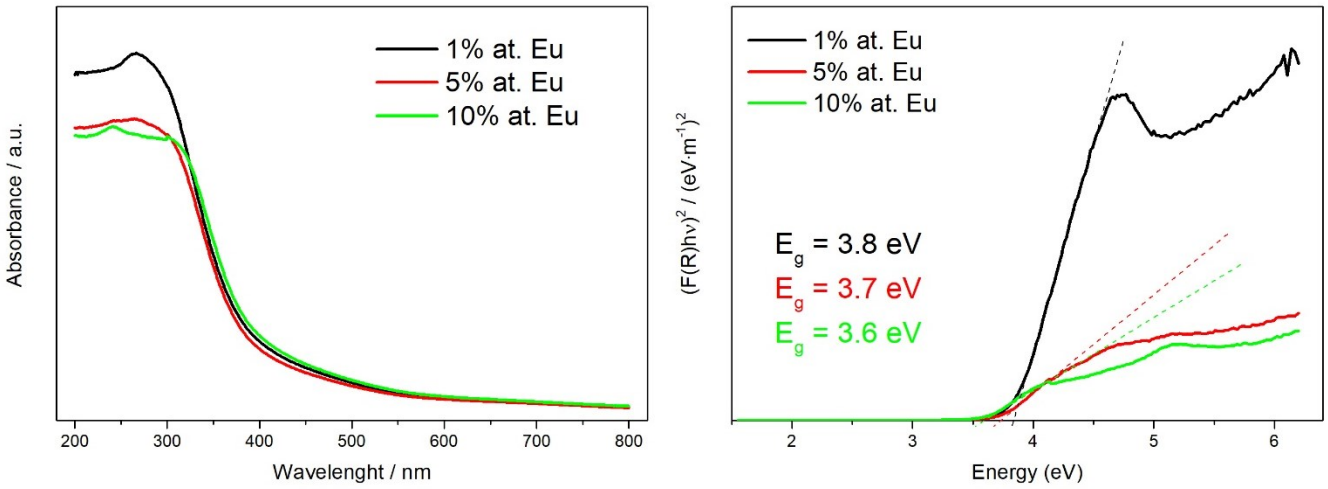

Figure 9.1.5: UV-Vis spectra (left) and Tauc plots (right) of the samples obtained at pH 11 exploiting the synthetic method C.

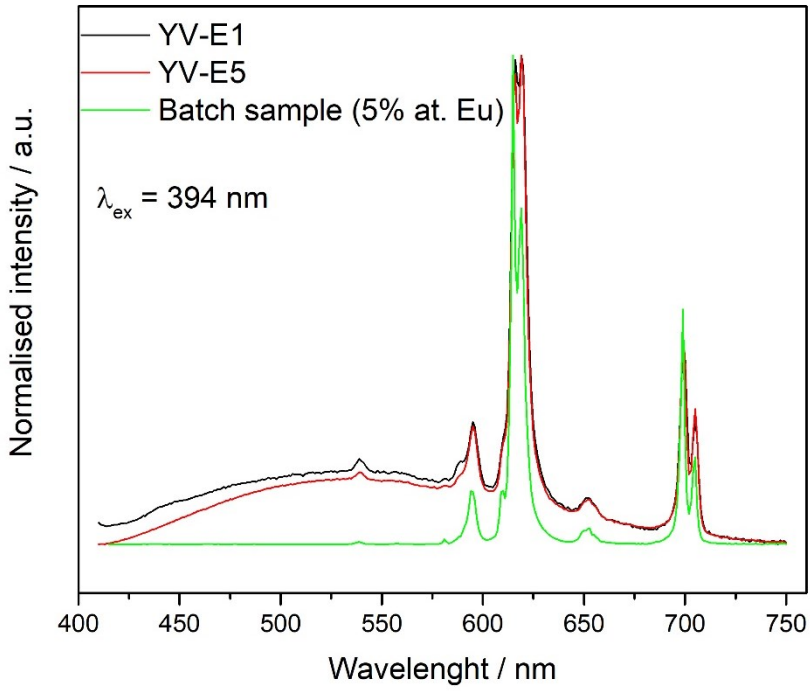

Figure 9.1.6: Emission spectra of the samples when exciting directly the europium ions.

9.2 APPENDIX A.2: SYNTHESIS WITHIN MESOPOROUS MATERIALS

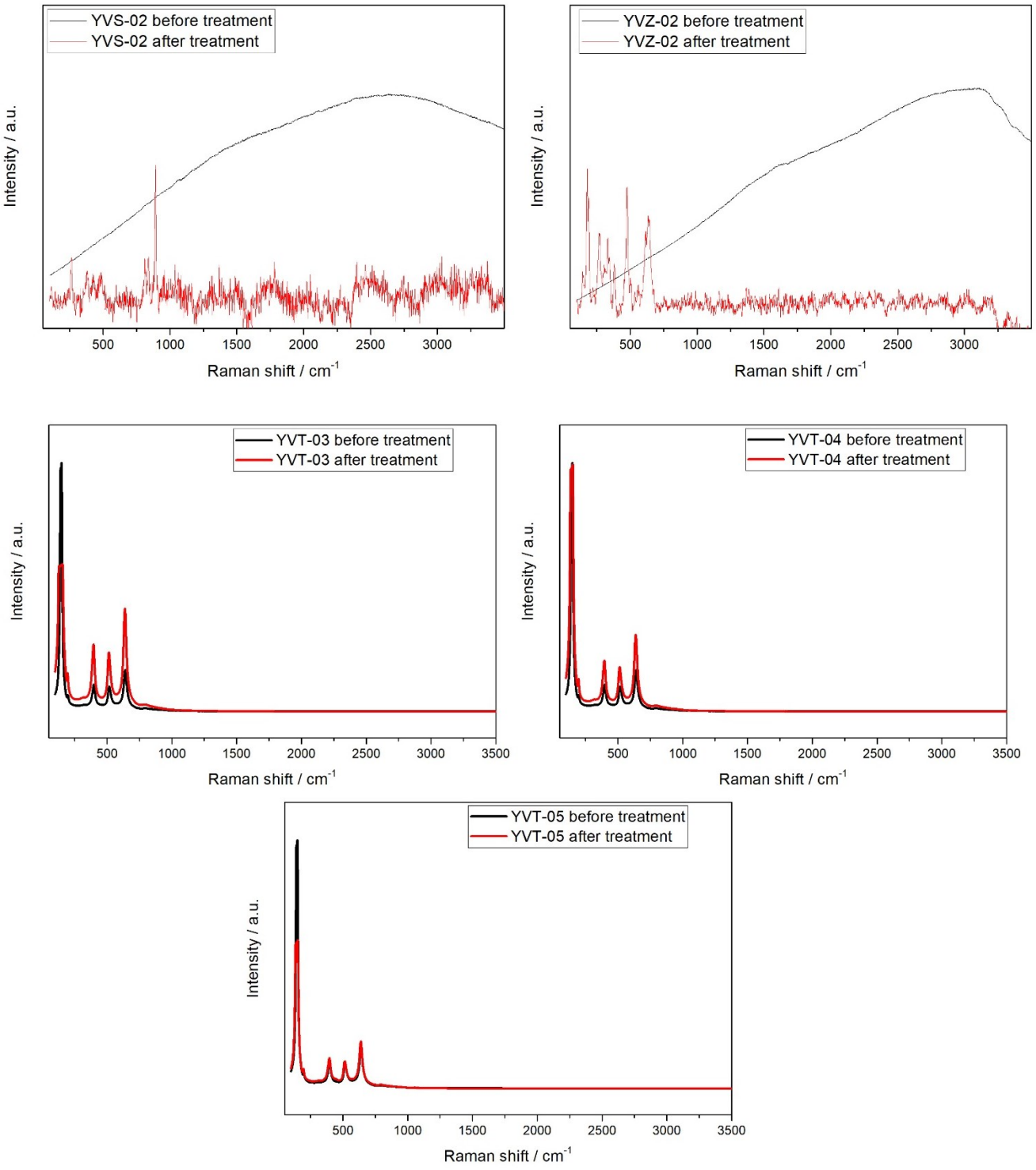

Figure 9.2.1: Raman spectra of the samples before and after the thermal treatment.